2014

Modeling and simulation of continuous fiber-reinforced ceramic composites

Venkata Bheemreddy

Department: Mechanical and Aerospace Engineering

MODELING AND SIMULATION

OF CONTINUOUS FIBER-REINFORCED CERAMIC COMPOSITES

by

VENKATA BHEEMREDDY

A DISSERTATION

Presented to the Faculty of the Graduate School of the

MISSOURI UNIVERSITY OF SCIENCE AND TECHNOLOGY

In Partial Fulfillment of the Requirements for the Degree

DOCTOR OF PHILOSOPHY

in

MECHANICAL ENGINEERING

2014

Approved
K. Chandrashekhara, Advisor
L. R. Dharani
V. Birman
G. E. Hilmas
V. A. Samaranayake

PUBLICATION DISSERTATION OPTION

This dissertation has been prepared in the form of three papers for publication as follows:

Pages 8-52 have been published in Computational Materials Science journal

Pages 53-95 are intended for submission to International Journal of Damage Mechanics

Pages 96-124 are intended for submission to International Journal of Numerical Methods in Engineering

ABSTRACT

Finite element modeling framework based on cohesive damage modeling, constitutive material behavior using user-material subroutines, and extended finite element method (XFEM), are developed for studying the failure behavior of continuous fiber-reinforced ceramic matrix composites (CFCCs) by the example of a silicon carbide matrix reinforced with silicon carbide fiber (SiC/SiC_f) composite. This work deals with developing comprehensive numerical models for three problems: (1) fiber/matrix interface debonding and fiber pull-out, (2) mechanical behavior of a CFCC using a representative volume element (RVE) approach, and (3) microstructure image-based modeling of a CFCC using object oriented finite element analysis (OOF). Load versus displacement behavior during a fiber pull-out event was investigated using a cohesive damage model and an artificial neural network model. Mechanical behavior of a CFCC was investigated using a statistically equivalent RVE. A three-step procedure was developed for generating a randomized fiber distribution. Elastic properties and damage behavior of a CFCC were analyzed using the developed RVE models. Scattering of strength distribution in CFCCs was taken into account using a Weibull probability law. A multi-scale modeling framework was developed for evaluating the fracture behavior of a CFCC as a function of microstructural attributes. A finite element mesh of the microstructure was generated using an OOF tool. XFEM was used to study crack propagation in the microstructure and the fracture behavior was analyzed. The work performed provides a valuable procedure for developing a multi-scale framework for comprehensive damage study of CFCCs.

ACKNOWLEDGMENTS

I would like to express my sincere gratitude to Dr. K Chandrashekhara for his valuable guidance, assistance and encouragement during my graduate study at Missouri University of Science and Technology. I would like to thank him for generous support of providing excellent working environment and teamwork. It has been a great pleasure working with him.

I want to extend my genuine appreciation to my advisory committee members, Dr. Dharani, Dr. Birman, Dr. Hilmas, and Dr. Samaranayake for their valuable time and advice in the review of this dissertation. I also wish to thank the assistance from my research group members.

I would like to acknowledge the financial support from Air Force Research Laboratory in the form of graduate research assistantship and from Department of Mechanical and Aerospace Engineering at Missouri University of Science and Technology for a graduate teaching assistantship.

Finally, I wish to express my deepest gratitude to my family, and my friends for their company, understanding, and encouragement. Without their support, I would not be able to accomplish and fulfill my dreams.

TABLE OF CONTENTS

LIST OF ILLUSTRATIONS

Page

PAPER I

PAPER II

LIST OF TABLES

Page

1. INTRODUCTION

Ceramic matrix composites (CMCs) are widely used in high temperature structural applications because of their lightweight and greater resistance to high temperature aggressive environments compared to metals or other engineering materials. Monolithic ceramics are inherently brittle, sensitive to process and service related flaws. These materials have high strength but low toughness often leading to catastrophic failures. Continuous fiber reinforced ceramic composites (CFCCs) have higher toughness and fail 'gracefully'. These materials have the ability to deform nonlinearly with applied load and show notch-insensitive strength behavior. The nonlinearity results from formation of matrix cracks, circumventing cracks around fibers, and fiber/matrix interface debonding. Unlike conventional monolithic ceramics, CFCCs can take more loads even after matrix failure. CFCCs can effectively redistribute stresses around notches, voids and cracks, thereby, increasing toughness of the material.

Toughness is an important factor complimenting the mechanical behavior of a CFCC and is dependent on the collective behavior of all constituents. In a metallic material, the toughness is governed by its ability to absorb energy by plastic deformation. Unlike metallic materials, the toughness behavior of CFCCs is from work of fracture required for,

- matrix failure – crack initiation and crack propagation
- fiber failure – fiber breakage
- fiber pull-out under frictional effects, and
- fiber/matrix interface debonding

Fiber/matrix interface is an important constituent in controlling the toughening mechanism of CFCCs. When the matrix cracks under application of an external load, the crack propagates and deflects into the fiber/matrix interface. Two things are likely to occur when the crack approaches the interface. The crack can either deflect into the interface or break the fiber. The former mechanism occurs when the interface is weak and the later occurs with a stronger interface. When a 'weak' interface is used the crack deflects into the interface, owing to its low strength and fracture toughness compared to the fiber. This process allows more work to be spent in propagating the crack through the

weak interface. During this whole process, the fibers in the CFCC, adjacent to debonded interface, can still contribute to load carrying behavior. Only after sufficient debonding has occurred, the fiber breaks and pull-out occurs. The frictional sliding during fiber pull-out increases the work of fracture. The crack propagates into the adjacent matrix and the process repeats until complete failure of material. Finite element modeling of RVE's has been conventionally done using fiber and matrix constituents only and ignoring the fiber/matrix interface. A perfect bond between the fiber and matrix was assumed by many researchers. However, the interface will have a significant impact on determining the mechanical properties of a CFCC and is explicitly modeled in this work.

In the current study, the mechanical behavior of a CFCC was studied in three different problems – mechanics of fiber pull-out, mechanical behavior evaluation using an RVE, and XFEM based failure study in a CFCC microstructure. Effect of interfaces was considered in these micromechnical models. Advanced numerical methods for crack initiation and propagation such as cohesive damage modeling and XFEM were used to study damage behavior in the microstructures.

2. LITERATURE REVIEW

Micromechanical modeling approaches predict overall behavior of the material from known properties of reinforcing and matrix constituent phases. Birman and Byrd [1] have provided an extensive review of damage in ceramic matrix composites. Lissart and Lamon [2] and Curtin et al. [3, 4] have provided a comprehensive study on damage behavior in unidirectional ceramic matrix composites. The statiscal variability of strengths in fibers and matrices, matrix cracking, effect of interface, and fiber failure were discussed in detail in their work.

Representative volume element (RVE) based micromechanical approaches are widely used for micromechanical modeling of composite materials. Sun and Vaidya [5] have detailed the procedure for determining composite properties from RVE. The authors have indicated that 'plane-remains-plane' boundary conditions are over-constrained boundary conditions. The effective determination of transverse shear modulus, unlike transverse Young's modulus, requires application of appropriate boundary conditions. This issue has been addressed by Xia et al. [6], Sun and Vaidya [5], and Li [7]. Finite element analysis has been used as a framework to conduct micromechanical analysis of composite materials by several researchers. Finite element RVE models are used to determine mechanical properties and also to study damage mechanisms of composites. Li [7] has applied finite element micromechanical models to unidirectional laminates and Xia et al. [8] have developed models for cross-ply laminates.

Cohesive damage modeling approaches can effectively model damage initiation and evolution using traction-separation laws. The use of cohesive elements in finite element RVE's has been explored by few researchers. Mishnaevsky and Brondsted [9] have used a cohesive damage modeling approach to investigate mechanical behavior and damage evolution of glass fiber reinforced composites. The authors have developed a code for automatic generation of 3D micromechanical unit cells of composites with damageable elements. The statistical variability of fiber strength, fiber/matrix interface debonding and other features have been embedded into the code. Numerical experiments have been conducted using the generated unit cell models to investigate different fiber packing geometries.

Experimental evaluation of interfacial properties in fiber reinforced composites using fiber pull-out tests has been investigated by several researchers [10-15]. However, analytical/numerical modeling of fiber pull-out tests has gained popularity subsequent to experimental testing due to cost and time saving advantages. Several theoretical models have been developed to predict the load-displacement behavior of fiber pull-out tests and the inherent interfacial properties [10, 16-19]. Stang and Shah [16] have proposed a simple model to predict the ultimate tensile strength of fiber-reinforced composites when the failure is governed by fiber debonding. Gao et al. [17] have studied the fiber/matrix debonding problem using a simple shear lag model, which includes friction at a debonded interface and Poisson contraction of the fiber. The authors have observed interfacial friction to have a significant effect on the debonding behavior. Further, the load-displacement relationship has been modeled in terms of interface toughness and frictional parameters of the interface. Hsueh [10] analyzed the non-linear dependence of stresses required to debond the fiber/matrix interface and for fiber pull-out as a function of embedded fiber length for a fiber-reinforced composite. The roles of residual clamping stresses at the interface, and Poisson contraction of the fiber, have been taken into consideration. Hutchinson and Jensen [18] have conducted a rigorous study on fiber pull-out of a fiber embedded in a brittle matrix and developed approximate closed form solutions. Residual compressive stresses acting across the fiber/matrix interface, a constant friction stress independent of normal compression across the interface, and coulomb friction have been considered in fiber debonding and pull-out models. Kerans and Parthasarathy [18] have developed fiber pull-out and push-out models to predict the load-displacement behavior in terms of the fiber/matrix interface parameters. The authors have found residual axial strain in the fiber to have a significant effect on fiber debonding and also included fiber surface topography in their model. The authors have suggested a methodology to extract interface parameters from experimental data.

Finite element modeling has been widely used to simulate fiber pull-out and understand various intricacies of the fiber/matrix interface debonding process [20-23]. Beckert and Lauke [20] have developed a comprehensive finite element model using a fracture mechanics debonding criterion to simulate the interface failure process of a single fiber pull-out test. The authors have made special emphasis on the local mixed-

mode load at the interface. Liu et al. [21] have developed finite element simulations for a single fiber pull-out process and obtained solutions for fiber axial stress, fiber displacement, and applied pull-out stress versus fiber displacement. The authors have adopted local shear strain criterion as the criterion for interface debonding. The effects of fiber pull-out rate, thermal residual stress, friction coefficient, and fiber volume fraction have been evaluated. Sun and Lin [22] have conducted parametric studies utilizing a fiber pull-out problem that includes a varying stiffness ratio for the fiber and matrix, and irregular fiber cross-sections. Wei et al. [23] have developed finite element models to investigate the interface shear stress distribution, and effects of shear stress transfer across the interface on interface debonding behavior.

The failure analysis of heterogeneous materials, accounting for damage initiation and evolution, has been explored by many researchers [24-30]. Advanced numerical methods have been developed to introduce an arbitrary discontinuity in the models for an effective analysis of material failure [30-33]. Cohesive damage models, based on traction-separation laws, were developed for simulating damage initiation and evolution. However, cohesive models require prior knowledge of crack paths. Numerical methods on treating arbitrary cracks without any prior knowledge of crack paths were first developed by Belytschko et al. [29, 32, 33, 34]. Crack tip enrichments were introduced for enhancing the nodal degrees of freedom, for effective description of element discontinuity displacement. This method is called as the extended finite element method (XFEM).

3. SCOPE AND OBJECTIVES

This dissertation comprises three papers corresponding to the following problems.

The first paper is titled "Modeling of Fiber Pull-Out in Continuous Fiber Reinforced Ceramic Composites using Finite Element Method and Artificial Neural Networks." In this paper, finite element models for the debonding of a silicon carbide fiber (SiC_f) embedded in silicon carbide matrix (SiC) are developed and analyzed. An axi-symmetric finite element model is developed to simulate the single fiber pull-out process and predict the load-displacement behavior in terms of fiber/matrix interface properties. A two-parameter cohesive damage modeling approach is coupled with a finite element model to simulate crack propagation during a fiber pull-out event. Parametric studies are conducted to evaluate the effects of thickness of specimen, friction coefficient, interface toughness, and residual stresses, on load-displacement behavior. An artificial neural network model using a backpropagation algorithm is proposed to mimic the fiber pull-out and also approximate load-displacement behavior. The developed finite element and neural network models are validated using existing analytical models from the technical literature.

The second paper is titled "Computational Study of Micromechanical Damage Behavior in Continuous Fiber-Reinforced Ceramic Composites." In this paper, a comprehensive numerical analysis of micromechanical damage behavior in a continuous fiber-reinforced ceramic composite (CFCC) is presented. A three-dimensional micromechanical finite element modeling procedure is proposed for effective elastic property estimation by the example of a composite consisting of a silicon carbide matrix unidirectionally reinforced with silicon carbide fiber (SiC/SiC_f). The effect of the fiber/matrix interface on predicted elastic properties of the SiC/SiC_f composite is considered. Representative volume element (RVE) models are developed for a SiC/SiC_f composite with damageable interfaces. Statistically equivalent RVE models with randomly distributed fibers are generated using a developed algorithm. The statistical variability of fiber and matrix strengths is considered in developing RVE models and assumed to follow a Weibull probability law. A user-material subroutine is developed to

predict damage behavior in the RVE. The predicted uniaxial stress vs. strain behavior and damage in the composite are discussed.

The third paper is titled “Microstructure Image-Based Multi-scale Modeling of Fracture in Continuous Fiber-Reinforced Ceramic Matrix Composites.” In this paper, A multi-scale modeling framework is developed for evaluating damage at the micro-level. An actual fiber/matrix topology, based on a SiC/SiC_f microstructure image, is used at the micro-level. A finite element mesh of the microstructure is generated using a object oriented finite element analysis tool. An extended finite element method, integrated with cohesive damage modeling, is used to study crack propagation in the microstructure. Finite element model validation using a baseline case study is discussed. The effect of cohesive parameters of individual phases on stress-displacement behavior in the micromechanical model is studied.

PAPER

I. MODELING OF FIBER PULL-OUT IN CONTINUOUS FIBER REINFORCED CERAMIC COMPOSITES USING FINITE ELEMENT METHOD AND ARTIFICIAL NEURAL NETWORKS

V. Bheemreddy[1], K. Chandrashekhara[1,*] L. Dharani[1], and G. Hilmas[2]

[1]*Department of Mechanical and Aerospace Engineering*

[2]*Department of Materials Science and Engineering*

Missouri University of Science and Technology, Rolla, MO 65409

ABSTRACT

Finite element models for the debonding of a silicon carbide fiber (SiC_f) embedded in silicon carbide matrix (SiC) are developed and analyzed. An axi-symmetric finite element model is developed to simulate the single fiber pull-out process and predict the load-displacement behavior in terms of fiber/matrix interface properties. A two-parameter cohesive damage modeling approach is coupled with a finite element model to simulate crack propagation during a fiber pull-out event. Effects of residual compressive stress acting across the fiber/matrix interface, and residual axial strain in the fiber, on fiber pull-out behavior are investigated. Poisson contraction of the fiber, which reduces resultant radial compressive stresses at the interface and interfacial frictional stress, is taken into consideration. Parametric studies are conducted to evaluate the effects of thickness of specimen, friction coefficient, interface toughness, and residual stresses, on load-displacement behavior. An artificial neural network model using a backpropagation algorithm is proposed to mimic the fiber pull-out and also approximate load-displacement behavior. A multilayer perceptron utilizing a nonlinear activation function is

implemented in the neural network model. Analytical modeling and finite element models are used to train and test the proposed neural network model. The developed finite element and neural network models are validated using existing analytical models from the technical literature.

1. INTRODUCTION

The mechanical behavior of continuous fiber reinforced ceramic composites is dependent on its constituent properties – fiber, matrix, and fiber/matrix interface [1]. The fiber/matrix interface can occur through a zero-thickness interface or an interphase region, and is a surface across which there is a discontinuity in one or more material properties [2]. In the former case, the interface is a common boundary between the reinforcing fibers and the matrix and is involved in transfer of loads. In the latter case, the interphase region constitutes an interfacial coating, is a finite volume region, enables proper load transfer, and protects the fibers from the service environment. In either case, the fiber/matrix interface is an unavoidable and inherent part of a composite [3, 4]. The nature of the interfacial bond between the fiber and matrix plays a profound role on the failure mechanisms in these composites. If the interfacial bond is strong, the oncoming crack will propagate unimpeded through the interface and the failure of the composite will occur catastrophically. On the other hand, if the interfacial bond is weak, the oncoming crack can experience interface debonding, followed by crack deflection, crack bridging, fiber breakage, and finally fiber pull-out. All these failure mechanisms lead to enhanced fracture toughness of the composite and graceful failure.

The characterization of an interface is a challenging problem. Several techniques have been developed to determine the mechanical properties of the interface. Fiber pull-out and push-out tests, which involve analyzing the response of a single fiber embedded in a matrix, are often adopted to study these interface properties. The theoretical models governing both test methods are similar, except that due to Poisson's effect, lateral contraction of the fiber is observed during pull-out tests while lateral expansion of the fiber is observed during push-out tests. In the case of a single fiber pull-out test, the test method of interest in the current study, a fiber embedded in a matrix material is pulled out under axial tension. This leads to interfacial debonding initiation at the surface, where the fiber enters the matrix and also the interfacial shear stresses are at a maximum [5]. For interfacial debonding to initiate, the applied stress on the fiber must overcome the bonding strength between the fiber and matrix. Residual stresses exist in the fiber and at the fiber/matrix interface due to thermal coefficient mismatch, and will influence the interfacial debonding behavior. Hence, after initial debonding of the interface, further debonding occurs when the applied stress exceeds the interfacial frictional stress. After complete debonding, fiber pull-out occurs when the applied stress overcomes the interfacial frictional stress along the total fiber length.

Experimental evaluation of interfacial properties in fiber reinforced composites using fiber pull-out tests has been investigated by several researchers [6-10]. However, analytical/numerical modeling of fiber pull-out tests has gained popularity subsequent to experimental testing due to cost and time saving advantages. Several theoretical models have been developed to predict the load-displacement behavior of fiber pull-out tests and the inherent interfacial properties [5, 11-14]. Stang and Shah [11] have proposed a simple

model to predict the ultimate tensile strength of fiber-reinforced composites when the failure is governed by fiber debonding. Gao et al. [12] have studied the fiber/matrix debonding problem using a simple shear lag model, which includes friction at a debonded interface and Poisson contraction of the fiber. The authors have observed interfacial friction to have a significant effect on the debonding behavior. Further, the load-displacement relationship has been modeled in terms of interface toughness and frictional parameters of the interface. Hsueh [5] analyzed the non-linear dependence of stresses required to debond the fiber/matrix interface and for fiber pull-out as a function of embedded fiber length for a fiber-reinforced composite. The roles of residual clamping stresses at the interface, and Poisson contraction of the fiber, have been taken into consideration. Hutchinson and Jensen [13] have conducted a rigorous study on fiber pull-out of a fiber embedded in a brittle matrix and developed approximate closed form solutions. Residual compressive stresses acting across the fiber/matrix interface, a constant friction stress independent of normal compression across the interface, and coulomb friction have been considered in fiber debonding and pull-out models. Kerans and Parthasarathy [14] have developed fiber pull-out and push-out models to predict the load-displacement behavior in terms of the fiber/matrix interface parameters. The authors have found residual axial strain in the fiber to have a significant effect on fiber debonding and also included fiber surface topography in their model. The authors have suggested a methodology to extract interface parameters from experimental data.

Finite element modeling has been widely used to simulate fiber pull-out and understand various intricacies of the fiber/matrix interface debonding process [15-18]. Beckert and Lauke [15] have developed a comprehensive finite element model using a

fracture mechanics debonding criterion to simulate the interface failure process of a single fiber pull-out test. The authors have made special emphasis on the local mixed-mode load at the interface. Liu et al. [16] have developed finite element simulations for a single fiber pull-out process and obtained solutions for fiber axial stress, fiber displacement, and applied pull-out stress versus fiber displacement. The authors have adopted local shear strain criterion as the criterion for interface debonding. The effects of fiber pull-out rate, thermal residual stress, friction coefficient, and fiber volume fraction have been evaluated. Sun and Lin [17] have conducted parametric studies utilizing a fiber pull-out problem that includes a varying stiffness ratio for the fiber and matrix, and irregular fiber cross-sections. Wei et al. [18] have developed finite element models to investigate the interface shear stress distribution, and effects of shear stress transfer across the interface on interface debonding behavior. Use of cohesive damage models, and its implementation in finite element modeling to simulate fiber/matrix interface debonding, has gained importance in the last decade [3, 19-20]. Cohesive damage modeling, which has the ability to simulate the crack initiation and subsequent propagation of an incipient crack, was first implemented by Dugdale [21] and Barenblatt [22]. Its finite element implementation was provided later by Hilleborg et al. [23]. Cohesive damage models rely on traction-separation laws to simulate crack initiation and crack propagation. Chandra [3] has implemented stress-based and energy-based failure criterion to model interface failure and provided a detailed discussion on using cohesive damage models to simulate failure/fracture of interfaces. Chandra et al. [19] have investigated the sensitivity of various cohesive zone parameters on overall interfacial mechanical response. Though the authors have used fiber push-out tests to analyze these

parameters, the discussion is well applicable for finite element modeling of fiber pull-out. The authors have indicated that the form of the traction-separation law for a cohesive damage model plays a significant role in determining the failure behavior. Alfano and Sacco [20] have combined interface damage and friction in a cohesive damage model and implemented it on finite element modeling of fiber push-out. The authors also validated their model with existing experimental results. Similar work on using cohesive damage modeling for interface debonding has been conducted by Lin et al. [24] and Pochiraju et al. [25].

Artificial Neural Networks (ANN), inspired by the biological nervous system, are extensively used to solve a wide range of complex scientific and engineering problems. ANN can be trained to provide solutions to non-linear and multi-dimensional problems without knowing anything about the problem nature. With its self-organizing capabilities, ANN can typically learn to adapt to any kind of data behavior. Though the application of ANN to the composite field is relatively minimal, it has the potential to solve a multitude of problems. The application of ANN in the composite field has been investigated by a few researchers [26-29]. Addin et al. [26] studied failure in laminated composites using ANN as a quantitative method, along with additional non-destructive methods. The authors were able to identify complex failures including delamination, matrix cracking, fiber fracture, and debonding. Zhang and Friedrich [27] and Kadi [28] reviewed various applications of ANN in the composite field including mechanical modeling of fiber reinforced composites and composite property prediction. Rao and Mukherjee [29] developed a novel approach using ANN to model the macromechanical behavior of

ceramic matrix composites. The authors used finite element models to investigate interfacial debonding and sliding, and then used these results to train the neural network.

The current work deals with modeling the fiber/matrix interface debonding and fiber pull-out behavior in continuous fiber reinforced ceramic composites using the example of a SiC/SiC_f composite. Finite element models utilizing cohesive damage modeling for interface debonding and fiber pull-out are developed. ANN is used to learn the load versus displacement behavior of fiber pull-out using analytical models and the finite element model. The developed finite element model and ANN model are validated by comparing with an existing analytical model. The novelty of this paper is in applying ANN to a fiber pull-out problem and has not been discussed in the published literature to the extent of the authors' knowledge, with the only exception being the work carried out by Rao and Mukherjee [29]. This paper is organized as follows. In section 2, a brief overview of the fiber pull-out process, and the equations governing various stages of fiber pull-out, are provided. A finite element model for fiber pull-out simulation, and a cohesive damage model, are detailed in section 3. In section 4, the ANN model is explained in detail including the training and testing sets. Results are discussed in section 5 and concluding remarks are presented in section 6.

2. FIBER PULL-OUT PROCESS – ANALYTICAL MODEL

Figure 1 shows a schematic of the fiber pull-out test configuration. Typically, the test configuration consists of a cylindrical fiber of radius 'r' protruding through a concentric cylinder of matrix having thickness 't'. The radius of the matrix cylinder is considered to be sufficiently high such that the effect of matrix on the load-displacement

behavior is virtually negligible. The matrix block is also gripped in a fashion such that the deformation is seen only in the immediate vicinity of the fiber. The fiber is loaded in uniaxial tension by applying an external displacement 'δ' on the free end of the fiber and the response load 'P_a' is measured. Figure 2 shows the schematic of the load-displacement behavior during the fiber pull-out process.

The typical load-displacement behavior constitutes four different regions, which will be explained in a later part of this section. The initial compliance is assumed to be due to the free length 'l_0' of the fiber, prior to the initiation of fiber/matrix interface debonding. After initiation of debonding, the compliance of the specimen increases with an increase in length of the strained fiber. This fiber/matrix interface debonding is viewed as a mode 2 interface fracture. When the debonding crack tip is approximately a few fiber diameters away from either end of the specimen surface, the crack propagation process is a stable process. In the presence of friction at the fiber/matrix interface, the stability is enhanced [14]. As the debond length 'l_d' is increased through the thickness of the specimen, incremental work is required to propagate the crack. When the debond length reaches a few fiber diameters from the lower end of the specimen surface, the shear stress at the interface is adequate to slip the remaining bonded length catastrophically. This is observed as a load drop in the load-displacement curve. Once the interface is completely debonded, the load drops to that required to slip the debonded fiber against friction. In the following sub-sections, the four regions of the load-displacement curve in a fiber pull-out process, and the associated governing equations, are explained. The analytical model used in the current work has been adopted from the extensive work by Kerans and Parthasarathy [14].

2.1 Criterion for initial debonding

As mentioned earlier, a part of the fiber protrudes out from the matrix block. For simplicity of discussion, prior to debond initiation, the fiber can be divided into two regions – (1) free length of the fiber 'l_0' and (2) bonded region 't'. When the free end of the fiber is subjected to external displacement 'δ', the deflection in the fiber is due to strain in region 1. The deflection of the fiber due to strain in region 2 is assumed to be negligible. Before the initial debonding, the equation that relates external displacement 'δ' and response load 'P_a' is given by,

$$\delta = \frac{l_0 P_a}{\pi r^2 E_f} \tag{1}$$

Here, E_f is the elastic modulus of fiber, l_0 is free length of fiber, and r is the radius of fiber. Equation 1 holds true until the fiber/matrix interface starts to debond. For debonding to initiate, the axial stress in the fiber at the region where the fiber enters the matrix block, has to exceed a critical value given by '$P_d/\pi r^2$'. A one-to-one correspondence between the axial stress in the fiber and the shear stress in the interface has been assumed. The initial debond is shown by point 'A' on the load-displacement curve (Figure 2). Sometimes, the debond initiation load is high such that it would reach point 'A^I' and then decreases, followed by progressive debonding. The initial debond load 'P_d' is related to the fracture toughness of the fiber/matrix interface 'G' and is given by,

$$P_d = \sqrt{\left(\frac{4\pi^2 r^3 E_f G}{1 - 2v_f k}\right)} \tag{2}$$

Equation 2 assumes no residual axial stress in the fiber and does not take friction into consideration. In Equation 2, v_f is the Poisson's ratio of fiber and k is a parameter relating elastic moduli and the Poisson's ratios of the fiber and the matrix, as given by,

$$k = \frac{E_m v_f}{E_f(1 + v_m) + E_m(1 - v_f)} \tag{3}$$

Here, E_m is the elastic modulus of matrix and v_m is the Poisson's ratio of the matrix.

2.2 Progressive debonding

When fiber/matrix interface debonding is initiated, the fiber can be divided into three regions – (1) free portion of the fiber, (2) debonded region 'l_d', and (3) bonded region '$t - l_d$'. The progressive debonding stage continues until the debond crack length reaches a few fiber diameters from the lower end of the specimen surface. This region of the load-displacement curve is nonlinear, unlike the part of the curve prior to debond initiation. In addition to the free portion of the fiber, the debonded region contributes to the compliance of the specimen. Additionally, the frictional resistance, residual normal stress at the interface, residual axial stress in the fiber, surface roughness, and Poisson's contraction of the fiber affect the load-displacement behavior of the fiber during progressive debonding. In this work, the effect of surface roughness along the fiber/matrix interface is ignored. Before the debond is initiated, due to the coefficient of thermal expansion mismatch, residual strains prevail both in the fiber and the matrix. This causes a residual normal (radial) stress 'σ_n' at the interface (Equation 4) and residual axial stress 'σ_r' in the fiber (Equation 5). When debonding is initiated, the residual strain is released and contributes to the external displacement of the fiber.

$$\sigma_n = \frac{-E_m E_f \Delta\alpha \Delta T}{E_f(1+v_m) + E_m(1-v_f)} \tag{4}$$

$$\sigma_r = \frac{P_r}{\pi r^2} = -(\Delta\alpha\Delta T) E_f \left(\frac{1+2k}{1-2v_f k}\right) \tag{5}$$

During the progressive debonding stage, crack propagation occurs when the axial stress in the fiber exceeds a critical stress given by '$(P_d + P_r)/\pi r^2$'. Also, there exists a critical load 'P^*' (Equation 6) which is the maximum load that can be applied externally. If the applied load approaches this critical load, the Poisson's contraction due to axial stress in the fiber cancels the radial normal stress and the frictional resistance does not exist.

$$P^* = -\frac{\sigma_n \pi r^2}{k} \tag{6}$$

However, it must be noted that the quantities '$(P_d + P_r)$' and 'P^*' are different from each other. If $P^* < (P_d + P_r)$, crack propagation through the specimen will occur at $(P_d + P_r)$. Otherwise, the applied load increases with crack length, asymptotically reaching the critical load. The external displacement and the applied load, during the progressive debonding, are related using the following expression.

$$\delta = \frac{l_0 P_a}{\pi r^2 E_f} + \frac{1-2v_f k}{2\mu k \pi r E_f}\left[P_d + P_r - P_a + (P^* - P_r)\, ln\left(\frac{P^* - (P_d + P_r)}{P^* - P_a}\right)\right] \quad \text{for } P^* > P_a > (P_d + P_r) \tag{7}$$

2.3 Load drop

As mentioned earlier, the progressive debonding stage ceases when the crack tip is close enough to the lower end. The shear stress at the interface is high enough such that the remaining bonded region '$t - l_c$' debonds catastrophically. Here 't' is the thickness of the specimen and 'l_c' is the critical debond length at the maximum load. The load drop

is calculated from the relation below, where '$P(x)$' gives the axial tension in the fiber at a distance 'x' from specimen surface.

$$P(x) = (P_a - P^*)exp\left[\frac{2\mu kx}{r}\right] + P^* \tag{8}$$

2.4 Fiber pull-out

Following the load drop, the fiber could have slipped a certain length. The embedded length of the fiber 'l_e' is then given by,

$$l_e = \frac{r}{2\mu k} ln\left(\frac{P^*}{P^* - P_a}\right) \tag{9}$$

The axial tension in the embedded length of the fiber is now given by,

$$P(x) = P^*\left\{1 - exp\left[-\frac{2\mu k(l_e - x)}{r}\right]\right\} \tag{10}$$

The external displacement of the fiber has three distinct regions: (1) the free portion of the fiber, (2) the portion of the fiber originally inside the matrix but now slipped out, and (3) the embedded region of the fiber. The relation between external displacement and applied load during fiber pull-out is given by,

$$\delta = \left(l_f - l_e\right) + \frac{P_a\left(l_0 + l_f - l_e\right)}{\pi r^2 E_f} + \frac{1 - 2v_f k}{2\mu k\pi r E_f}\left[P^* ln\left(\frac{P^*}{P^* - P_a}\right) - P_a\right] \tag{11}$$

Here, 'l_f'is the bonded length of the fiber measured after debonding and includes the change in length from the release of axial residual strain.

$$l_f = t\left\{1 - \frac{P_r\left(1 - 2v_f k\right)}{\pi r^2 E_f}\right\} \tag{12}$$

3. FINITE ELEMENT MODEL

The failure behavior of fiber/matrix interfaces are conventionally studied using a linear elastic fracture mechanics approach. In this approach, the local crack tip field is characterized using macroscopic parameters such as stress intensity factors ($K_I, K_{II}, \text{and } K_{III}$) or strain energy release rates ($G_I, G_{II}, \text{and } G_{III}$). These parameters are related to the corresponding fracture toughness of the material which determines the condition for initiation of crack growth. If the crack tip undergoes plastic yielding, these concepts based on theory of elasticity become inapplicable and a path dependent J integral is used [19]. If the energy at the crack tip region is converted to inelastic energy due to plasticity, the path independence property is lost. Also, traditional fracture mechanics approaches assume the existence of a sharp crack with stress levels locally approaching infinity. These crack tips are called singular crack tips. However, in reality, singular crack tips do not exist in materials. Cohesive zone modeling is an alternative to traditional fracture mechanics approaches and does not assume crack tip singularities. Cohesive models are phenomenological models used to effectively study crack propagation analyses. These methods are robust and can be easily implemented in finite element analyses.

A cohesive zone represents the region where the material separates. In a cohesive damage modeling approach, the crack initiation and propagation are governed by traction-separation laws across the crack faces and near the crack tip. The location of the cohesive zone is characterized by a mathematical tip and a physical tip [19]. The crack opening is zero in the mathematical tip and cohesive tractions are zero in a physical tip. When no loading is applied, the mathematical tip and physical tip coincide with each

other. Figure 3 gives the schematic of the cohesive zone in the crack region with a hypothetical mathematical crack tip, cohesive crack tip, and material crack tip. Cohesive zone modeling can be used to simulate crack propagation in a homogeneous material or in a bi-material interface. Unless otherwise mentioned, a 'cohesive zone' will refer to the 'fiber/matrix interface' hereafter.

As mentioned earlier, modeling of artificial cohesive zones in the crack domain is described using traction-separation laws. Figure 4 shows the schematic of a typical traction-separation law for modeling cohesive failure. In this work, a bilinear traction-separation law has been implemented. The shape of the traction separation curve '$T(\delta)$' can take several forms. A brief review of various traction-separation laws used by several authors has been provided by Chandra et al. [19]. The traction-separation law, also called a cohesive law, is characterized by a peak traction 'T_{max}' corresponding to a critical separation 'δ_{max}', and finally by a maximum separation parameter 'δ_{sep}'. The peak traction parameter corresponds to the cohesive strength of the interface. Each of these fracture parameters can uniquely affect the failure behavior of the interface. When the traction stresses are integrated over the separation of the interface, the result is the energy dissipated 'Γ_{sep}' by cohesive failure.

$$\Gamma_{sep} = \int_0^{\delta_{sep}} T(\delta)\, d\delta \tag{13}$$

In the present work, the cohesive zone model for simulating fiber/matrix interface debonding and fiber pull-out has been developed using a commercial finite element code (ABAQUS ver. 6.10) [31]. Figure 5 gives the schematic of the traction-separation

behavior at the interface of two element sets for various modes of fracture. The constitutive relation between these traction stresses and separation is given by,

$$T = \begin{Bmatrix} T_n \\ T_s \\ T_t \end{Bmatrix} = \begin{bmatrix} K_{nn} & K_{ns} & K_{nt} \\ & K_{ss} & K_{st} \\ sym & & K_{tt} \end{bmatrix} \begin{Bmatrix} \delta_n \\ \delta_s \\ \delta_t \end{Bmatrix} = K\delta \tag{14}$$

Here, T_n is the traction stress in the normal direction, T_s, T_t are traction stresses in the first shear and second shear directions, respectively, K is the nominal stiffness matrix, δ_n is the separation in the normal direction, and δ_s, δ_t are separations in the first shear and second shear directions, respectively. If the normal and shear components are uncoupled, equation 14 is reduced to,

$$\begin{Bmatrix} T_n \\ T_s \\ T_t \end{Bmatrix} = \begin{bmatrix} K_{nn} & 0 & 0 \\ & K_{ss} & 0 \\ sym & & K_{tt} \end{bmatrix} \begin{Bmatrix} \delta_n \\ \delta_s \\ \delta_t \end{Bmatrix} \tag{15}$$

The elastic stiffness and cohesive strength can be obtained from experiments or treated as penalty parameters (approximation). When a small stiffness value is used, it adds compliance to the model and affects the solution accuracy. If large stiffness values are used, the solver will have convergence issues. The principal diagonal terms are assumed to be equal to each other and initiated using a sufficiently large value based on a convergence analysis with various cases considered. Prior to damage initiation, the cohesive zone is governed by the portion of the traction-separation curve to the left of the vertical, dotted line. This implies that the traction stress increases in the cohesive zone until it reaches maximum traction 'T_{max}' which corresponds to the cohesive strength of the interface. For the initialization of damage in the cohesive zone, it has to satisfy certain damage initiation criterion. Several damage initiation criteria are available. In this work, the maximum stress criterion based damage initiation has been implemented as follows.

$$max\left\{\frac{T_n}{T_n^p}, \frac{T_s}{T_s^p}, \frac{T_t}{T_t^p}\right\} = 1 \tag{16}$$

In the above equation, T_n^p, T_s^p, and T_t^p are peak values of contact stress when the separation is either purely normal to the interface or purely in the first or the second shear direction, respectively. Once the damage has initiated, the damage evolution is described by introducing a stiffness degradation parameter, D, as below.

$$T_s = (1 - D)\overline{T_s} \tag{17}$$

Here, $\overline{T_s}$ is the contact stress component in first shear predicted by the traction-separation behavior for the current separation without damage. D is a scalar damage variable that represents the overall damage at the contact point. The value of D ranges from 0 (no damage) to 1 (complete damage) and can be described by either linear or exponential evolution. For linear softening, the evolution of damage variable 'D' is given by,

$$D = \frac{\delta^f(\delta^{max} - \delta^o)}{\delta^{max}(\delta^f - \delta^o)} \tag{18}$$

In Equation 18, δ^f is the effective separation at complete failure, δ^o is the effective separation at damage initiation, and δ^o is the maximum value of effective separation attained during loading history. Also, the effective separation at complete failure can be approximated by,

$$\delta^f = \frac{2G}{T_{eff}} \tag{19}$$

Here, G is the energy dissipated during failure, and T_{eff} is the effective traction at damage initiation. Using a cohesive damage modeling approach, an axi-symmetric finite element model of the fiber pull-out specimen has been generated. The finite element model of the fiber pull-out specimen and the boundary conditions are shown in Figure 6.

The radius of the fiber is 7 μm and that of matrix is 12.5 mm. Because the dimensions of the matrix are high compared to that of the fiber, only a part of the finite element model is shown in Figure 6. Both the fiber and the matrix have been modeled using four node bilinear axi-symmetric quadrilateral elements with reduced integration (CAX4R). The fiber/matrix interface is modeled like a zero thickness interface instead of an explicit interphase region (continuum). In this study, the properties of pyrolytic carbon (PyC) are assumed for the interface. A total of 11000 elements are used in the finite element mesh generation. To save computational time and without affecting the accuracy of the result, the mesh is chosen to be fine in the regions closer to the interface and coarse in the regions away from interface. The contact behavior of the fiber/matrix interface is modeled using a cohesive surface behavior. The equations governing the cohesive surface are similar to that of a cohesive element approach. Once the fiber/matrix interface is debonded, the contact friction at the interface is activated and influences the fiber slip/pull-out. A displacement controlled load has been applied on the free-end of fiber. The fiber displacement due to application of an external load, and the fiber/matrix interface debonding, followed by fiber pull-out have been simulated. A viscous regularization parameter (viscosity coefficient = 0.00001) has been used to overcome convergence difficulties that arise during material softening/stiffness degradation. The material properties and other input parameters required for the simulation are given in Table 1.

4. ARTIFICIAL NEURAL NETWORKS FOR FIBER PULL-OUT

Artificial Neural Networks (ANN) are a computational system that mimics the neurons of a biological nervous system. ANN are composed of simple elements operating in parallel and represent the clustering of artificial neurons. The topological structure of an ANN is comprised of neuron layers. Typically ANN have an input layer, output layer, and one or more hidden layers. These input neuron layers interface with the real world to capture the input, and the output layers provide the real world with network output [27]. The network function, usually a non-linear function, is determined by the interconnection between the neurons. Each neuron is associated with a weight factor that determines the strength of the interconnection. ANN are trained using available input/output data such that the network adjusts the values of these weight factors over iterations called epochs in ANN terminology. After several epochs, the network converges to training data that has been provided. This training step is repeated for multiple sets of input/output data and each time the weight factors are adjusted accordingly. This process when repeated over several training sets will result in an inherent optimized function that responds effectively to any similar input provided. After the network is trained, it is verified/validated using a set of test data. Once the ANN gives promising results with test data, it is said to be validated and can be used for any new input data, but is similar to the training/testing data. The above mentioned procedure of ANN is applied to a fiber pull-out problem using analytical models from the technical literature as a training/testing data set. A multilayer perceptron (MLP) neural network, along with a backpropagation algorithm, has been implemented to simulate the fiber pull-out behavior.

An MLP is a feedforward ANN model that maps sets of input data onto a set of appropriate output. An MLP consists of multiple layers of nodes in a directed graph which is fully connected from one layer to the next. MLPs are the oldest and most popular form of neural networks used today. They consist generally of three layers: an input layer, hidden layer, and an output layer. The specific one used in this study is shown in Figure 7. The ANN model was developed in MATLAB R2010a [33]. The network size used is 5 × 25 × 1 and has a total of 150 weights: 125 for the input-hidden layer, and 25 for the hidden-output layer. The inputs to the MLP are interface toughness, friction coefficient, specimen thickness, residual axial stress, residual normal stress, and a bias of 1. The output generated by the ANN model is the coordinates of the load-displacement curve. A linear activation function was used for both the input and output layers, and a sigmoid activation function was used for the hidden layer. A step by step procedure of the feedforward and back propagation operations in the ANN model is given below.

Step 1: Calculate the activation vector 'a_i'

$$a_i = \sum_{j=1}^{n} w_{ij} x_j \, , i = 1 \; to \; m \tag{20}$$

Here, x_j is the input vector, n is the number of inputs, w_{ij} is the weight function matrix for input-hidden layer, and m is the number of neurons in hidden layer.

Step 2: Calculate the decision vector 'd_i'

$$d_i = sigmoid(a_i) \tag{21}$$

The sigmoid activation function is given by,

$$sigmoid(a_i) = {}^{1}/_{(1 + e^{-(a_i)})} \tag{22}$$

Step 3: Calculate the output vector 'y_h'

$$y_h = \sum_{i=1}^{m} v_{hi} d_i \tag{23}$$

Here, h is the number of outputs.

Step 4: Calculate the output error vector 'E_y'. A least sum squared optimality criterion has been used between the predicted and desired values.

$$E_y = \sum_{p=1}^{k} \left(\widehat{y_{h,p}} - y_{h,p}\right)^2 \tag{24}$$

Here, k corresponds to the number of points on the load-displacement curve, and $\widehat{y_{h,p}}$ corresponds to the actual output calculated using finite element and analytical models.

Step 5: Calculate the decision error vector 'E_d'

$$E_d = {v_{hi}}^T E_y \tag{25}$$

Step 6: Calculate the activation error vector 'E_a'

$$E_a = d_i(1 - d_i)E_d \tag{26}$$

Step 7: Compute the weight changes for input-hidden layer '$\Delta w_{ij}(t)$' and hidden-output layer '$\Delta v_{hi}(t)$'

$$\Delta w_{ij}(t) = \gamma_g E_a(t) {x_j}^T(t) + \gamma_m \Delta w_{ij}(t-1) \tag{27}$$

$$\Delta v_{hi}(t) = \gamma_g E_y(t) {d_i}^T(t) + \gamma_m \Delta v_{hi}(t-1) \tag{28}$$

Here, t is learning iteration, γ_g is the learning gain, and γ_m is the momentum gain. The learning gain is a small parameter that adjusts the weight change each time, and the momentum gain reduces oscillations in the network model, ensuring rapid convergence.

Step 8: Compute the weight updates ''$w_{ij}(t+1)$' and ''$v_{hi}(t+1)$'

$$w_{ij}(t+1) = w_{ij}(t) + \Delta w_{ij}(t) \tag{29}$$

$$v_{hi}(t+1) = v_{hi}(t) + \Delta v_{hi}(t) \quad (30)$$

Equations 20 – 23 are used for the feedforward operation and Equations 24 – 30 are used for computing the back propagation operation. The analytical model and finite element model are run for several cases by varying the input parameters - interface toughness, friction coefficient, specimen thickness, residual axial stress, and residual normal stress. The interface toughness was varied from 1 J/m^2 to 10 J/m^2 at an interval of 0.25 J/m^2. Similarly, friction coefficient was varied from 0.05 to 0.15 at 0.005 intervals, and specimen thickness was varied from 2 mm to 10 mm at 0.5 mm intervals. Finally, residual axial stress was varied from 0 to 5 MPa at 0.5 MPa intervals, and residual normal stress was varied from 0 MPa to -30 MPa at 5 MPa intervals. A large input data set was developed by varying the above parameters one-factor-at-a-time. This input data set was used in a finite element model and an analytical model, to get the required output (load-displacement curve) data set. Using a random number generation, approximately 70% of the data of the whole data set was used for training the ANN model and the remaining data was used for testing. While selecting the training data set, care was taken to include 70% of the data from each of the variable data sets considered. This random number generation procedure will allow selecting random data without any bias, thereby making the ANN model more robust. The ANN model was trained for 10000 epochs to obtain a final sum of square error of less than 0.01. During the testing stage, the minimum sum of square error obtained was less than 0.1.

5. RESULTS AND DISCUSSION

The objective of this work is develop alternative numerical approaches to conventional analytical modeling for the investigation of the load-displacement behavior of fiber pull-out in continuous fiber reinforced ceramic matrix composites. Cohesive damage modeling based finite element models are developed to simulate fiber/matrix interface debonding and fiber pull-out. ANN based models are also developed, trained, and tested to mimic the load-displacement behavior for fiber pull-out. A parametric study has been conducted to compare the load-displacement behavior predicted by each of these approaches, and the sensitivity of various material parameters. The following parameters are analyzed in this study – (a) interface toughness, (b) friction coefficient, (c) specimen thickness, (d) residual axial stress in the fiber, and (e) residual normal stress. In this study, the effect of fiber surface irregularities on load-displacement behavior is not investigated.

Prior to investigating the influence of each of these parameters, the developed finite element model and ANN model are validated by comparing the predicted load-displacement behaviors with that of a widely used analytical model developed by Kerans and Parthasarathy [14]. Input parameters related to the geometry specifications of the fiber pull-out model, coefficient of friction, and residual normal stress are taken from the same reference. The fiber/interface/matrix configuration used in the study is Hi-Nicalon SiC_f/PyC/SiC. The radius of the fiber is 7 μm and the matrix radius is assumed to be 12.5 mm. The length of the free portion of the fiber is assumed to be 6 mm, and the thickness of the specimen is 3 mm. A coefficient of friction (μ) of 0.1 is used, and the residual normal stress (σ_n) is assumed to be -20 MPa. Other required inputs related to the material

properties are shown in Table 1. For the finite element model, displacement controlled loading is applied and the reactive forces at the free end of the fiber are captured. Figure 8 shows the fiber/matrix interface debonding and fiber pull-out simulated using the developed finite element model. The damage initiation is shown in Figure 8 (a), progressive debonding is shown in Figures 8 (b, c, d), and the fiber pull-out can be observed in Figures 8 (e, f). The ANN model could also predict the load-displacement behavior using the input parameters mentioned above. Figure 9 shows the comparison of the load-displacement behaviors predicted using the analytical model, finite element model, and the ANN model. The analytical model developed by Kerans and Parthasarathy [14] is referred to as the K-P model in the plot. In this case study, the critical load 'P^*' is less than the critical value for debonding '$P_d + P_r$'. This can be attributed to the thin fiber radius and also the high modulus of the SiC matrix. The initial debonding load '$P_d + P_r$' was sufficient to propagate the crack through the entire length of the specimen without requiring any additional load. Thus, the load-displacement behavior until the peak load was observed to be linear without any progressive debonding. The load-displacement behavior predicted using the finite element model and the ANN model were similar to that predicted using the analytical model. The peak load predicted using the finite element model was slightly lower and the predicted displacement at peak load was slightly higher. Following the peak load, the load dropped to near zero for the finite element model. The ANN model, which is now characteristic of the properties of the analytical model and the finite element model, has predicted the load-displacement curve displaying the combined behavior of both models. The peak loads predicted using the analytical model, finite element model, and ANN model were 0.0914 N, 0.0869 N,

and 0.0882 N, respectively. Considering the peak load predicted by the analytical model to be the reference, the finite element model had a relative error of 4.92 %, while the ANN model had a 3.5% relative error.

5.1 Effect of interface toughness on load-displacement behavior

The parameter 'interface toughness' primarily influences the debond initiation load. As mentioned earlier, progressive debonding was not observed in the predicted load-displacement behaviors and the Poisson effect was negligible. Figure 10 shows the load-displacement plots predicted using the analytical model, finite element model, and ANN model for two values of interface toughness – G = 2 J/m^2 and 6 J/m^2. The analytical model showed an increase in the debond initiation load or the peak load (in this study) with the increase in interface toughness. However, the difference in slopes of both the curves was minimal. The load drop was slightly higher for the case with higher toughness. The load-displacement plots captured using the finite element model and ANN model were similar to that of analytical model, although the slopes of the curves were slightly different. As observed earlier, the ANN model showed a combined behavior of both the analytical and finite element models.

5.2 Effect of friction coefficient on load-displacement behavior

The effect of friction coefficient on load-displacement is shown in Figure 11. The friction coefficients used in this analysis are μ = 0.05 and 0.1. The friction term is used in the analytical model to predict the peak load (Equation 8) during progressive debonding. In the absence of progressive debonding, the frictional coefficient is observed to have minimal effect on load vs. displacement, as predicted by the analytical model. Thus, it can be observed that the load-displacement plots predicted using the analytical model have overlapped. Contrary to this behavior, the load-displacement plots predicted using

the other two models are different for the two friction coefficients. Although the peak loads were close enough for the three models, it increased with an increase in friction coefficient (as predicted by both the finite element model and the ANN model). The load drop was observed to decrease with an increase in friction coefficient (ANN model). This behavior is similar to that observed by Kerans and Parthasarathy [14].

5.3 Effect of thickness of specimen on load-displacement behavior

The specimen thickness is another parameter, besides the friction coefficient, which affects the peak load during progressive debonding. For different specimen thicknesses, the length of the embedded fiber is increased/decreased which in turn increases/decreases the compliance of the specimen. Two specimen thicknesses, t = 3 mm and 6 mm, are considered for the analysis. Figure 12 shows the load-displacement plots for both the thicknesses. As expected, the analytical model resulted in similar load-displacement curves for both thickness values. However, an increase in peak load with an increase in specimen thicknesses was observed from the load-displacement plots obtained using the finite element model and the ANN model. Though the peak loads were predicted to be high using these models, the slope of the curves prior to peak load were similar for both thickness values.

5.4 Effect of residual axial stress in fiber on load-displacement behavior

The residual axial stress in the fiber would directly affect the critical value for interface debonding '$P_d + P_r$'. If the progressive debonding stage exists, the peak load predicted will be affected by the presence of residual axial stress. Figure 13 shows the effect of residual axial stress on the load-displacement behavior. Two cases are considered – (a) no residual axial stress 'σ_r=0', and (b) 'σ_r=1 MPa'. From the plots developed using the analytical model, it can be observed that the peak load is increased

slightly. Similar behavior is also observed from the plots developed using the finite element model and the ANN model. The frictional load after the load drop was almost the same, as predicted from the analytical model. However, as observed from the ANN model, the load drop was higher when there was no residual axial stress. The frictional pull-out load predicted by the finite element model was close to zero.

5.5 Effect of residual normal stress on load-displacement behavior

The residual normal stress parameter along with the Poisson contraction affects the frictional fiber slippage during interface debonding and frictional fiber pull-out. While a Poisson contraction decreases the frictional resistance, the residual normal stress (compressive) has the opposite effect. The effect of varying residual normal stress (σ_n = -20 MPa and -10 MPa) on predicted load-displacement behavior is shown in Figure 14. The peak load predicted from the analytical model was the same for both values of residual normal stress. However, the load drop was observed to be higher for σ_n = -10 MPa. The load-displacement patterns predicted by the other two models were similar to that predicted by the analytical model.

6. CONCLUSIONS

Finite element modeling and ANN models are developed to study the load-displacement behavior during fiber pull-out in continuous fiber reinforced ceramic composites. An axi-symmetric finite element model has been developed using a cohesive damage modeling approach integrated with frictional contact, for simulating the fiber/matrix interface debonding and frictional fiber pull-out. The finite element model has been validated by comparing with the analytical model. Numerical models were

developed using ANN concepts to mimic the load-displacement behavior during fiber pull-out. The ANN model was trained and tested using the analytical model and finite element model. The ANN model has shown good potential in near-accurately predicting the load-displacement behavior. With the availability of a larger data set of experimental results, the ANN model can be trained rigorously to capture the intricate details from experimental observations which otherwise are difficult to analyze using analytical models. A parametric study has been conducted to investigate the sensitivity of interface toughness, friction coefficient, specimen thickness, and residual stresses on the load-displacement behavior. For the material system considered in this study, the debond initiation load was observed to be high enough to completely debond the interface without an increase in load. The load-displacement behavior predicted by the analytical model, finite element model, and ANN model were observed to be similar for various parameters investigated in this study.

REFERENCES

1) R. D. Cordes and I. M. Daniel, "Determination of Interfacial Properties from Observations of Progressive Fiber Debonding and Pullout," Composites Engineering, Vol. 5, pp. 633-648, 1995.

2) K. K. Chawla, "Ceramic Matrix Composites," Kluwer Academic Publishers, Second Edition, Norwell, MA, USA, 2003.

3) N. Chandra, "Evaluation of Interfacial Fracture Toughness using Cohesive Zone Model," Composites: Part A, Vol. 33, pp. 1433-1447, 2002.

4) J. -K. Kim and Y. -W. Mai, "Engineered Interfaces in Fiber Reinforced Composites," Elsevier Science Ltd., First Edition, Kidlington, Oxford, U.K., 1998.

5) C. -H. Hsueh, "Interfacial Debonding and Fiber Pull-Out Stresses of Fiber-Reinforced Composites," Materials Science and Engineering, Vol. A123, pp. 1-11, 1990.

6) S. Zhandarov and E. Mader, "Characterization of Fiber/Matrix Interface Strength: Applicability of Different Tests, Approaches and Parameters," Composites Science and Technology, Vol. 65, pp. 149-160, 2005.

7) C. DiFrancia, T.C. Ward, and R. O. Claus, "The Single-Fibre Pull-Out Test. 1: Review and Interpretation," Composites Part A: Applied Science and Manufacturing, Vol. 27, pp. 597-612, 1996.

8) V. M. C. F. Cunha, J. A. O. Barros, and J. M. Sena-Cruz, "Pullout Behavior of Steel Fibers in Self-Compacting Concrete," Journal of Materials in Civil Engineering, Vol. 22, pp. 1-9, 2010.

9) A. J. G. Jurewicz, R. J. Kerans, and J. Wright, "The Interfacial Strengths of Coated and Uncoated SiC Monofilaments Embedded in Borosilicate Glass," Ceramic Engineering and Science Proceedings, Vol. 10, pp. 925-937, 1989.

10) E. P. Butler, E. R. Fuller, and H. M. Chan, "Interface Properties for Ceramic Composites from a Single Fiber Pull-Out Test," Materials Research Society Symposium Proceedings, Vol. 170, pp. 17-24, 1990.

11) H. Stang and S. P. Shah, "Failure of Fiber-Reinforced Composites by Pull-Out Fracture," Journal of Material Science, Vol. 21, pp. 953-957, 1986.

12) Y. C. Gao, Y. -W. Mai, and B. Cotterell, "Fracture of Fiber Reinforced Materials," Journal of Applied Mathematics and Physics, Vol. 39, pp. 550-572, 1988.

13) J. W. Hutchinson and H. M. Jensen, “Models of Fiber Debonding and Pullout in Brittle Composites with Friction,” Mechanics of Materials, Vol. 9, pp. 139-163, 1990.

14) R. J. Kerans and T. A. Parthasarathy, “Theoretical Analysis of the Fiber Pullout and Pushout Tests,” Journal of American Ceramic Society, Vol. 74, pp. 1585-1596, 1991.

15) W. Beckert and B. Lauke, “Critical Discussion of the Single-Fibre Pull-Out Test: Does it Measure Adhesion?” Composites Science and Technology, Vol. 57, pp. 1689-1706, 1997.

16) H. -Y. Liu, X. Zhang, Y. -W. Mai, and X. -X. Diao, “On Steady-state Fiber Pull-Out Computer Simulation,” Composites Science and Technology, Vol. 59, pp. 2191-2199, 1999.

17) W. Sun and F. Lin, “Computer Modeling and FEA Simulation for Single Fiber Pull-Out,” Journal of Thermoplastic Composite Materials, Vol. 14, pp. 327-343, 2001.

18) G. Wei, G. Liu, C. Xu, and X. Sun, “Finite Element Simulation of Perfect Bonding for Single Fiber Pull-Out Test,” Advanced Materials Research, Vol. 418-420, pp. 509-512, 2012.

19) N. Chandra, H. Li, C. Shet, and H. Ghonem, “Some Issues in the Application of Cohesive Zone Models for Metal-Ceramic Interfaces,” International Journal of Solids and Structures, Vol. 39, pp. 2827-2855, 2002.

20) G. Alfano and E. Sacco, “Combining Interface Damage and Friction in a Cohesive-Zone Model,” International Journal for Numerical Methods in Engineering, Vol. 68, pp. 542-582, 2006.

21) D. S. Dugdale, “Yielding of Steel Sheets containing Slits,” Journal of the Mechanics and Physics of Solids, Vol. 8, pp. 100-104, 1960.

22) G. I. Barenblatt, “The Mathematical Theory of Equilibrium Cracks in Brittle Fracture,” Advances in Applied Mechanics, Vol. 7, pp. 55-129, 1962.

23) A. Hilleborg, M. Modeer, and P. E. Petersson, “Analysis of Crack Formation and Crack Growth in Concrete by Means of Fracture Mechanics and Finite Elements,” Cement and Concrete Research, Vol. 6, pp. 773-782, 1976.

24) G. Lin, P. H. Geubelle, and N. R. Sottos, “Simulation of Fiber Debonding with Friction in a Model Composite Pushout Test,” International Journal of Solids and Structures, Vol. 38, pp. 8547-8562, 2001.

25) K. V. Pochiraju, G. P. Tandon, and N. J. Pagano, "Analysis of Single Fiber Pushout Considering Interfacial Friction and Adhesion," Journal of the Mechanics and Physics of Solids, Vol. 49, pp. 2307-2338, 2001.

26) A. O. Addin, S. M. Sapuan, E. Mahdi, and M. Othman, "Prediction and Detection of Failures in Laminated Composite Materials Using Neural Networks - A Review," Polymers & Polymer Composites, Vol. 14, pp. 433-441, 2006.

27) Z. Zhang and K. Friedrich, "Artificial Neural Networks Applied to Polymer Composites: A Review," Composites Science and Technology, Vol. 63, pp. 2029-2044, 2003.

28) H. E. Kadi, "Modeling the Mechanical Behavior of Fiber-Reinforced Polymeric Composite Materials Using Artificial Neural Networks - A Review," Composite Structures, Vol. 73, pp. 1-23, 2006.

29) H. S. Rao and A. Mukherjee, "Artificial Neural Networks for Predicting the Macromechanical Behavior of Ceramic-Matrix Composites," Computational Material Science, Vol. 5, pp. 307-322, 1996.

30) A. Cornec, I. Scheider, and K. -H. Schwalbe, "On the Practical Application of the Cohesive Zone Model," Engineering Fracture Mechanics, Vol. 70, pp. 1963-1987, 2003.

31) ABAQUS/Standard User's Manual, Vol. I and II (ver. 6.10), 2010. Hibbit, Karlsson and Sorensen, Inc., Pawtucket, Rhode Island.

32) S. Liu, L. Zhang, X. Yin, L. Cheng, and Y. Liu, "Microstructure and Mechanical Properties of SiC and Carbon Hybrid Fiber Reinforced SiC Matrix Composite," International Journal of Applied Ceramic Technology, Vol. 8, pp. 308-316, 2011.

33) MATLAB version 7.10.0. Natick, Massachusetts: The MathWorks Inc., 2010.

Table 1 Material properties for finite element modeling [32]

Material		Modulus (GPa)	Tensile Strength (MPa)	Poisson's Ratio	Fracture Energy (J/m^2)
Fiber	Hi-Nicalon SiC_f	270	2800	0.2	20
Matrix	SiC Matrix	350	-	0.21	6
Interface (Cohesive Zone)	PyC	Penalty Parameters		-	2-6

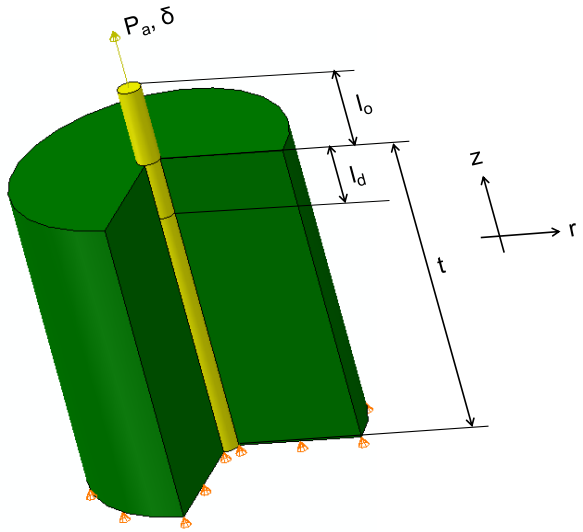

Figure 1 Schematic of pull-out test configuration

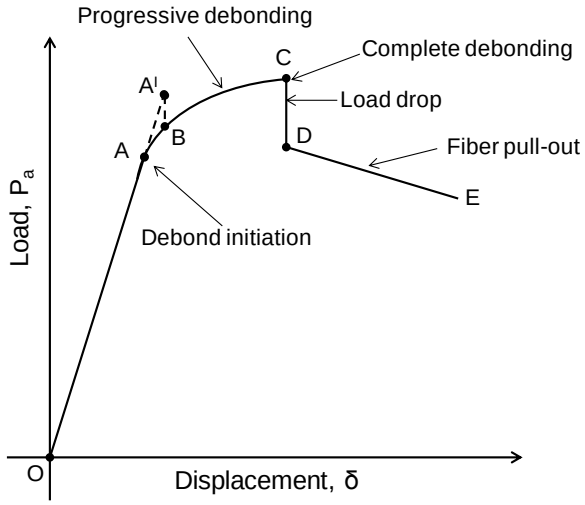

Figure 2 Typical load-displacement behavior during a fiber pull-out process

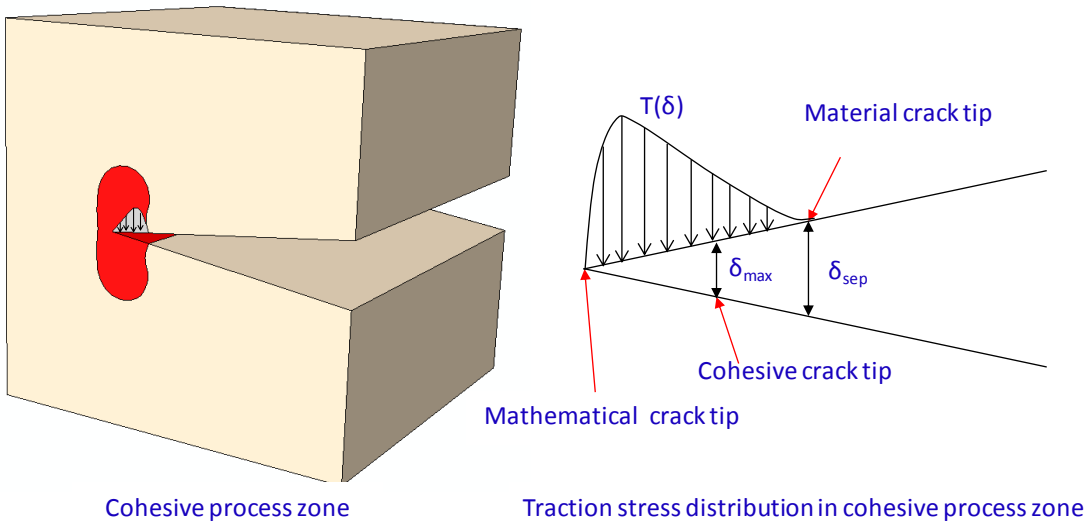

Figure 3 Schematic of a cohesive zone in a cracked material

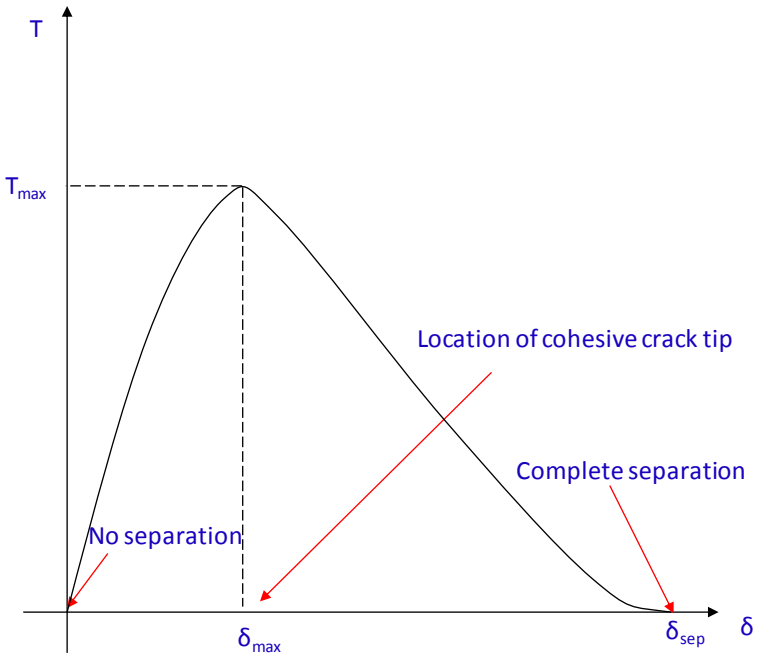

Figure 4 Typical traction-separation law for modeling cohesive failure

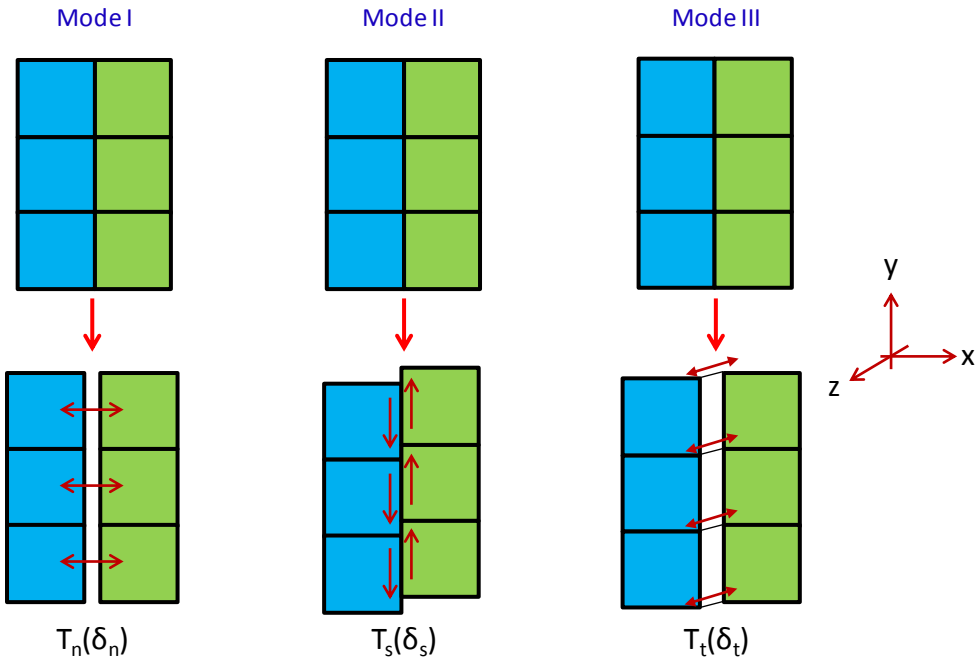

Figure 5 Traction-separation distribution in finite elements for three fracture modes

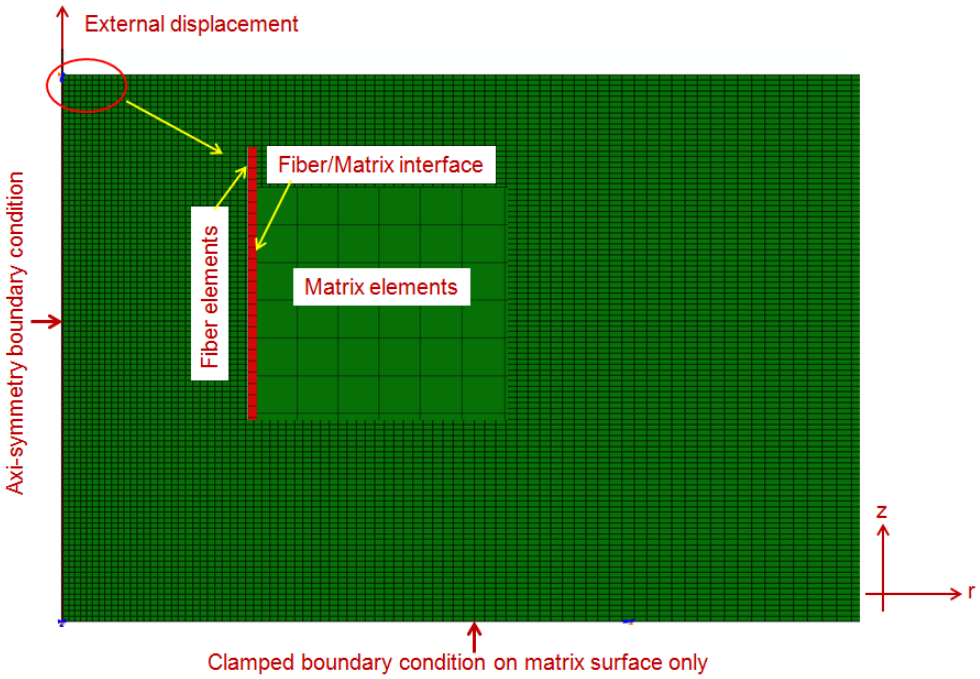

Figure 6 Finite element model of fiber pull-out specimen

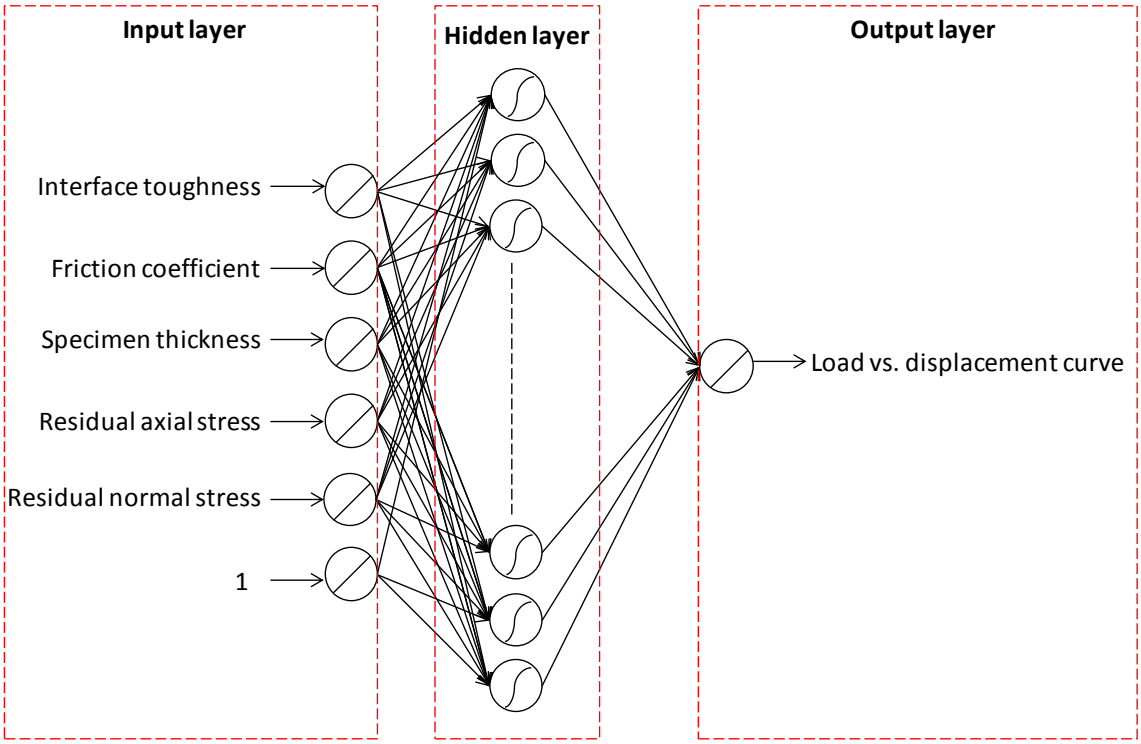

Figure 7 ANN model of fiber pull-out

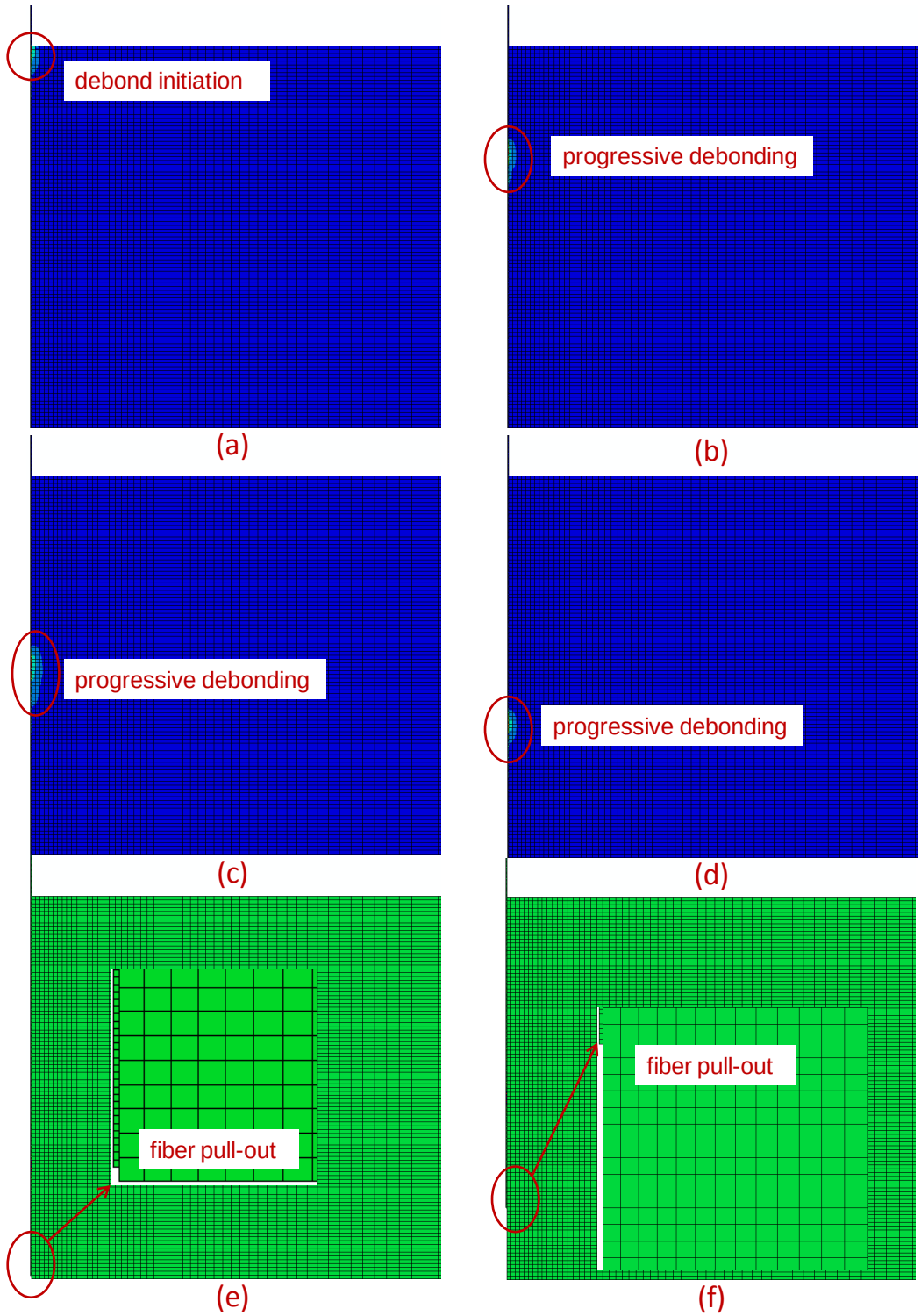

Figure 8 Fiber/matrix interface debonding (a-d) and fiber pull-out (e-f)

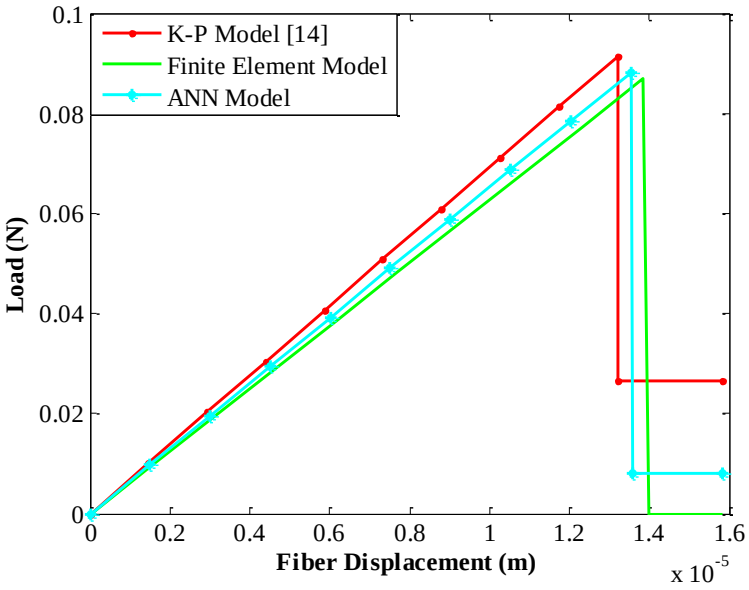

Figure 9 Comparison of finite element results and ANN results with analytical model

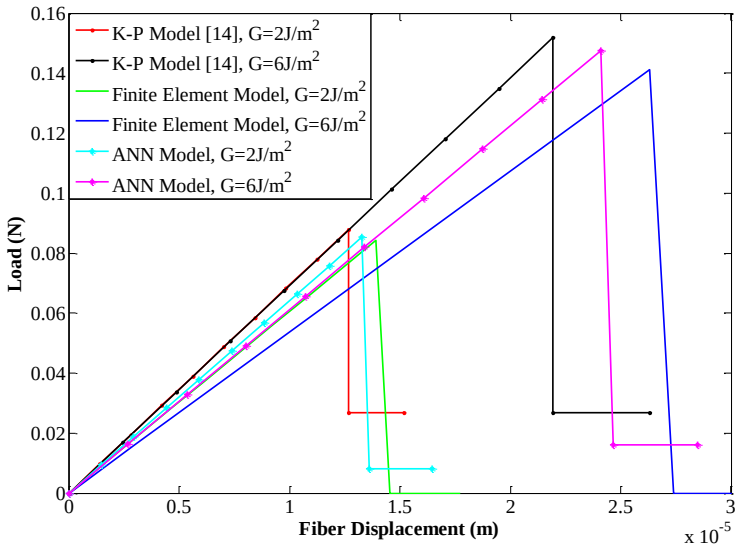

Figure 10 Load-displacement plots for varying interface toughness

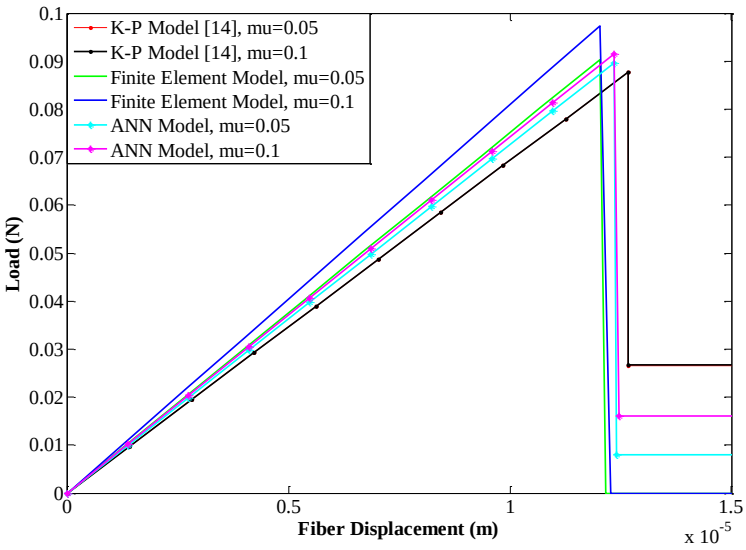

Figure 11 Load-displacement plots for varying coefficient of friction

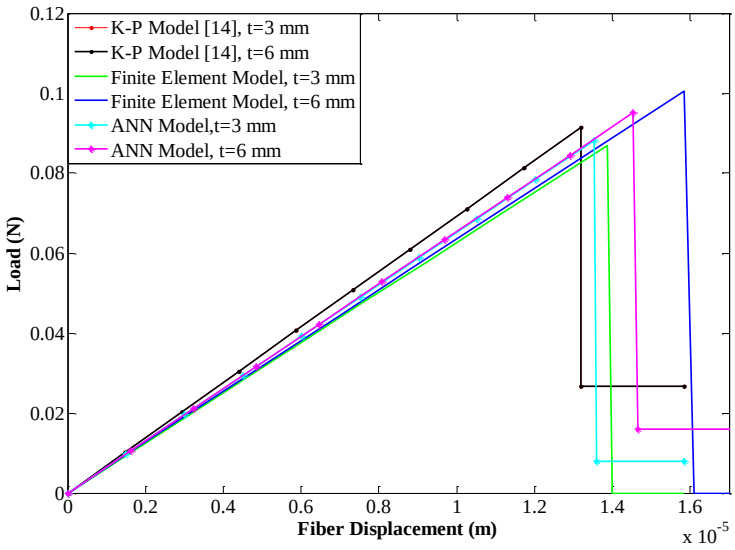

Figure 12 Load-displacement plots for varying specimen thickness

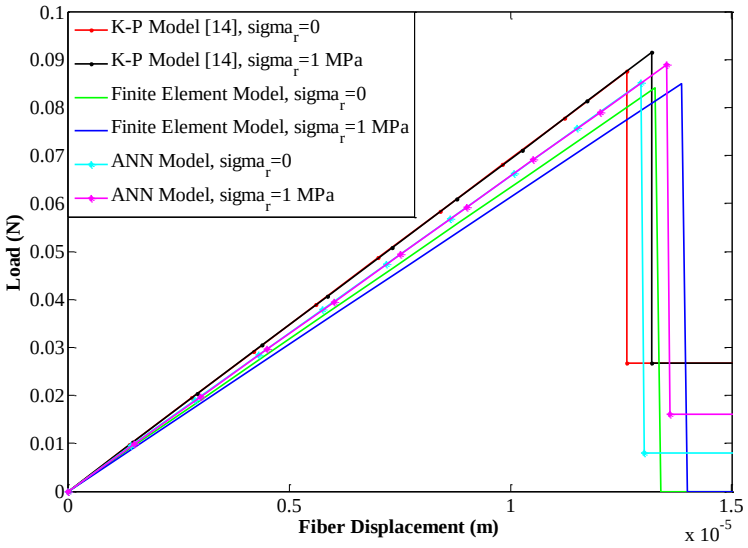

Figure 13 Load-displacement plots for studying the effect of residual axial stress

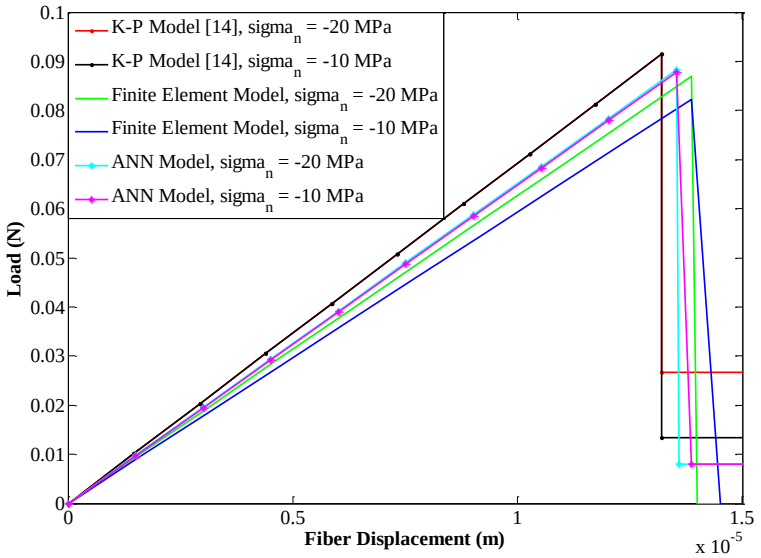

Figure 14 Load-displacement plots for studying the effect of residual normal stress

II. COMPUTATIONAL STUDY OF MICROMECHANICAL DAMAGE BEHAVIOR IN CONTINUOUS FIBER-REINFORCED CERAMIC COMPOSITES

V. Bheemreddy[1], K. Chandrashekhara[1,*] L. R. Dharani[1], and G. E. Hilmas[2]

[1]*Department of Mechanical and Aerospace Engineering*

[2]*Department of Materials Science and Engineering*

Missouri University of Science and Technology, Rolla, MO 65409

ABSTRACT

A comprehensive numerical analysis of micromechanical damage behavior in a continuous fiber-reinforced ceramic composite (CFCC) is presented. A three-dimensional micromechanical finite element modeling procedure is proposed for effective elastic property estimation by the example of a composite consisting of a silicon carbide matrix unidirectionally reinforced with silicon carbide fiber (SiC/SiC_f). The effect of fiber/matrix interface on predicted elastic properties of the SiC/SiC_f composite is considered. Representative volume element (RVE) models are developed for SiC/SiC_f composite with damageable interfaces. Statistically equivalent RVE models with randomly distributed fibers are generated using a developed algorithm. The statistical variability of fiber and matrix strengths is considered in developing RVE models and assumed to follow a Weibull probability law. A user-material subroutine is developed to predict damage behavior in the RVE. The predicted uniaxial stress vs. strain behavior and damage in the composite are discussed.

1. INTRODUCTION

Ceramic matrix composites (CMCs) are widely used in high temperature structural applications because of their lightweight and greater resistance to high temperature aggressive environments compared to metals or other engineering materials [1, 2]. Monolithic ceramics are inherently brittle, sensitive to process and service related flaws. These materials have high strength but low toughness often leading to catastrophic failure. Continuous fiber reinforced ceramic composites (CFCCs) have higher toughness and fail 'gracefully'. These materials have the ability to deform nonlinearly with applied load and show notch-insensitive strength behavior. The nonlinearity results from formation of matrix cracks, crack propagation around reinforcing fibers, and fiber/matrix interface debonding with frictional sliding. Unlike conventional monolithic ceramics, CFCCs can take more load even after matrix failure. CFCCs can effectively redistribute stresses around notches, voids and cracks, thereby, increasing toughness [3].

Several researchers have worked on evaluating mechanical properties of composites using micromechanical models [4-15]. Micromechanical modeling approaches predict overall behavior of the material from known properties of reinforcing and matrix constituent phases. Birman and Byrd [4] have provided an extensive review of damage in ceramic matrix composites. Lissart and Lamon [5] and Curtin et al. [6, 7] have provided a comprehensive study on damage behavior in unidirectional ceramic matrix composites. The statiscal variability of strengths in fibers and matrices, matrix cracking, effect of interface, and fiber failure were discussed in detail in their work. Chateau et al. [8] have developed and experimentally validated a 1D probablistic model of damage evolution in unidirectional SiC/SiC composites.

Representative volume element (RVE) based micromechanical approaches are widely used for micromechanical modeling of composite materials. RVE is the basic unit or element of a material capturing all details of macrostructure. Often RVE's are referred to as repeating unit cells (RUC's) for composites; RUC's are used to model materials which show periodic behavior. Raghavan et al. [13] have developed a mathematical representation for periodic composite materials called 'asymptotic homogenization theory'. Sun and Vaidya [10] have detailed the procedure for determining composite properties from RVE. The authors have indicated that 'plane-remains-plane' boundary conditions are over-constrained boundary conditions. The effective determination of transverse shear modulus, unlike transverse Young's modulus, requires application of appropriate boundary conditions. This issue has been addressed by Xia et al. [9], Sun and Vaidya [10], and Li [11]. Finite element analysis has been used as a framework to conduct micromechanical analysis of composite materials by several researchers. Finite element RVE models are used to determine mechanical properties and also to study damage mechanisms of composites. Li [11] has applied finite element micromechanical models to unidirectional laminates and Xia et al. [12] have developed models for cross-ply laminates.

Finite element RVE's for composite materials are usually modeled as damage-free. The fiber/matrix interface in the CFCCs is a critical factor affecting its toughness behavior. The toughness of composite materials is dependent on the crack propagation behavior. The greater the crack growth resistance, more energy is spent in propagating the crack and thus enhancing its toughness. For crack growth resistance to be high, the fiber/matrix interface has to be 'weak' [16, 17]. Conventionally used finite element RVE

models ignore the interfaces and assume a perfect bond between the fiber and matrix. In order to accurately predict the mechanical properties of the composite material fiber/matrix interface in addition to fiber and matrix has to be considered.

Cohesive damage modeling approaches can effectively model damage initiation and evolution using traction-separation laws. The use of cohesive elements in finite element RVE's has been explored by few researchers. Mishnaevsky and Brondsted [18] have used a cohesive damage modeling approach to investigate mechanical behavior and damage evolution of glass fiber reinforced composites. The authors have developed a code for automatic generation of 3D micromechanical unit cells of composites with damageable elements. The statistical variability of fiber strength, fiber/matrix interface debonding and other features have been embedded into the code. Numerical experiments have been conducted using the generated unit cell models to investigate different fiber packing geometries. Wang et al. [19] have used an extended finite element method technique to effectively model damage initiation and propagation in a unidirectional glass fiber reinforced epoxy composite subjected to tensile load. The authors have considered both single fiber and multi fiber unit cells to investigate the case study.

In the current work, statistically equivalent RVE models for a unidirectionally reinforced SiC/SiC_f composite are developed. These models are used to predict the elastic constants and damage behavior of the composite from known properties of the fiber, matrix, and interface. The finite element models are validated by comparing the results with available data from the literature. The paper is organized into six sections. The mechanics of failure in the CFCCs is presented in the second section. The third section provides details on generating a statistically equivalent RVE. The finite element

modeling procedure for predicting elastic constants and damage behavior is detailed in the fourth section. Discussion of results and conclusions are presented in fifth and sixth sections, respectively.

2. MECHANICS OF FAILURE IN CFCC$_S$

CFCCs are increasingly being considered for advanced aerospace and nuclear applications. Unlike monolithic (unreinforced) ceramics, CFCCs fail in a 'graceful' manner. The non-catastrophic failure behavior in these materials is due to large work of fracture required for crack initiation and propagation [17]. The mechanical behavior of CFCCs is controlled by the constituent (fiber, matrix, and interface) properties. Toughness is an important factor complimenting the mechanical behavior of a CFCC and is dependent on the collective behavior of all constituents. In a metallic material, the toughness is governed by its ability to absorb energy by plastic deformation. Unlike metallic materials, the toughness behavior of CFCCs is from work of fracture required for [20],

- matrix failure – crack initiation and crack propagation
- fiber failure – fiber breakage
- fiber pull-out under frictional effects, and
- fiber/matrix interface debonding

The various mechanisms of crack energy dissipation in a CFCC are shown in Figure 1.

Fiber/matrix interface is an important constituent in controlling the toughening mechanism of CFCCs. When the matrix cracks under application of an external load, the

crack propagates and proceeds to the fiber/matrix interface. Two things are likely to occur when the crack approaches the interface. The crack can either deflect along the interface or continue in its original propagation direction and break the fiber. The former mechanism occurs when the interface is weak and the latter occurs with a stronger interface. When a 'weak' interface is used the crack deflects into the interface, owing to its low strength and fracture toughness compared to the fiber. This process allows more work to be spent in propagating the crack through the weak interface. During this whole process, the fibers in the CFCC, adjacent to debonded interface, can still contribute to load carrying behavior. Only after sufficient debonding has occurred, the fiber breaks and pull-out occurs. The frictional sliding during fiber pull-out increases the work of fracture. The crack propagates into the adjacent matrix and the process repeats until complete failure of material. Finite element modeling of RVE's has been conventionally done using fiber and matrix constituents only and ignoring the fiber/matrix interface. A perfect bond between the fiber and matrix has been assumed by many researchers. However, the interface will have a significant impact on determining the mechanical properties of a CFCC and is explicitly modeled in this work.

3. STATISTICALLY EQUIVALENT RVE

In this section, a three-step procedure is detailed for automatic generation of a statistically equivalent RVE model with randomly distributed fibers. Figure 2 shows the flow chart of the algorithm developed for random distribution of fibers. This algorithm was implemented in MATLAB R2010. The developed RVE model can be easily transferred to a commercial finite element tool for developing finite element models.

3.1 Step 1: Generation of square RVE

In order to generate a statistically equivalent RVE with random fiber distribution, an RVE with square packing was selected as an initial distribution. Several algorithms were previously developed for generating the random distribution of fibers [21, 22]. Most of these algorithms involved a single fiber as the starting point and generated multiple fibers one after the other to develop an RVE. These algorithms were sometimes limited by the maximum volume fraction produced. This phenomenon is called 'jamming'. Unlike these, the algorithm presented here has the advantage of starting with an RVE that has a fixed fiber volume fraction. The parameters that were input to the algorithm included fiber volume fraction (V_f), radius of fiber (r), and number of fibers (N). All fibers were assumed to have the same radius. From these inputs, the side (S) of the RVE was calculated as,

$$S = \sqrt{\frac{N\pi r^2}{V_f}} \tag{1}$$

A square frame was generated using Eq. 1 and the fibers were uniformly distributed in the square domain. Figure 3(a) shows the generated RVE with square packing.

3.2 Step 2: Global crisscrossing

This step involves assigning new positions to the fibers by randomly moving the fibers within the square domain. The random movement of fibers was limited by global constraints imposed on the fiber positions. The constraints used in the algorithm were,

1) The minimum distance (d_{min}) between centers of any two neighboring fibers was equal to $2r + 2w$. Here, r is the radius of fiber and w is the thickness of the interface. This constraint will prevent any overlapping of fibers.

2) The maximum distance (d_{max}) between centers of any two neighboring fibers was equal to $4r$. This value was arbitrarily selected due to limited data availability in the literature. However, it can be replaced by experimentally observed inter-fiber distances.

3) The position of any fiber was restricted to the square domain.

4) In addition to the above constraints, the movement of any fiber in the square domain was limited to small increments. This will prevent localized accumulation of fibers after several iterations. This constraint was imposed using the following equations,

$$x_i(t+1) = x_i(t) + [a + (b-a) * rand] \quad (1)$$

$$y_i(t+1) = y_i(t) + [a + (b-a) * rand] \quad (2)$$

Here, (x_i, y_i) corresponds to the center of the i^{th} fiber, t is the iteration count, *'rand'* is a function in MATLAB and was used to generate a random number between 0 and 1. In Eq. 1 and Eq. 2, '$rand$' was used to generate a random number between a and b. The values of a and b were arbitrarily selected as -0.5 and 0.5, respectively, to avoid large increments in new positions. By selecting $a = -b$, the fiber was allowed to move in all possible directions.

By imposing the above constraints, the modified RVE after several iterations of global crisscrossing is shown in Figure 3(b).

3.3 Step 3: Sub-frame selection

In this step, a square sub-frame was randomly generated within the main domain (original square frame) to create a statistically equivalent RVE. All the fibers within this

sub-frame correspond to the new RVE. The RVE generated in Step 1 and Step 2 is similar to the microstructure of a composite (transverse cross-section of unidirectional composite) with a fiber volume fraction and large number of randomly distributed fibers. The sub-frame selected in this step is then similar to any statistically equivalent RVE generated from the microstructure. Similar to Step 2, constraints were applied on the sub-frame such that the sub-frame domain was within the bounds of the main domain. Figure 4 shows the sub-frame selected from the main domain to generate the desired statistically equivalent RVE.

4. FINITE ELEMENT MODEL

In this section, the finite element model development of an RVE with randomly distributed fibers in a matrix, modeling of the fiber/matrix interface, properties of constituent phases, numerical homogenization procedure for predicting elastic constants, and the damage model based on Weibull probability of failure are detailed.

4.1 Finite element model of RVE

A comprehensive three-dimensional finite element model of the RVE was developed using commercial finite element code Abaqus ver. 6.12. The fiber/matrix interface was explicitly modeled as an interphase region. Figure 5 illustrates the developed finite element model of RVE. The randomized fiber distribution of the RVE was developed based on the procedure explained in section 3. A code was written in Python to import the coordinate points obtained from Matlab and develop a transverse cross-section of the RVE in Abaqus. With an increase in the number of fibers, the randomized distribution is well accounted for, however, it will increase the computational

cost. Similarly, if the number is less, the computational time is reduced but the randomization will not result in effective results. Accordingly, the cross-section was selected to include at least nine fibers. The three-dimensional model was then realized by extruding the transverse cross-section in the longitudinal direction. Due to its complex structure, the RVE was modeled with a combination of hexahedral and tetrahedral elements. The hexahedral elements form the majority of the elements and to reduce the computational time, a reduced integration scheme with hourglass control was used. The hexahedral configuration corresponds to eight-node linear brick elements with reduced integration and enhanced hourglass control (C3D8R). Similarly, the tetrahedral elements refer to a four node linear tetrahedron (C3D4).

4.2 Properties of constituent phases

Isotropic linear elastic behavior was considered for modeling individual phases - fiber, matrix, and fiber/matrix interface. Typically, brittle materials experience a large scattering of strengths owing to their random distribution of flaws, such as cracks [4-7]. This scattering of strengths in fiber and matrix phases is taken into account using a Weibull probability law. The Weibull probability law gives the probability of failure 'P_f' for a volume 'V' of a material at a stress level 'σ'.

$$P_f(\sigma) = 1 - exp\left[-\frac{V}{V_0}\left(\frac{\sigma - \sigma_u}{\sigma_0}\right)^m\right] \quad (2)$$

The probability of failure ranges from 0 to 1. In Eq. 2, V_0 (=1 mm3) is a reference volume used for fitting Weibull parameters to experimental data, σ_u is stress below which no failure occurs, σ_0 is a Weibull strength parameter, and m is a Weibull shape parameter. The Weibull shape parameter describes the statistical spread in material strength. The higher the value of Weibull shape parameter, the lesser is the scatter in

material strengths. In ceramic materials, failure cannot be excluded even with lower stresses and thus the parameter σ_u is zero. Eq. 2 is reduced to,

$$P_f(\sigma) = 1 - exp\left[-\frac{V}{V_0}\left(\frac{\sigma}{\sigma_0}\right)^m\right] \tag{3}$$

The elastic constants and Weibull parameters for each of the material phases are provided in Table 1 [8, 23].

4.3 Numerical homogenization

Numerical homogenization is a procedure for predicting the elastic properties of the composite from available elastic properties of the constituents. This procedure involves applying appropriate boundary conditions on the finite element model of the RVE for estimating elastic properties of a composite. In general, composites reinforced with fibers arranged in parallel show orthotropic behavior at the mesoscale (Figure 6(a)). However, with the statistically equivalent RVE (random fiber arrangement) considered in this work, the mesoscale behavior is transversely isotropic (Figure 6(b)).

For a homogeneous composite material, the relationship between average stress ($\bar{\sigma}$) and average strain ($\bar{\varepsilon}$) is given by,

$$\{\bar{\sigma}\} = [C]\{\bar{\varepsilon}\} \tag{4}$$

Here, $[C]$ is the stiffness tensor. For a transversely isotropic material, the stiffness tensor is given by,

$$[C_{ij}] = \begin{bmatrix} C_{11} & C_{12} & C_{12} & 0 & 0 & 0 \\ C_{12} & C_{22} & C_{23} & 0 & 0 & 0 \\ C_{12} & C_{23} & C_{22} & 0 & 0 & 0 \\ 0 & 0 & 0 & \frac{C_{22} - C_{23}}{2} & 0 & 0 \\ 0 & 0 & 0 & 0 & C_{66} & 0 \\ 0 & 0 & 0 & 0 & 0 & C_{66} \end{bmatrix} \tag{5}$$

Here, the 1-axis is aligned with the fiber direction. The goal is to find the five independent elastic properties (longitudinal and transverse Young's moduli, longitudinal and transverse Poisson's ratio, and longitudinal shear modulus) of a homogeneous material by computing the components of this transversely isotropic stiffness tensor. The shear modulus in the transverse plane can be directly obtained from the transverse Young's modulus and transverse Poisson's ratio. In order to evaluate the stiffness tensor, six components of strain (${\varepsilon_{ij}}^{a}$) are applied by enforcing the following displacement (u_i) boundary conditions [24].

$$u_i(l, x_2, x_3) - u_i(-l, x_2, x_3) = 2l{\varepsilon_{i1}}^{a}, \quad -m \le x_2 \le m \ \ and \ \ -n \le x_3 \le n \tag{6}$$

$$u_i(x_1, m, x_3) - u_i(x_1, -m, x_3) = 2m{\varepsilon_{i2}}^{a}, \quad -l \le x_1 \le l \ \ and \ \ -n \le x_3 \le n \tag{7}$$

$$u_i(x_1, x_2, n) - u_i(x_1, x_2, -n) = 2n{\varepsilon_{i3}}^{a}, \quad -l \le x_1 \le l \ \ and \ \ -m \le x_2 \le m \tag{8}$$

The superscript 'a' denotes applied strain while the over-line in Eq. 1 indicates volume average. In Eq. 6, Eq. 7 and Eq.8, $2l{\varepsilon_{ij}}^{a}$, $2m{\varepsilon_{ij}}^{a}$, and $2n{\varepsilon_{ij}}^{a}$ indicate the displacements required for enforcing a strain ${\varepsilon_{ij}}^{a}$ on an RVE with sides $2l$, $2m$, and $2n$, respectively (Figure 7).

The strain ${\varepsilon_{ij}}^{a}$ applied on the RVE results in a complex state of stress, however, the volume average of strain ($\bar{\varepsilon}_{ij}$) in the RVE equals the applied strain.

$$\bar{\varepsilon}_{ij} = \frac{1}{V}\int_V \varepsilon_{ij} dV = {\varepsilon_{ij}}^{a} \tag{9}$$

Here, V is the volume of the RVE. By applying the boundary conditions (Eq. 6, Eq. 7 and Eq.8) one at a time, only one strain component of Eq. 1 will be non-zero and all other components are made zero. If the applied strain (${\varepsilon_{ij}}^{a}$) is given a unit value, the

components of the stiffness tensor can be computed from the volume averaged stress ($\bar{\sigma}$) in the RVE.

$$C_{ij} = \bar{\sigma}_{ij} = \frac{1}{V}\int_V \sigma_{ij}(x_1, x_2, x_3)dV, \;\; {\varepsilon_{ij}}^a = 1 \tag{10}$$

The step by step procedure for evaluating each column of the stiffness tensor, by imposing appropriate boundary conditions, is explained in the following sub-sections.

Computing first column of the stiffness tensor: A unit strain is applied on the RVE in the fiber direction (x_1) to compute the stiffness tensor components C_{i1} with i = 1 to 3.

$${\varepsilon_{11}}^{\mathrm{a}} = 1 \qquad {\varepsilon_{22}}^{\mathrm{a}} = {\varepsilon_{33}}^{\mathrm{a}} = {\varepsilon_{23}}^{\mathrm{a}} = {\varepsilon_{13}}^{\mathrm{a}} = {\varepsilon_{12}}^{\mathrm{a}} = 0 \tag{11}$$

The displacement boundary conditions corresponding to the above applied strain are given by (Figure 8),

$$u_1(l, x_2, x_3) = 2l, \quad -m \le x_2 \le m \;\; and \;\; -n \le x_3 \le n \tag{12}$$

$$u_1(-l, x_2, x_3) = 0, \quad -m \le x_2 \le m \;\; and \;\; -n \le x_3 \le n \tag{13}$$

$$u_2(x_1, m, x_3) = 0, \quad -l \le x_1 \le l \;\; and \;\; -n \le x_3 \le n \tag{14}$$

$$u_2(x_1, -m, x_3) = 0, \quad -l \le x_1 \le l \;\; and \;\; -n \le x_3 \le n \tag{15}$$

$$u_3(x_1, x_2, n) = 0, \quad -l \le x_1 \le l \;\; and \;\; -m \le x_2 \le m \tag{16}$$

$$u_3(x_1, x_2, -n) = 0, \quad -l \le x_1 \le l \;\; and \;\; -m \le x_2 \le m \tag{17}$$

Computing second column of the stiffness tensor: A unit strain is applied on the RVE in the transverse direction (x_2) to compute the stiffness tensor components C_{i2} with i = 1 to 3.

$${\varepsilon_{22}}^{\mathrm{a}} = 1 \qquad {\varepsilon_{11}}^{\mathrm{a}} = {\varepsilon_{33}}^{\mathrm{a}} = {\varepsilon_{23}}^{\mathrm{a}} = {\varepsilon_{13}}^{\mathrm{a}} = {\varepsilon_{12}}^{\mathrm{a}} = 0 \tag{18}$$

The displacement boundary conditions corresponding to the above applied strain are given by (Figure 9),

$$u_1(l, x_2, x_3) = 0, \quad -m \le x_2 \le m \ \ and \ \ -n \le x_3 \le n \tag{19}$$

$$u_1(-l, x_2, x_3) = 0, \quad -m \le x_2 \le m \ \ and \ \ -n \le x_3 \le n \tag{20}$$

$$u_2(x_1, m, x_3) = 2m, \quad -l \le x_1 \le l \ \ and \ \ -n \le x_3 \le n \tag{21}$$

$$u_2(x_1, -m, x_3) = 0, \quad -l \le x_1 \le l \ \ and \ \ -n \le x_3 \le n \tag{22}$$

$$u_3(x_1, x_2, n) = 0, \quad -l \le x_1 \le l \ \ and \ \ -m \le x_2 \le m \tag{23}$$

$$u_3(x_1, x_2, -n) = 0, \quad -l \le x_1 \le l \ \ and \ \ -m \le x_2 \le m \tag{14}$$

Computing third column of the stiffness tensor: A unit strain is applied on the RVE in the transverse direction (x_3) to compute the stiffness tensor components C_{i3} with i = 1 to 3.

$$\varepsilon_{33}{}^{a} = 1 \qquad \varepsilon_{11}{}^{a} = \varepsilon_{22}{}^{a} = \varepsilon_{23}{}^{a} = \varepsilon_{13}{}^{a} = \varepsilon_{12}{}^{a} = 0 \tag{24}$$

The displacement boundary conditions corresponding to the above applied strain are given by (Figure 10),

$$u_1(l, x_2, x_3) = 0, \quad -m \le x_2 \le m \ \ and \ \ -n \le x_3 \le n \tag{25}$$

$$u_1(-l, x_2, x_3) = 0, \quad -m \le x_2 \le m \ \ and \ \ -n \le x_3 \le n \tag{26}$$

$$u_2(x_1, m, x_3) = 0, \quad -l \le x_1 \le l \ \ and \ \ -n \le x_3 \le n \tag{27}$$

$$u_2(x_1, -m, x_3) = 0, \quad -l \le x_1 \le l \ \ and \ \ -n \le x_3 \le n \tag{28}$$

$$u_3(x_1, x_2, n) = 2n, \quad -l \le x_1 \le l \ \ and \ \ -m \le x_2 \le m \tag{29}$$

$$u_3(x_1, x_2, -n) = 0, \quad -l \le x_1 \le l \ \ and \ \ -m \le x_2 \le m \tag{30}$$

Computing fourth column of the stiffness tensor: For a transversely isotropic material, the fourth column of stiffness tensor has only one component C_{44} which does

not require computation as in previous cases. The component C_{44} can be calculated as a function of other components given by,

$$C_{44} = \frac{C_{22} - C_{23}}{2} \tag{31}$$

Computing fifth and sixth columns of the stiffness tensor: A unit strain is applied on the $x_3 = n$ face of the RVE in the longitudinal direction (x_1) to compute the stiffness tensor component C_{66}.

$$\varepsilon_{13}{}^{a} = 1 \qquad \varepsilon_{11}{}^{a} = \varepsilon_{22}{}^{a} = \varepsilon_{33}{}^{a} = \varepsilon_{23}{}^{a} = \varepsilon_{12}{}^{a} = 0 \tag{32}$$

The boundary conditions for this case are not similar to those used for computing the first three columns. In this case, periodicity boundary conditions are applied on the $x_1 = -l$ and $x_1 = l$ faces. If these conditions are not enforced, the applied boundary conditions do not lead to a unit average strain. The boundary conditions required for computing C_{66} are shown in Figure 11.

$$u_1(l, x_2, x_3) - u_1(-l, x_2, x_3) = 0, \quad -m \le x_2 \le m \ \ and \ \ -n \le x_3 \le n \tag{33}$$

$$u_2(x_1, m, x_3) = 0, \quad -l \le x_1 \le l \ \ and \ \ -n \le x_3 \le n \tag{34}$$

$$u_2(x_1, -m, x_3) = 0, \quad -l \le x_1 \le l \ \ and \ \ -n \le x_3 \le n \tag{35}$$

$$u_1(x_1, x_2, n) = 2n, \quad -l \le x_1 \le l \ \ and \ \ -m \le x_2 \le m \tag{36}$$

$$u_1(x_1, x_2, -n) = 0, \quad -l \le x_1 \le l \ \ and \ \ -m \le x_2 \le m \tag{37}$$

$$u_3(x_1, x_2, n) = 0, \quad -l \le x_1 \le l \ \ and \ \ -m \le x_2 \le m \tag{38}$$

$$u_3(x_1, x_2, -n) = 0, \quad -l \le x_1 \le l \ \ and \ \ -m \le x_2 \le m \tag{39}$$

Once all the components of stiffness tensor are computed, the elastic constants can be calculated using the following relations,

$$E_1 = C_{11} - \frac{2C_{12}^2}{(C_{22} + C_{23})} \tag{40}$$

$$E_2 = E_3 = \frac{[C_{11}(C_{22} + C_{23}) - 2C_{12}^2](C_{22} - C_{23})}{(C_{11}C_{22} - C_{12}^2)} \tag{41}$$

$$\nu_{12} = \nu_{13} = \frac{C_{12}}{(C_{22} + C_{23})} \tag{42}$$

$$\nu_{23} = \frac{(C_{11}C_{23} - C_{12}^2)}{(C_{11}C_{22} - C_{12}^2)} \tag{43}$$

$$G_{12} = G_{13} = C_{66} \tag{44}$$

$$G_{23} = \frac{C_{22} - C_{23}}{2} = \frac{E_2}{2(1 + \nu_{23})} \tag{45}$$

4.4 Damage modeling using a user-material subroutine

The damage evolution of the fiber and matrix was modeled by integrating Weibull probability of failure with a finite element weakening method. For the fiber/matrix interface the damage was modeled using interface shear strength as the failure criterion. The damage modeling of constituent phases of the RVE was implemented in Abaqus ver. 6.12 using a user-material subroutine (UMAT). This subroutine was used as the built-in material models cannot be used to define a specific material behavior. The UMAT subroutine was called at each integration point in the model, and the stresses and tangent stiffness matrix were updated at each increment. A viscous regularization parameter (viscosity coefficient = 0.0001) was used to overcome any convergence difficulties during material softening/stiffness degradation [25].

Before calling the UMAT subroutine, random probabilities ($0< P_f <1$) were generated at each integration point in the finite element model using a SDVINI subroutine. Figure 12 shows the contour of random probabilities generated in the RVE, which are indicative of respective failure strengths. These probabilities were generated

only once during the initial increment and stored for the rest of the analysis using solution dependent state variables. The probabilities generated in the initial increment were called in UMAT to generate a random strength distribution for fiber and matrix elements. Equation 2 was reorganized in terms of stress to calculate random strengths (corresponding to generated probabilities) at each material point. The random strengths were stored in a solution dependent state variable and were not updated when UMAT was called at each increment. The damage evolution in the fiber and matrix was modeled using a damage variable. The maximum stress criterion was used for modeling failure in the fiber and matrix. A damage variable ($0<D<1$) was defined in UMAT by initializing to zero, and updating to 0.99 when the failure criterion was satisfied. The stiffness matrix in Eq.5 was defined as a product of $(1-D)$, and individual stiffness terms, such that the stiffness of the element (material) reduces to 0.0001% of the initial value when the failure criterion is satisfied [18].

5. RESULTS AND DISCUSSION

5.1 Elastic constants

Figure 13 shows the transverse cross-section of 12 different statistically equivalent RVE models generated using the procedure developed in section 3. Each of these models was used to predict elastic constants of the resulting transversely isotropic composite. The elastic modulus and Poisson's ratio provided in Table 1 were used as input to the finite element model. No strength data was used for predicting the elastic constants. The loads and boundary conditions applied in these models followed the numerical homogenization procedure detailed in section 4.3. A python code was

developed to calculate volume averaged stress and strain in the model by extracting stresses and strains at each integration point. The developed python code was also used to calculate all the stiffness terms in the stiffness matrix (Eq. 10) and finally the elastic constants (Eq. 40 – Eq. 45). Table 2 shows the predicted elastic constants from each RVE model, mean and standard deviation. Figure 14 shows the stress distribution in the RVE model corresponding to different loading conditions for predicting stiffness terms.

The results predicted using the statistically equivalent RVE models were compared with results generated from Chamis model [26]. The Chamis model is a widely used analytical model for predicting elastic constants of a transversely isotropic, unidirectionally reinforced fiber composite [27]. However, this model does not take elastic behavior of the interface in to account. Table 3 shows the comparison of elastic constants predicted from the current model and the Chamis model. The variation of longitudinal Young's modulus and Poisson's ratios was less than 3%, while the transverse Young's modulus was off by 8%. The longitudinal and transverse shear moduli varied by 5.8% and 7.7%, respectively. The experimentally observed longitudinal Young's modulus was 350 GPa, as provided by Chateau et al. [8]. The deviation of the predicted longitudinal Young's modulus was 3.23% in comparison to the experimentally observed data.

5.2 Stress vs. strain and damage behavior

A damage model was developed using the procedure outlined in section 4.4. This model was used to predict the stress-strain behavior of a unidirectionally reinforced SiC/SiC_f composite under uniaxial tension. The elastic properties and Weibull parameters provided in Table 1 were used as input to the model. Under uniaxial tension, the stress levels increased with the applied load, and matrix elements which were weak (low

strength) started to fail. When the stress in an element exceeded its material strength (randomly generated from Weibull probability law - Eq. 12) the damage variable increased from 0 to 0.99. Accordingly, the stiffness of the element reduced to 1% of its initial value. When a matrix element failed, local load sharing with adjacent elements was observed, which increased the stresses in these elements. Similarly, when a matrix element adjacent to an interface element failed, shear stress build up in the interface element was observed. As shown in Table 1, the interface has low shear strength, and failed accordingly when stresses exceeded this value. As the crack (damage) evolved from matrix elements to interface elements, stress levels in adjacent fiber elements increased due to local load sharing. Similar to matrix and interface elements, the fiber elements failed when the failure criterion was satisfied. Figure 15 shows the predicted stress-strain behavior based on the developed damage model. The maximum predicted stress and strain were 1254 MPa and 0.57% respectively. The matrix cracking has saturated at ~621 MPa and beyond this point the observed stress-strain behavior was primarily fiber dependent. The developed finite element model was validated by comparing with experimentally observed stress-strain behavior from the literature [8]. The experimental data had a maximum stress of 1198 MPa and a failure strain of 0.63%. The predicted stress-strain curve showed brittle behavior in comparison to experimentally observed data. The deviation of predicted failure stresses and strains from experimental data was found to be 4.7% and 9.5%, respectively. This difference is assumed to be attributed to any voids or defects present in the tested specimens.

The stress-strain behavior of the composite is influenced by Weibull strength and shape parameters. Among the parameters used for fiber and matrix, the Weibull strength

of the matrix was often discussed in the literature [5-7]. The effect of this parameter on the stress-strain behavior was evaluated in this study. Table 1 gives the baseline value (278 MPa) of Weibull strength for the matrix. Two other values, 225 MPa and 175 MPa, were used to study the effect and were then compared against baseline results. Figure 16 shows the stress-strain behavior of the composite at three different Weibull strengths. Matrix modulus and Weibull shape were left unchanged. With the decrease in Weibull strengths, a brittle (low failure strain) to tough (high failure strain) transition was observed. This behavior was in good agreement with the results presented by Curtin et al. [6]. As predicted, matrix cracking was saturated at lower stress levels when compared to the baseline value, and the fiber dominance of failure strain was more realized. At a Weibull strength of 225 MPa, the failure strength was reduced by 4.07%, and failure strain increased by 3.51%. Similarly, for a Weibull strength of 175 MPa, the failure strength was reduced by 8.56%, and failure strain increased by 17.54%.

6. CONCLUSIONS

A new algorithm was developed to generate statistically equivalent RVE models. The fiber/matrix interface was explicitly defined in these models. The elastic and damage properties of fiber, matrix, and interface of a unidirectionally reinforced SiC/SiC_f composite were used in the study. Elastic properties of the unidirectional composite were estimated using the developed RVE models and validated using an analytical model. The deviation of predicted longitudinal Young's modulus and Poisson's ratios from analytical results was less than 3%. The longitudinal and transverse shear moduli varied by 5.8% and 7.7%, respectively. The transverse Young's modulus had a maximum deviation of

8%. The predicted longitudinal Young's modulus was also compared with an experimentally observed value from the literature and was off by 3.23%, while the analytical model was off by 5.61%. A damage model was developed and integrated with the RVE model using a user-material subroutine. Weibull probability of failure was used to account for the distribution of strengths in brittle fiber and matrix materials. The stress vs. strain behavior of a composite under a uniaxial tensile load was predicted using the damage model. The finite element results were validated using the stress vs. strain experimental data from the literature. The predicted failure stresses and strains varied from the experimental data by 4.7% and 9.5%, respectively. The effect of matrix Weibull strength on stress vs. strain behavior was studied. A brittle (low failure strain) to tough (high failure strain) transition was observed when the Weibull strength parameter was reduced.

REFERENCES

1) Z. Xia and W. Curtin, "Tough-to-Brittle Transitions in Ceramic-Matrix Composites with Increasing Interfacial Shear Stress," Acta Materialia, Vol. 48, pp. 4879-4892, 2000.

2) P. Liaw, "Continuous Fiber Reinforced Ceramic Composites," Journal of the Chinese Institute of Engineers, Vol. 21, pp. 701-718, 1998.

3) K. Dassios, V. Kostopoulos, and M. Steen, "A Micromechanical Bridging Law Model for CFCCs," Acta Materialia, Vol. 55, pp. 83-92, 2007.

4) V. Birman and L. Byrd, "Review of Fracture and Fatigue in Ceramic Matrix Composites," Applied Mechanical Reviews, Vol. 53, pp. 147-174, 2000.

5) N. Lissart and J. Lamon, "Damage and Failure in Ceramic Matrix Minicomposites: Experimental Study and Model," Acta Materialia, Vol. 45, pp. 1025-1044, 1997.

6) W. Curtin, B. Ahn, and N. Takeda, "Modeling Brittle and Tough Stress-Strain Behavior in Unidirectional Ceramic Matrix Composites," Acta Materialia, Vol. 46, pp. 3409-3420, 1998.

7) W. Curtin, "Multiple Matrix Cracking in Brittle Matrix Composites," Acta Metallurgica et Materialia, Vol. 41, pp. 1369-1377, 1993.

8) C. Chateau, L. Gelebart, M. Bornert, J. Crepin, D. Caldemaison, and C. Sauder, "Modeling of Damage in Unidirectional Ceramic Matrix Composites and Multi-scale Experimental Validation on Third Generation SiC/SiC Minicomposites," Journal of the Mechanics and Physics of Solids, Vol. 63, pp. 298-319, 2014.

9) Z. Xia, C. Zhou, Q. Yong, and X. Wang, "On Selection of Repeated Unit Cell Model and Application of Unified Periodic Boundary Conditions in Micro-mechanical Analysis of Composites," International Journal of Solids and Structures, Vol. 43, pp. 266-278, 2006.

10) C. Sun, and R. Vaidya, "Prediction of Composite Properties from a Representative Volume Element," Composites Science and Technology, Vol. 56, pp. 171-179, 1996.

11) S. Li, "General Unit Cells for Micromechanical Analysis of Unidirectional Composites," Composites, Part A: Applied Science and Manufacturing, Vol. 32, pp. 815-826, 2000.

12) Z. Xia, Y. Chen, and F. Ellyin, "A Meso/Micro-Mechanical Model for Damage Progression in Glass-Fiber/Epoxy Cross-Ply Laminates by Finite Element Analysis," Composites Science and Technology, Vol. 60, pp. 1171-1179, 2000.

13) P. Raghavan, S. Moorthy, S. Ghosh, and N. Pagano, "Revisiting the Composite Laminate Problem with an Adaptive Multi-Level Computational Model," Composites Science and Technology, Vol. 61, pp. 1017-1040, 2001.

14) Z. Xia, Y. Zhang, and F. Ellyin, "A Unified Periodical Boundary Conditions for Representative Volume Element of Composites and Applications," International Journal of Solids and Structures, Vol. 40, pp. 1907-1921, 2003.

15) A. Drago and M. Pindera, "Micro-Macromechanical Analysis of Heterogeneous Materials: Macroscopically Homogeneous vs Periodic Microstructures," Composites Science and Technology, Vol. 67, pp. 1243-1263, 2007.

16) A. Evans, F. Zok, and J. Davis, "The Role of Interfaces in Fiber-Reinforced Brittle Matrix Composites," Composites Science and Technology Vol. 42, pp. 3-24, 1991.

17) N. Miriyala and P. Liaw, "The Monotonic and Fatigue Behavior of CFCCs," Journal of Materials, Vol. 48, pp. 44-52, 1996.

18) L. Mishnaevsky and P. Brondsted, "Micromechanisms of Damage in Unidirectional Fiber Reinforced Composites: 3D Computational Analysis," Composites Science and Technology, Vol. 69, pp. 1036-1044, 2009.

19) H. Wang, Q. Qin, H. Zhou, and H. Miao, "Damage Progress Simulation in Unidirectional Composites by Extended Finite Element Method (XFEM)," Advanced Materials Research, Vol. 152-153, pp. 73-76, 2011.

20) H. Ismar and F. Streicher, "Modeling and Simulation of the Mechanical Behavior of Ceramic Matrix Composites as Shown by the Example of SiC/SiC," Computational Materials Science, Vol. 16, pp. 17-24, 1999.

21) L. Yang, Y. Yan, Z. Ran, and Y. Liu, "A New Method for Generating Random Fiber Distributions for Fiber Reinforced Composites," Composites Science and Technology, Vol. 76, pp. 14-20, 2013.

22) Z. Wang, X. Wang, J. Zhang, W. Liang, and L. Zhou, "Automatic Generation of Random Distribution of Fibers in Long-Fiber-Reinforced Composites and Mesomechanical Simulation," Materials and Design, Vol. 32, pp. 885-891, 2011.

23) S. Liu, L. Zhang, X. Yin, L. Cheng, and Y. Liu, "Microstructure and Mechanical Properties of SiC and Carbon Hybrid Fiber Reinforced SiC Matrix Composite," International Journal of Applied Ceramic Technology, Vol. 8, pp. 308-316, 2011.

24) E. J. Barbero, "Finite Element Analysis of Composite Materials using Abaqus," CRC Press, Taylor & Francis Group, Boca Raton, FL, 2013.

25) ABAQUS/Standard User's Manual, Vol. I and II (ver. 6.12), 2012. Hibbit, Karlsson and Sorensen, Inc., Pawtucket, Rhode Island.

26) C. Chamis, “Simplified Composite Micromechanics Equations for Hygral, Thermal, and Mechanical Properties,” SAMPE Quarterly, Vol. 15, pp. 14-23, 1984.

27) K. K. Chawla, “Ceramic Matrix Composites,” Kluwer Academic Publishers, Second Edition, Norwell, MA, 2003.

Table 1 Material properties used in finite element simulations

Materials	Young's Modulus	Poisson's Ratio	Weibull Strength Parameter	Weibull Shape Parameter	Radius	Interface Shear Strength
SiC fiber	354 GPa	0.21	1217 MPa	6.3	6.5	-
SiC matrix	404 GPa	0.16	278 MPa	4.6	-	-
PyC interface	35 GPa	0.23	-	-	-	2.5 MPa

Table 2 Predicted elastic constants from finite element modeling of statistically equivalent RVE

RVE	E_1 (GPa)	$E_2 = E_3$ (GPa)	$\nu_{12} = \nu_{13}$	ν_{23}	$G_{12} = G_{13}$ (GPa)	G_{23} (GPa)
1	364.03	336.07	0.186	0.196	143.35	140.45
2	360.32	331.33	0.188	0.199	141.34	138.18
3	360.49	332.06	0.188	0.198	141.31	138.55
4	362.73	333.89	0.187	0.197	142.46	139.45
5	358.18	329.78	0.189	0.199	140.48	137.51
6	365.11	336.93	0.185	0.195	143.52	140.94
7	358.82	330.86	0.189	0.198	140.80	138.05
8	364.34	335.16	0.186	0.196	143.24	140.10
9	356.57	328.43	0.190	0.199	139.66	136.89
10	364.29	335.25	0.186	0.196	143.43	140.11
11	359.34	330.87	0.188	0.198	140.89	138.02
12	361.60	332.16	0.187	0.198	141.87	138.62
Mean	361.32	332.73	0.187	0.197	141.86	138.91
Standard deviation	2.796	2.685	0.002	0.001	1.317	1.278

Table 3. Comparison of predicted elastic constants with an analytical model

Elastic Constants	Current Model	Chamis Model [26]
E_1 (GPa)	361.32 $\pm$ 2.796	369.64
$E_2 = E_3$ (GPa)	332.73 $\pm$ 2.685	361.81
$\nu_{12} = \nu_{13}$	0.188 $\pm$ 0.002	0.193
ν_{23}	0.198 $\pm$ 0.001	0.202
$G_{12} = G_{13}$ (GPa)	141.73 $\pm$ 1.317	150.56
G_{23} (GPa)	138.77 $\pm$ 1.278	150.56

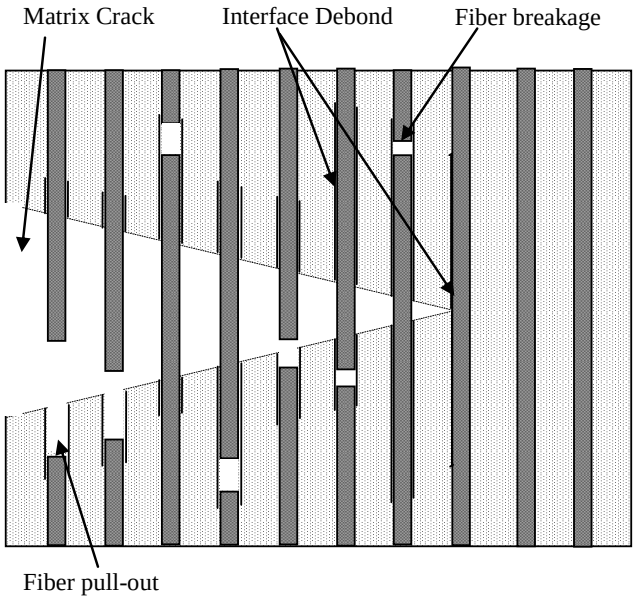

Figure 1 Mechanics of failure in a CFCC

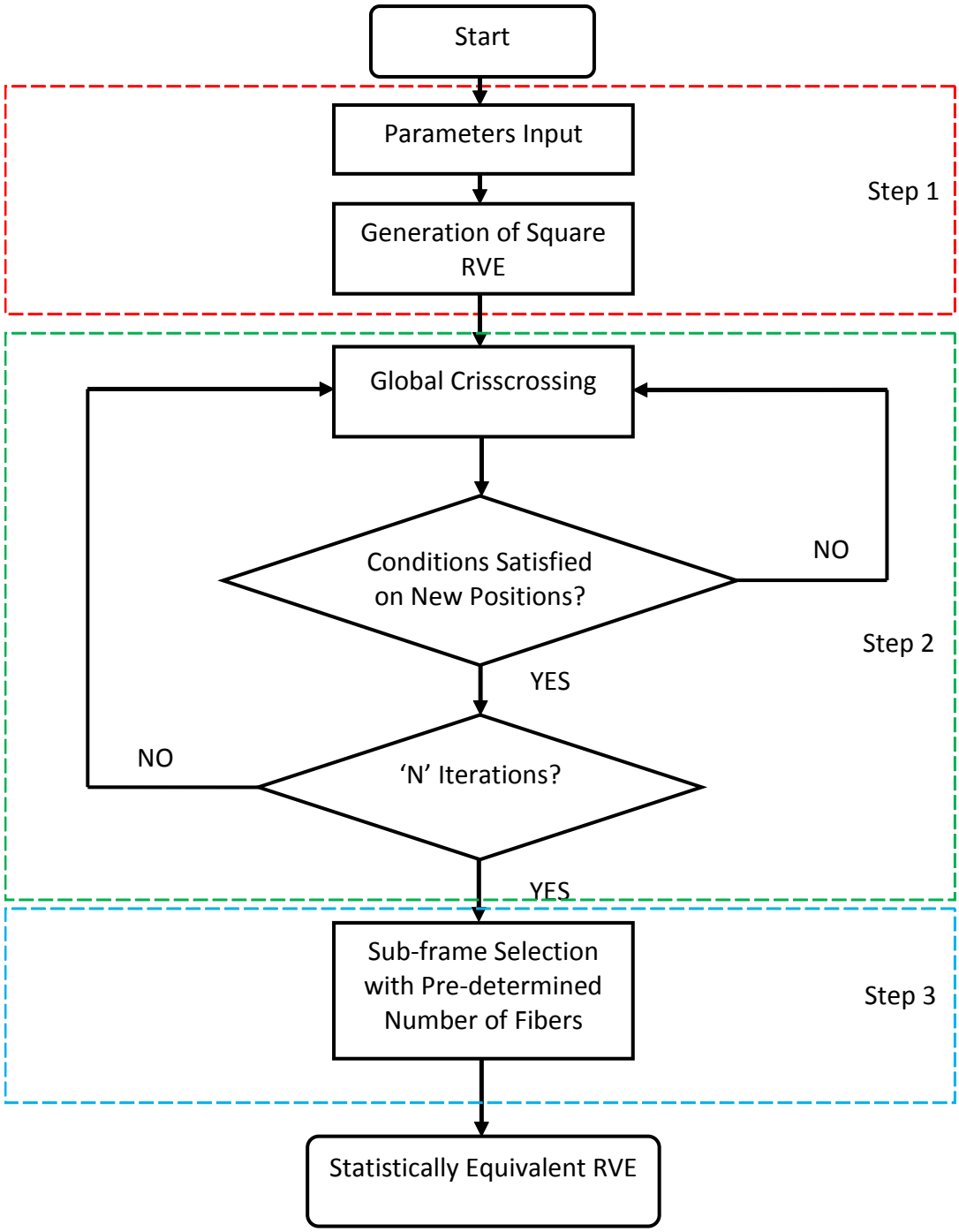

Figure 2 Flow chart for generating a statistically equivalent RVE

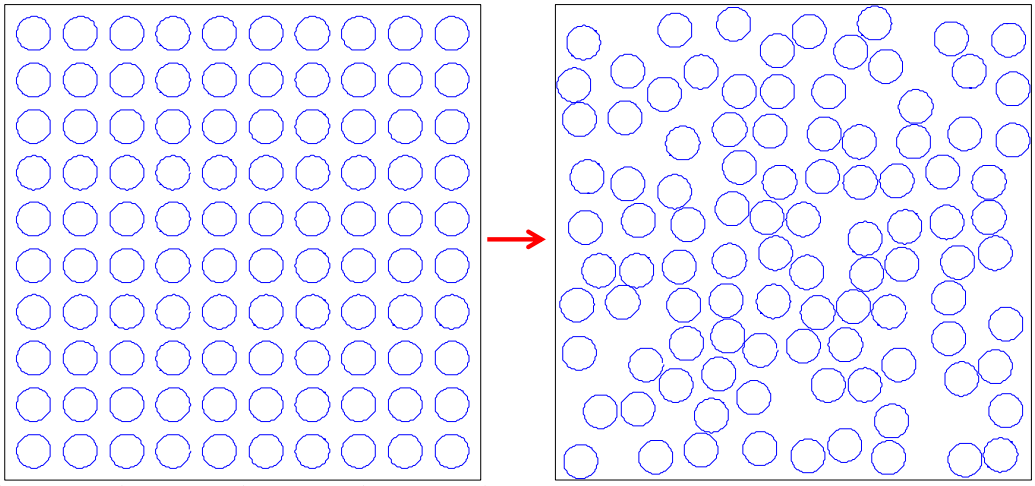

(a) RVE with square packing (b) RVE after global crisscrossing

Figure 3 RVE with randomly distributed fibers after global crisscrossing

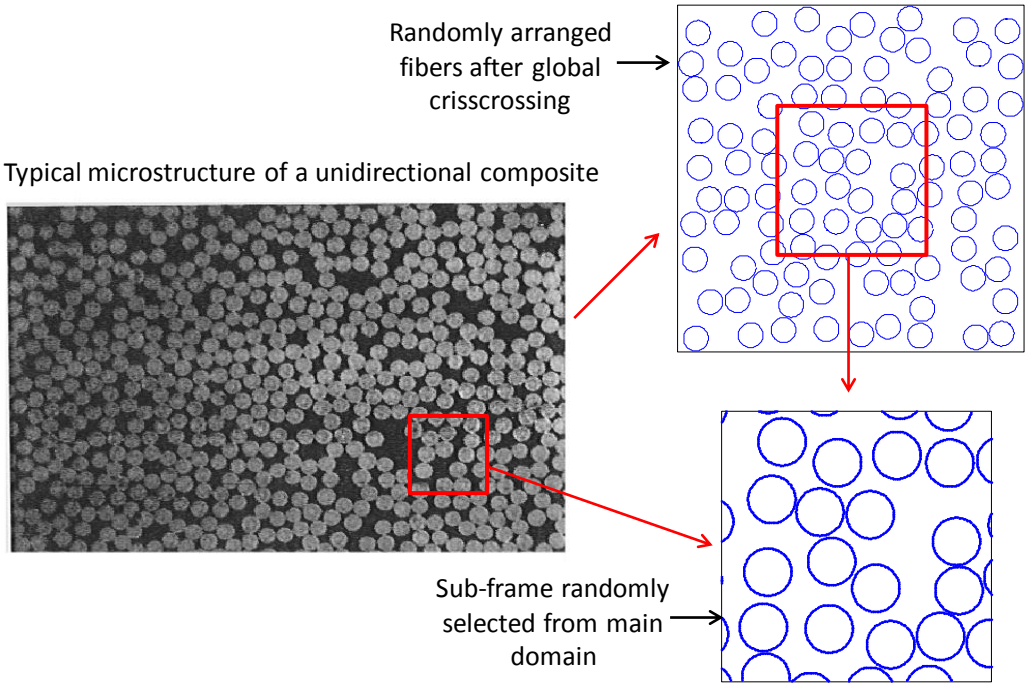

Figure 4 Generation of statistically equivalent RVE

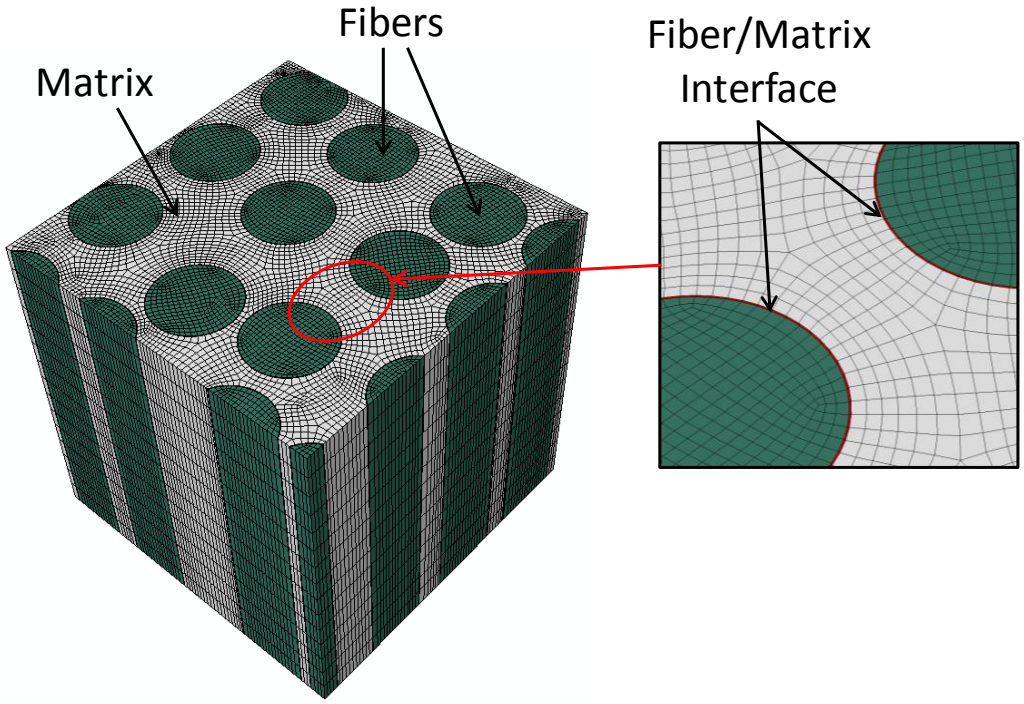

Figure 5 Finite element model of RVE

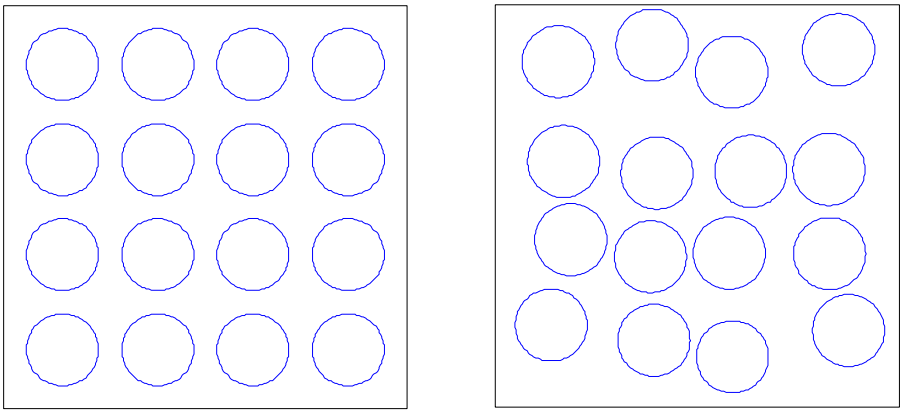

(a) Mesoscale behavior - Orthotropic

(b) Mesoscale behavior – Transversely isotropic

Figure 6 Mesoscale behavior of an RVE with (a) parallel fibers and (b) randomly distributed fibers

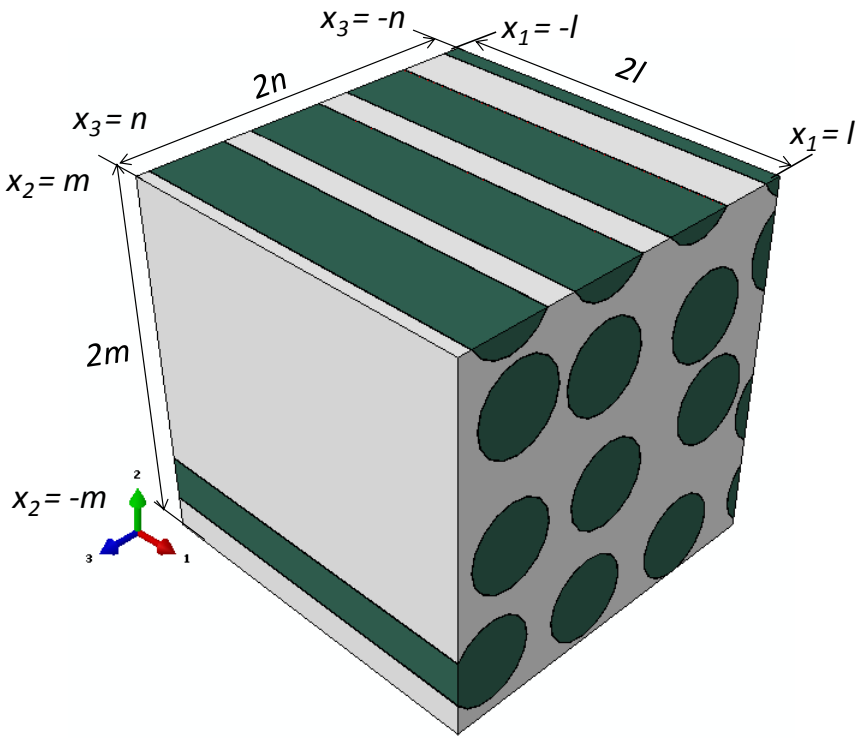

Figure 7 Geometric configuration of statistically equivalent RVE

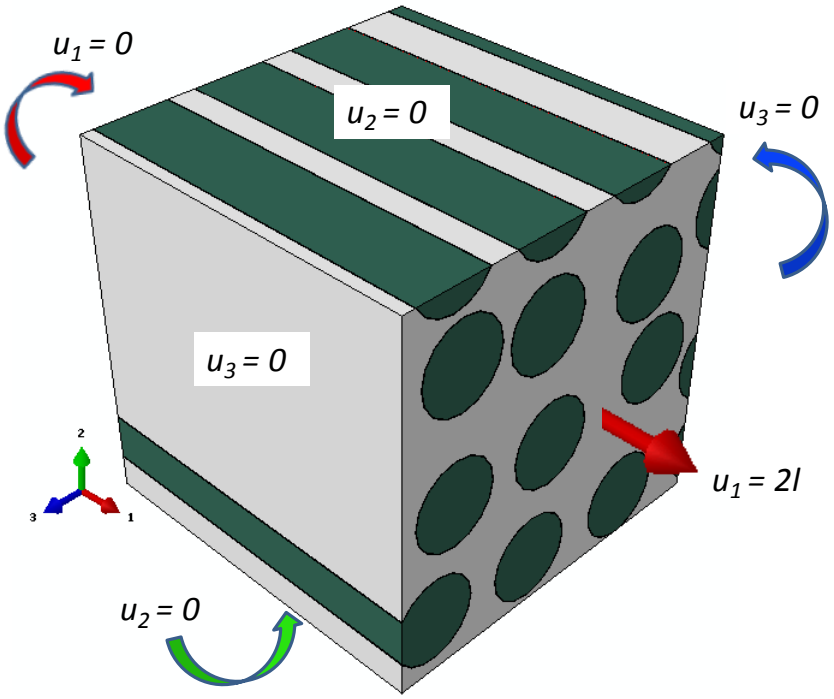

Figure 8 Displacement boundary conditions for computing first column of stiffness tensor

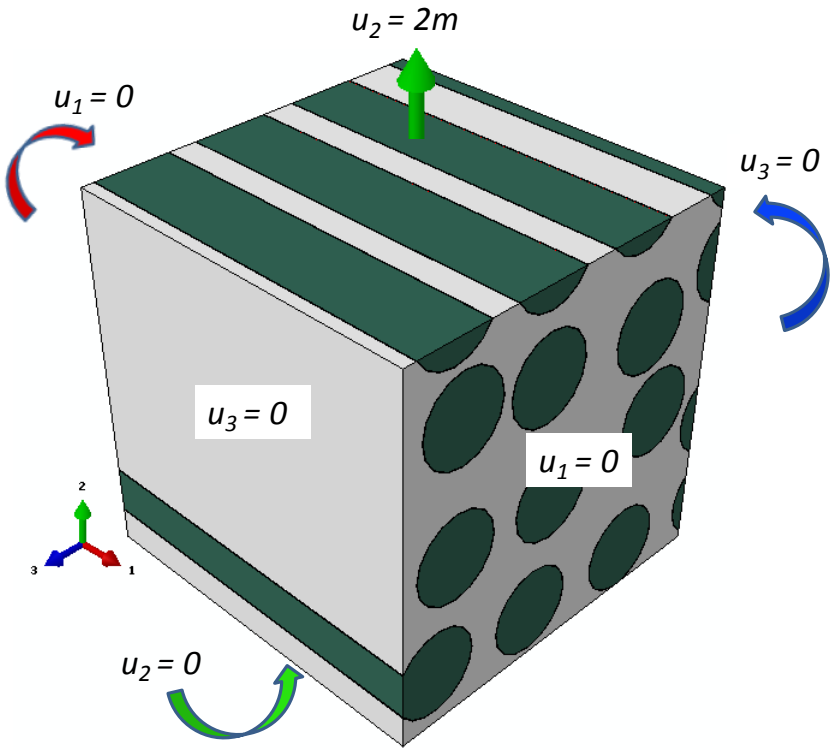

Figure 9 Displacement boundary conditions for computing second column of stiffness tensor

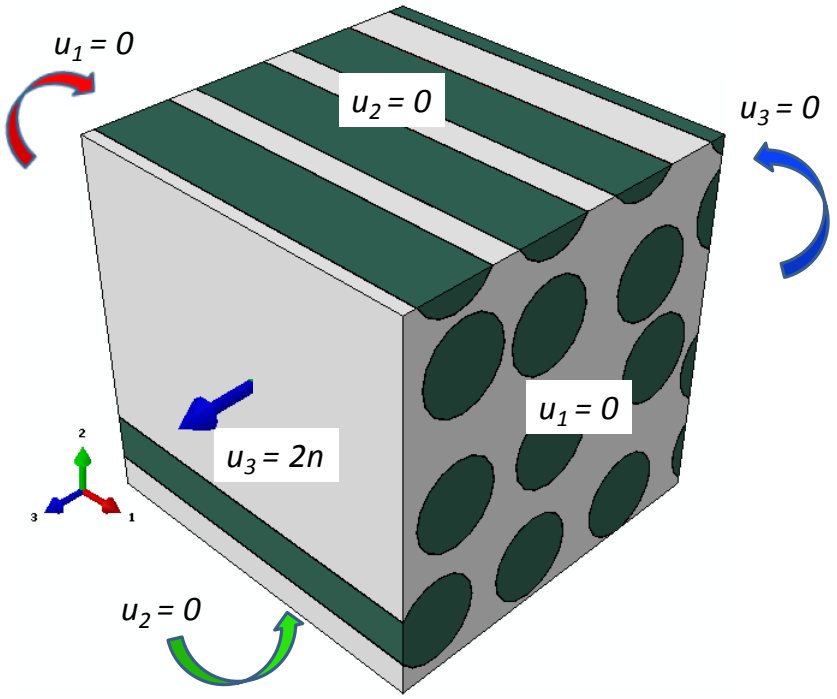

Figure 10 Displacement boundary conditions for computing third column of stiffness tensor

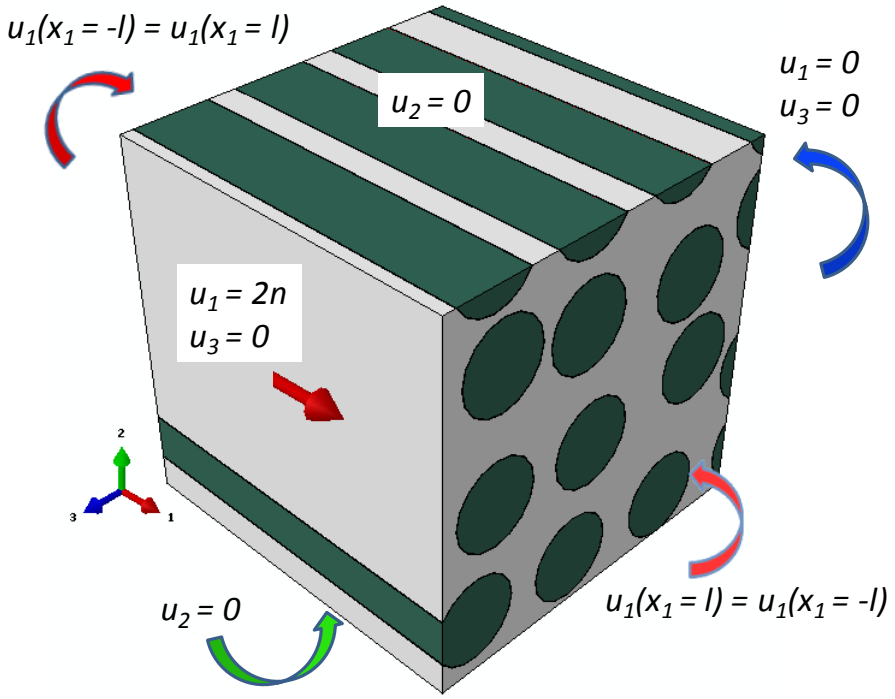

Figure 11 Displacement boundary conditions for computing sixth column of stiffness tensor

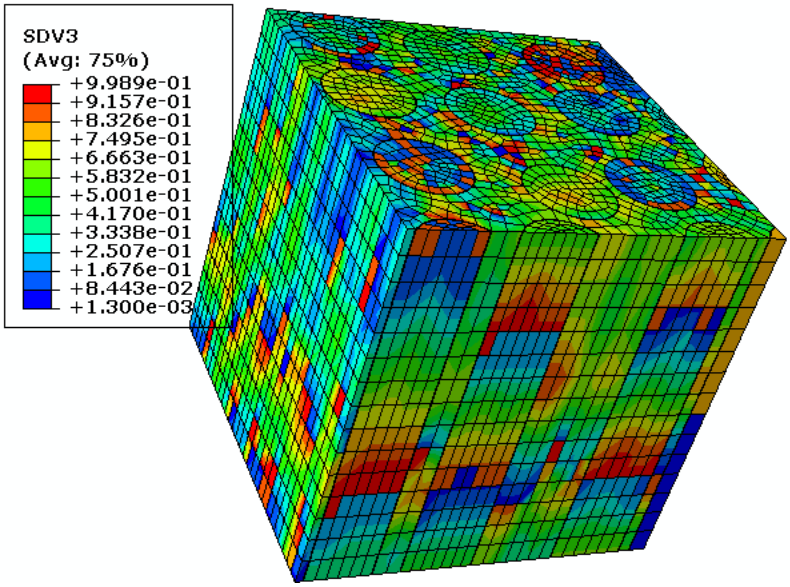

Figure 12 Randomly generated probabilities in fiber and matrix elements

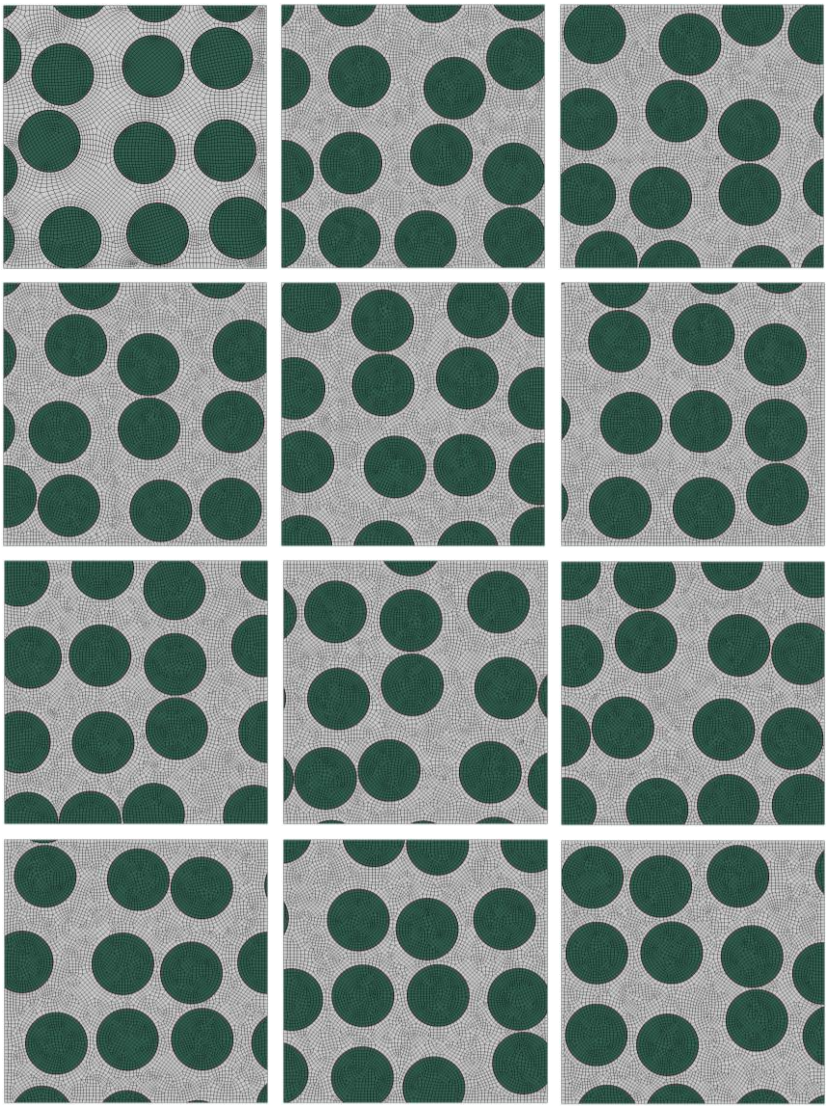

Figure 13 Transverse cross-sections of statistically equivalent RVE finite element models

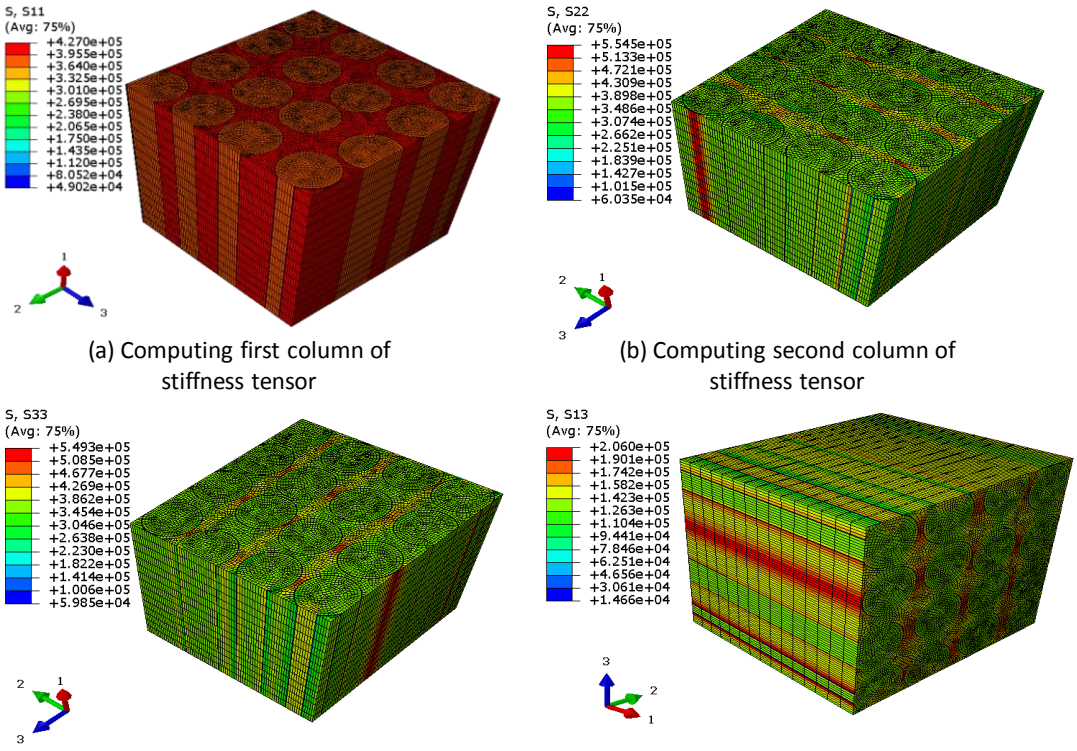

(a) Computing first column of stiffness tensor

(b) Computing second column of stiffness tensor

(c) Computing third column of stiffness tensor

(d) Computing fifth and sixth columns of stiffness tensor

Figure 14 Stress distribution in RVE corresponding to different loading conditions for computing the stiffness tensor

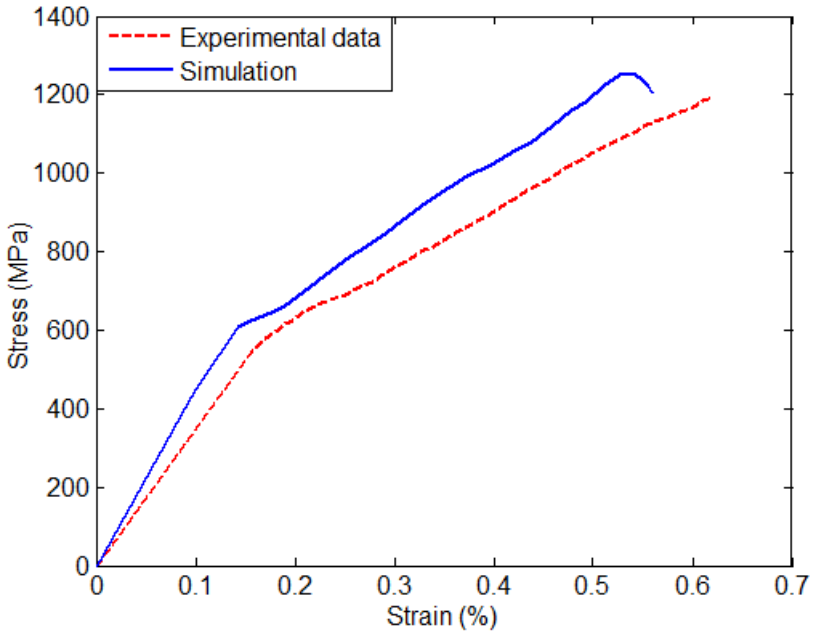

Figure 15 Comparison of longitudinal stress-strain behavior of the composite predicted by the developed finite element model and experimental results from literature [8]

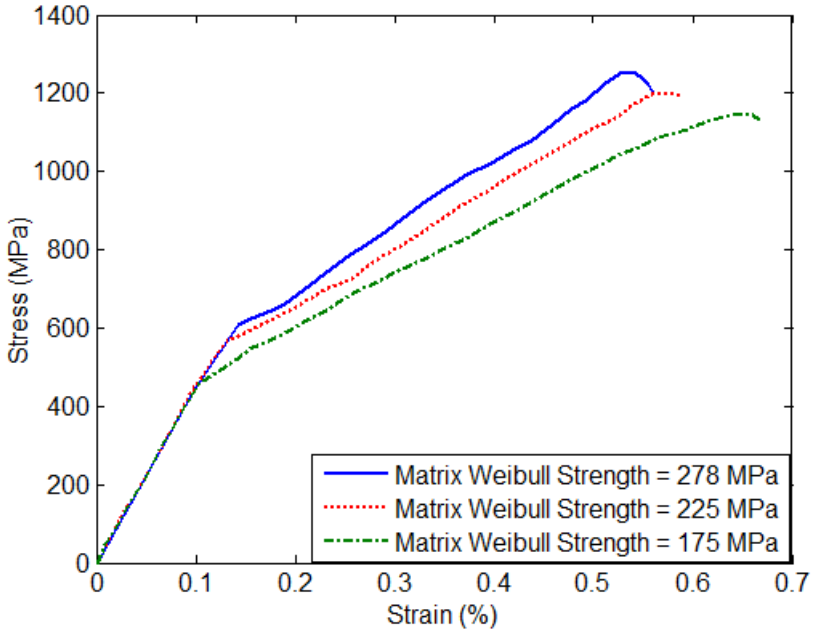

Figure 16 Effect of matrix Weibull strength on stress-strain behavior of the composite

III. MICROSTRUCTURE IMAGE-BASED MULTI-SCALE MODELING OF FRACTURE IN CONTINUOUS FIBER-REINFORCED CERAMIC MATRIX COMPOSITES

V. Bheemreddy[1], K. Chandrashekhara[1,*] L. R. Dharani[1], and G. E. Hilmas[2]

[1]*Department of Mechanical and Aerospace Engineering*

[2]*Department of Materials Science and Engineering*

Missouri University of Science and Technology, Rolla, MO 65409

ABSTRACT

The failure behavior of a continuous fiber-reinforced ceramic matrix composite (CFCC) is studied by the example of a unidirectionally reinforced composite. A multi-scale modeling framework is developed for evaluating damage at the micro-level. An actual fiber/matrix topology, based on a microstructure image, is used at the micro-level. Finite element mesh of the microstructure is generated using a object oriented finite element analysis tool. An extended finite element method, integrated with cohesive damage modeling, is used to study crack propagation in the microstructure. Finite element model validation using a baseline case study is discussed. The effect of cohesive parameters of individual phases on stress-displacement behavior in the micromechanical model is studied. Cohesive parameters, cohesive strength and fracture energy, of the micromechanical model are estimated from constituent properties.

1. INTRODUCTION

The microstructure of a material controls its physical and mechanical properties [1]. Several analytical and numerical techniques have evolved to predict the behavior of

multiphase materials. Analytical models provide reasonable estimate of material behavior but, are applicable for simple phase configurations. Several micromechanical models have been developed over decades to predict the macromechanical behavior of the material. Often these methods are integrated with finite element simulations to extend the realm of problems that can be modeled, but these models rely on simplifying assumptions about the geometry/distribution/orientation of the microstructure. A novel approach alternative to these traditional methods is image-based finite element analysis of microstructures wherein, finite element mesh is generated directly on the microstructure of the material followed by subsequent analysis using the same microstructure mesh domain. A object oriented finite element analysis (OOF) tool has been developed by few researchers at the Center for Theoretical and Computational Material Science, National Institute of Standards and Technology (NIST) to predict the material behavior and multiple other purposes using experimental/simulated microstructures [2-5]. OOF has been used to predict the thermal/mechanical behavior of a material by several investigators. Chawla et al. [1] have implemented OOF to predict elastic and material constants of two examples case studies – silicon carbide particle-reinforced aluminum matrix composites and double-cemented tungsten carbide particle-reinforced cobalt matrix composites. Levis and Geltmacher [6] have developed a three-dimensional spatial reconstruction of an austentic steel microstructure and incorporated the image into OOF to study the mesomechanical response. Goel et al. [7] have used OOF to investigate the longitudinal elastic modulus of glass fiber/polypropylene thermoplastic composite. The authors have compared the numerical results using the developed model with those of experimental results and results from other models. The authors have also concluded the

significance of taking microstructural parameters into account for accurate prediction of modulus. Dong and Bhattacharyya [8] have implemented OOF for predicting the tensile properties of polypropylene/organoclay nanocomposites using the images from scanning electron microscope (SEM) and transmission electron microscope (TEM). The authors have also compared their results with experimental and theoretical composite models. Bakshi et al. [9] have estimated the overall elastic modulus of spark plasma sintered tantalum carbide using a technique called scan-and-solve and compared their results with OOF.

The failure analysis of heterogeneous materials, accounting for damage initiation and evolution, has ben explored by many researchers [10-16]. Advanced numerical methods have been developed to introduce an arbitrary discontinuity in the models for an effective analysis of material failure [16-19]. Cohesive damage models, based on traction-separation laws, were developed for simulating damage initiation and evolution. However, cohesive models require prior knowledge of crack paths. Numerical methods on treating arbitrary cracks without any prior knowledge of crack paths were first developed by Belytschko et al. [15, 18, 19, 20]. Crack tip enrichments were introduced for enhancing the nodal degrees of freedom, for effective description of element discontinuity displacement. This method is called as the extended finite element method (XFEM).

In this study, a multi-scale framework based on XFEM and OOF was developed to study failure behavior in a microstructure. OOF was used to generate a finite element mesh of the microstructure. The paper is organized as follows. Finite element mesh generation of a microstructure is detailed in Section 2. Theoretical background on XFEM

and the multi-scale framework are described in Section 3. Results are discussed in Section 4.

2. DOMAIN DISCRETIZATION OF MICROSTRUCTURES USING OOF

2.1 OOF framework for domain discretization

The domain discretization scheme used in OOF for generating finite element mesh of a CFCC microstructure is shown in Figure 1. This procedure will enable clustering of various material phases or classify grains from their boundaries, and thereby make the discretized image useful for further analysis using numerical simulations. The starting point in the discretization scheme is a gray-scale image. Each pixel of the image has a different gray level and the goal of domain discretization is to group pixels with similar intensities. Pixel selection is conducted by selecting an arbitrary pixel, and pixels with similar gray levels are highlighted for forming groups. In the 'microstructure' step the image is segmented by classifying the individual phases. After creating the microstructure, material properties can be assigned to each pixel or individual phases. The next step is to create a finite element mesh skeleton. In this step, the element type required (quadrilateral/triangular) and their positions can be specified. Using appropriate element refinement methods and node motion, a finite element mesh with good representation of associated geometry can be obtained. A skeleton is, however, not a complete finite element mesh as it contains no information about the finite element interpolation functions. Once a good mesh representation is obtained, an actual finite element mesh can be created from the skeleton. This step adds physics and math to the skeleton and a fully functional finite element mesh is created, which can be transferred to

Abaqus v.6.12 for further study. The algorithms used for image segmentation are beyond the scope of this paper and are discussed elsewhere.

2.2 Finite element mesh generation of a microstructure

OOF was used to generate finite element mesh of a microstructure image consisting of 1452 pixel x 1452 pixel. Figure 2 shows the SEM image of a unidirectional composite microstructure.

The light and dark regions represent different material phases. The darker phase with circular regions corresponds to a ceramic fiber and the lighter phase is a ceramic matrix. These individual phases were clustered into separate pixel groups using the OOF framework as outlined in section 2.1. For the finite element mesh skeleton, the parameters used were - maxscale = 60 pixels, minscale = 20 pixels, and threshold = 0.9 [2]. The microstructure was coarse meshed with quadrilateral elements and mesh size was refined iteratively using various routines – refine, snap nodes, and snap refine, to create a quality mesh conforming to material boundaries. Figure 3 shows the finite element mesh of the microstructure obtained using the above discretization scheme.

Two element functionals, shape energy and homogeneity energy, were used to quantify the quality of mesh generated. The former measures the quality of the shape of elements while the latter measures mesh compliance with boundaries. A mesh is considered to be of good quality if the summation of the weighted average of functionals is low. The shape energy functional (E_{shape}) favors low aspect ratio elements and was calculated for quadrilateral elements using,

$$E_{shape} = 1 - \left(\left(1 - w_{opp}\right) q_{min} + w_{opp} q_{opp} \right) \tag{1}$$

$$q = 2 \frac{A_1}{L_1^2 + L_2^2} \tag{2}$$

Where, q is the quality measured at each corner, q_{min} corresponds to a corner with minimum q , q_{opp} is the q measured at opposite corner, A_1 is the area of parallelogram formed by two edges adjacent to a corner, L_1 and L_2 are lengths of the adjacent sides to a corner, and $w_{opp} = 10^{-5}$ is an arbitrary parameter.

The homogeneity functional (E_{hom}) was calculated using,

$$E_{hom} = 1 - H \tag{3}$$

$$H = \frac{max_i\{a_i\}}{A_2} \tag{4}$$

Here, a_i is the fraction of area of an element that conforms to material i, and A_2 is the area of element. The weighted sum of the two functionals gives effective element energy,

$$E = \alpha E_{hom} + (1 - \alpha)E_{shape} \tag{5}$$

Where, α is an adjustable parameter and 0.5 is the value used in this work [2].

3. XFEM BASED MULTI-SCALE MODELING FRAMEWORK

3.1 XFEM method

The XFEM method is an effective numerical approach for discrete crack modeling problems, and is based on Galerkin and partition of unity concepts [10, 11]. This method involves local enrichment of approximation spaces, which becomes particularly useful for approximating solutions of computational domains with discontinuities and singularities. A discontinuity is defined here as a high gradient in a field quantity, in a local domain. In solids, these discontinuous field quantities are typically stresses/strains or displacements, due to interfaces or cracks. Using local

enrichment, XFEM allows to model discontinuities in element interiors thereby not requiring to a priori define a mesh conforming to crack boundaries. Conventional finite element approaches often result in low convergence rates and exhibit poor accuracy in modeling these problems.

To understand how an enrichment function is added to the finite element approximation, a simple crack domain is considered as shown in Figure 4(a).

The objective is to represent the mesh in Figure 4(a) (Mesh A) using the mesh in Figure 4(b) (Mesh B). The finite element approximation for Mesh A is given by,

$$u^h = \sum_{i=1}^{10} N_i u_i \tag{6}$$

Where, N_i and u_i are shape function and displacement vector, respectively, at node i. Two parameters, a_1 and a_2, are defined using,

$$a_1 = \frac{u_9 + u_{10}}{2}, a_2 = \frac{u_9 - u_{10}}{2} \tag{7}$$

u_9 and u_{10} can be expressed in terms of a_1 and a_2 as,

$$u_9 = a_1 + a_2,\ u_{10} = a_1 - a_2 \tag{8}$$

The terms u_9 and u_{10} in Equation (8) are replaced in Equation (6) to get,

$$u^h = \sum_{i=1}^{8} N_i u_i + a_1(N_9 + N_{10}) + a_2(N_9 + N_{10})H(x) \tag{9}$$

Where, $H(x)$ is a discontinuous jump function defined as,

$$H(x) = \begin{cases} 1, & y > 0 \\ -1, & y < 0 \end{cases} \tag{10}$$

Now, $a_1 = (u_9 + u_{10})/2$ in Mesh A can be replaced by u_{11} in Mesh B. Similarly, $N_9 + N_{10}$ can be replaced by N_{11}. Accordingly, the finite element approximation for Mesh B is given by,

$$u^h = \sum_{i=1}^{8} N_i u_i + N_{11} u_{11} + a_2 N_{11} H(x) \tag{11}$$

The first two terms on the right-hand side of Equation (11) correspond to a standard finite element approximation and the third term is discontinuous enrichment. This equation is equivalent to a standard finite element approximation for Mesh B with an additional discontinuous enrichment term. Similar to the discontinuity enrichment, XFEM approximation uses a crack tip enrichment term. Figure 5 shows the nodal enrichment representation (discontinuity and crack tip) in a crack domain.

Overall, the XFEM based enriched finite element approximation is generalized and is given by,

$$u = \sum_{i \in \Omega} N_i(x) \left[u_i + \underbrace{H(x) a_i}_{i \in \Omega_d} + \underbrace{\sum_{j=1}^{4} F_j(x) b_i^j}_{i \in \Omega_c} \right] \tag{12}$$

Here, N_i is the shape function, u_i is the displacement vector, $H(x)$ is the jump function or disconuity function, $F_j(x)$ is the crack tip enrichment function, a_i and b_i are nodal enriched degree of freedom vectors corresponding to discontinuous enrichment function and crack tip enrichment function respectively. The standard finite element approximation is applicable for all the nodes (Ω) in the model, crack tip enrichment function is applicable for set of all nodes (Ω_c) with shape function supports cut by crack

tip, and discontinuity enrichment function is for set of all nodes (Ω_d) with shape function cut by crack interior (excluding the nodes in Ω_c).

3.2 Multi-scale modeling approach

The multi-scale configuration used in this study for analyzing the micromechanical fracture behavior is shown in Figure 6. The specimen configuration corresponds to a tensile specimen with no pre-crack and plain strain conditions were assumed. This framework integrates the homogeneous material and mechanical loading at global level with the fracture mechanism in a heterogeneous material at local level. The global model includes controlled loading and specimen geometric configuration. The local model constitutes explicit representation of phases in a microstructure. While the global model utilizes elastic properties only, elastic properties and damage parameters (cohesive strength and fracture energy) were used for modeling the microstructure constituents.

The failure behavior in the microstructure was modeled using the XFEM approach. Damage evolution is the critical part of modeling failure in the microstructure region. In this study, a cohesive damage modeling based approach was used. A bilinear traction-separation law (Figure 7) was used for modeling the damage evolution. The traction-separation law is characterized by a peak traction 'T_{max}' corresponding to a critical separation 'δ_{max}', and finally by a maximum separation parameter 'δ_{sep}'. In this work, the peak traction parameter corresponds to maximum nominal stress of the material. When the traction stresses are integrated over the separation, the resultant is the energy dissipated 'ϕ' during failure.

$$\phi = \int_0^{\delta_{sep}} T(\delta)\, d\delta \tag{13}$$

4. RESULTS AND DISCUSSION

4.1 Model validation using a baseline case study

The baseline case is a representative volume element (RVE) of a ceramic matrix composite under transverse tensile loading [10]. The authors in this work have developed an approach to estimate the ply level strength and toughness as a function of its microstructural attributes (fiber, matrix, and interface). The authors have implemented an augmented finite element technique for simulating arbitrary cracking in the ceramic matrix, and proposed augmented cohesive zone elements for modeling the fiber/matrix interface. The RVE developed by the authors had circular fibers of 10 μm diameter and fiber volume fraction was 50%. In the current study, the finite element mesh shown in Figure 3 is used as the RVE instead of randomized fiber geometry assumed by the authors. This microstructure has a fiber volume fraction of 44.71%. Table 1 shows the material properties of constituent phases, as used in the baseline study.

The model was developed in a commercial finite element code – Abaqus v.6.12 [21]. Typically, fiber failure under a transverse tensile load is not observed due to weak interfaces. Accordingly, the crack propagation was modeled only in matrix and interface and the XFEM enrichment was active in these phases only. Under transverse tensile loading, multiple crack initiation and propagation were observed. A discussion on the crack propagation is provided in the next sub-section for a composite microstructure. The stress-displacement behavior was modeled for this baseline case and compared with the results provided by Fang et al. The stress vs. displacement behavior of the RVE was estimated from elastic and fracture parameters of constituent phases, as shown in Figure 8. The predicted results had a higher initial stiffness as observed from the slope of the curve.

The peak stress and displacement were predicted to be lower as compared to the baseline result. The area under the stress vs. displacement curves was calculated and a variation of 12.66% in the estimated fracture energies was observed. This difference was assumed to be due to multiple factors – range of fiber diameters in the microstructure, fiber packing, and fiber volume fraction.

4.2 Failure analysis of a composite microstructure

The validated model was extended to a unidirectionally reinforced composite microstructure. Figure 9 shows the multi-scale model developed for studying the failure behavior in a composite microstructure. The global model and the local model were discretized using a 4-node bilinear quadrilateral element (CPE4). The global model had a total of 19200 elements, while the local model had 90,000 elements. A transverse tensile load was applied on the global model. The local model was modeled as a sub-model i.e. loads applied on the global model are transferred to the local model through the 'driven nodes' (on the local model). This methodology also ensures that boundary conditions for a RVE are automatically satisfied through the multi-scale modeling approach. Using the XFEM method, crack initiation and propagation are studied in the local model. Table 2 shows the material properties of the constituent phases, required for the numerical simulation. Similar to the baseline study, the failure of matrix and interface is governed by a traction-separation law. The XFEM enrichment was applied for matrix and interface elements only.

Due to the applied transverse tensile load, multiple crack initiation was observed in the matrix. Figure 10 shows the formation of matrix cracks in the local model. It was observed that the matrix cracks have initiated in the locations with high fiber packing density. Similar observation of crack initiation was made by Fang et al. [10]. The

discontinuities in these locations indicates crack initiation phase i.e. damage initiation criterion was satisfied in the traction-separation law (Figure 7). The evolution of these cohesive cracks into a complete crack depends on building up of local stresses. With an increase in applied stress, more cracks were initiated and propagated, leading to establishment of a complete crack.

The influence of cohesive parameters of the fiber/matrix interface and matrix on the predicted stress-displacement behavior (traction-separation) of a RVE was evaluated. The effect of interface strength was evaluated at three strength levels – 10 MPa, 30 MPa, and 50 MPa (Figure 11). It was observed that the strength of the RVE increases with increase in interfacial strength. The strength of the RVE almost doubled by increasing the interface strength from 10 MPa to 50 MPa. This increase was due to increase in load transfer between the fiber and matrix at higher interface strength. The area under the curves was calculated for evaluating the fracture energy. The fracture energy of the RVE increased by 14.58% by increasing the interface strength from 10 MPa to 50 MPa. In the work conducted by Fang et al. [10], a maximum increase in RVE cohesive parameters was observed by increasing the interface strength.

Figure 12 shows the influence of interface toughness on the observed stress-displacement behavior. The interface toughness was evaluated at two levels – 2 J/m^2 and 5 J/m^2. These values were selected based on the range of interface toughness values provided in the technical literature [22]. Due to the increase in interface toughness, there was no significant change of RVE parameters, as compared to the interface strength. The fracture energy of the RVE increased by 4.16% by increasing the interface toughness. Similar to the interface, the cohesive parameters of matrix were evaluated. The matrix

strength had no significant impact on the RVE parameters. However, increasing the fracture energy resulted in a increase in critical displacement on stress-displacement curve.

6. CONCLUSIONS

In this study, a multi-scale modeling framework was developed for studying the failure behavior of a CFCC. Finite element mesh was generated for an actual microstructure image of a unidirectionally reinforced composite. XFEM method was integrated in to the multi-scale framework to simulate crack propagation in the microstructure. The developed model was validated by comparing with a baseline case study from technical literature. The effect of cohesive damage modeling parameters of matrix and interface on the predicted stress-displacement behavior of the RVE was evaluated. The interface strength had the maximum effect on the cohesive parameters of the RVE. There was a 14.58% increase in RVE's fracture energy and the cohesive strength doubled by increasing the interface strength from 10 MPa to 50 MPa. Increasing the interface fracture energy had increased the RVE's fracture energy by 4.16%. The cohesive parameters of matrix had minimal impact on the RVE's parameters. The multi-scale framework developed in this study can be extended to a ply-level damage model.

REFERENCES

1. N. Chawla, B. V. Patel, M. Koopman, K. K. Chawla, R. Saha, B. R. Patterson, E. R. Fuller, and S. A. Langer, "Microstructure-Based Simulation of Thermomechanical Behavior of Composite Materials by Object-Oriented Finite Element Analysis," Materials Characterization, Vol. 49, pp. 395-407, 2002.

2. S. Langer, E. R. Fuller, and W. C. Carter, "OOF: An Image-Based Finite-Element Analysis of Material Microstructures," Computing in Science and Engineering, Vol. 3, pp. 15-23, 2001.

3. A. C. E. Reid, S. A. Langer, R. C. Lua, V. R. Coffman, S. –I. Haan, and R. E. Garcia, "Image-Based Finite Element Mesh Construction for Material Microstructures," Computational Material Science, Vol. 43, pp. 989-999, 2008.

4. A. C. E. Reid, R. C. Lua, R. E. Garcia, V. R. Coffman, and S. A. Langer, "Modeling Microstructures with OOF2," International Journal of Materials and Product Technology, Vol. 35, pp. 361-373, 2009.

5. V. R. Coffman, A. C. E. Reid, S. A. Langer, and G. Dogan, "OOF3D: An Image-Based Finite Element Solver for Materials Science," Mathematics and Computers in Simulation, Vol. 82, pp. 2951-2961, 2012.

6. A. C. Lewis and A. B. Geltmacher, "Image-Based Modeling of the Response of Experimental 3D Microstructures to Mechanical Loading," Scripta Materialia, Vol. 55, pp. 81-85, 2006.

7. A. Goel, K. K. Chawla, U. K. Vaidya, N. Chawla, and M. Koopman, "Two-Dimensional Microstructure Based Modeling of Young's Modulus of Long Fibre Thermoplastic Composite," Materials Science and Technology, Vol. 24, pp. 864-869, 2008.

8. Y. Dong and D. Bhattachaaryya, "Morphological-Image Analysis Based Numerical Modeling of Organoclay Filled Nanocomposites," Mechanics of Advanced Materials and Structures, Vol. 17, pp. 534-541, 2010.

9. S. R. Bakshi, A. Bhargava, S. Mohammadizadeh, A. Agarwal, and I. Tsukanov, "Computational Estimation of Elastic Properties of Spark Plasma Sintered TaC by Meshfree and Finite Element Methods," Computational Material Science, Vol. 50, pp. 2615-2620, 2011.

10. X. Fang, Q. Yang, B. Cox, and Z. zhou, "An Augmented Cohesive Zone Element for Arbitrary Crack Coalescence and Bifurcation in Heterogeneous Materials," International Journal of Numerical Methods in Engineering, Vol. 88, pp. 841-861, 2011.

11. T. Hettich, A. Hund, and E. Ramm, “Modeling of Failure in Composites by X-FEM and Level Sets within a Multiscale Framework,” Computer Methods in Applied Mechanics and Engineering, Vol. 197, pp. 414-424, 2008.

12. B. Cox and Q. Yang, “In Quest of Virtual Tests for Structural Composites,” Science, Vol. 314, pp. 1102-1107, 2006.

13. Y. Li and M. Zhou, “Prediction of Fracture Toughness of Ceramic Composites as Function of Microstructure: I. Numerical Simulations,” Journal of the Mechanics and Physics of Solids, Vol. 61, pp. 472-488, 2013.

14. C. Gonzalez and J. Llorca, “Multiscale Modeling of Fracture in Fiber-reinforced Composites,” Acta Materialia, Vol. 54, pp. 4171-4181, 2006.

15. D. Huynh and T. Belytschko, “The Extended Finite Element Method for Fracture in Composite Materials,” International Journal for Numerical Methods in Engineering, Vol. 77, pp. 214-239, 2009.

16. R. de Borst, “Numerical Aspects of Cohesive Zone Models,” Engineering Fracture Mechanics, Vol. 70, pp. 1743-1757, 2003.

17. J. Melenk and I. Bubaska, “The Partition of Unity Finite Element Method: Basic Theory and Applications,” Computational methods in Applied Mechanics and Engineering, Vol. 139, pp. 289-314, 1996.

18. N. Moës, J. Dolbow, and T. Belytschko, “A Finite Element Method for Crack Growth Without Remeshing,” International Journal for Numerical Methods in Engineering, Vol. 46, pp. 132-150, 1999.

19. S. Loehnert and T. Belytschko, “A Multiscale Projection Method for Macro/Microcrack Simulations,” International Journal for Numerical Methods in Engineering, Vol. 71, pp. 1466-1482.

20. T. Belytschko and T. Black, “Elastic Crack Growth in Finite Elements with Minimal Remeshing,” International Journal for Numerical Methods in Engineering, Vol. 45, pp. 601-620, 1999.

21. ABAQUS/Standard User’s Manual, Vol. I and II (ver. 6.12), 2012. Hibbit, Karlsson and Sorensen, Inc., Pawtucket, Rhode Island.

22. S. Liu, L. Zhang, X. Yin, L. Cheng, and Y. Liu, “Microstructure and Mechanical Properties of SiC and Carbon Hybrid Fiber Reinforced SiC Matrix Composite,” International Journal of Applied Ceramic Technology, Vol. 8, pp. 308-316, 2011.

Table 1 Material properties of constituent phases of a ceramic matrix composite [10]

Material	Modulus $E\ (GPa)$	Poisson's ratio ν	Cohesive strength $T_{max}\ (MPa)$	Fracture energy $\phi\ (J/m^2)$
Ceramic matrix	200	0.35	150	20
Ceramic fiber	40	0.3		
Fiber/matrix interface			10	10

Table 2 Material properties of constituent phases in a SiC/SiC_f ceramic composite [22]

Material	Modulus $E\ (GPa)$	Poisson's ratio ν	Cohesive strength $T_{max}\ (MPa)$	Fracture energy $\phi\ (J/m^2)$
SiC matrix	350	0.21	300	2
SiC fiber	270	0.2	2800	20
Interface			10	2

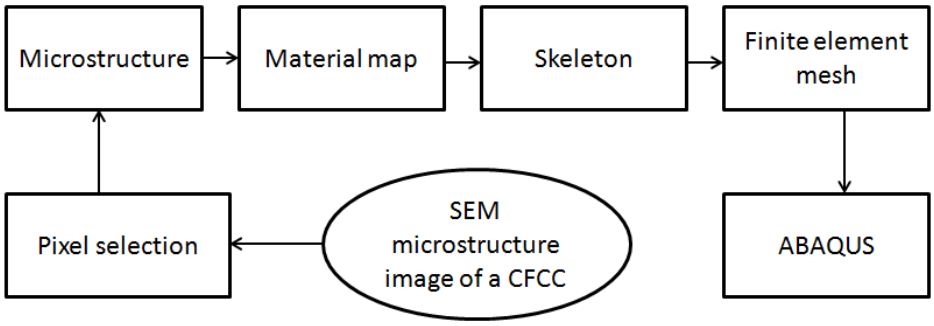

Figure 1 Domain discretization scheme using OOF

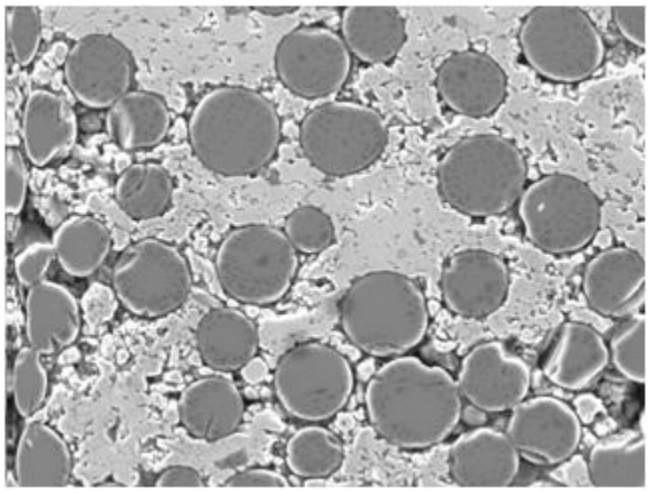

Figure 2 SEM microstructure image of a CFCC

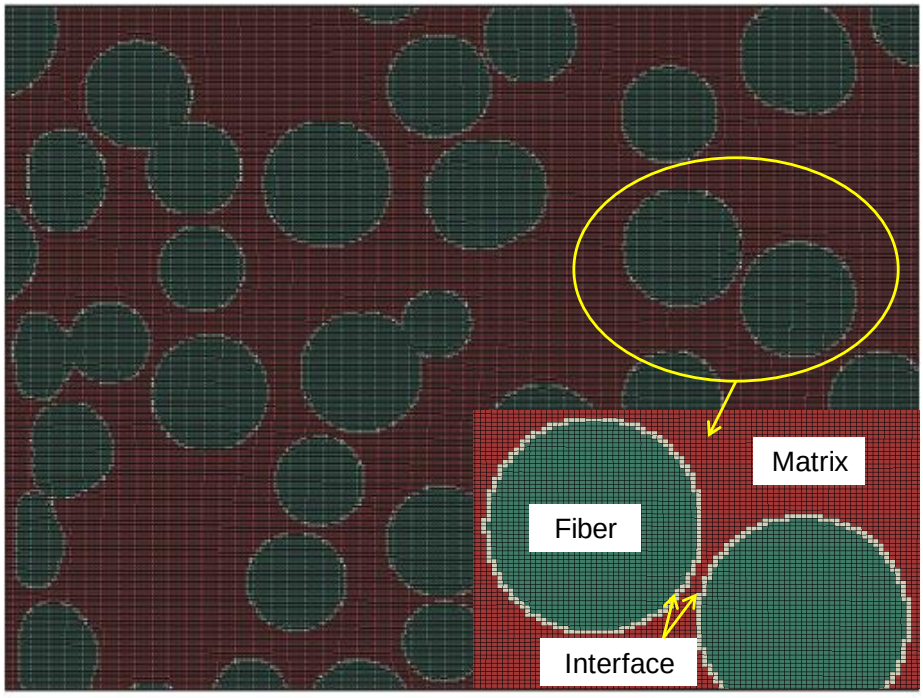

Figure 3 Finite element mesh of the microstructure

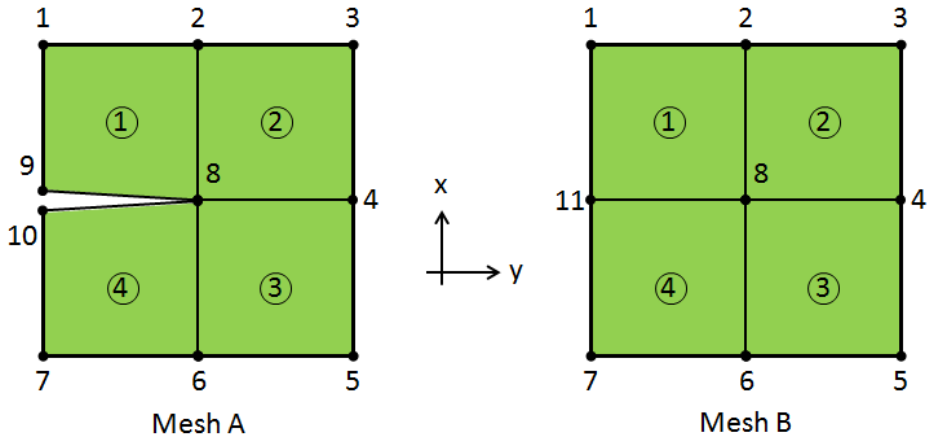

(a) (b)

Figure 4 Finite element mesh: (a) with a crack, (b) without a crack (enrichment)

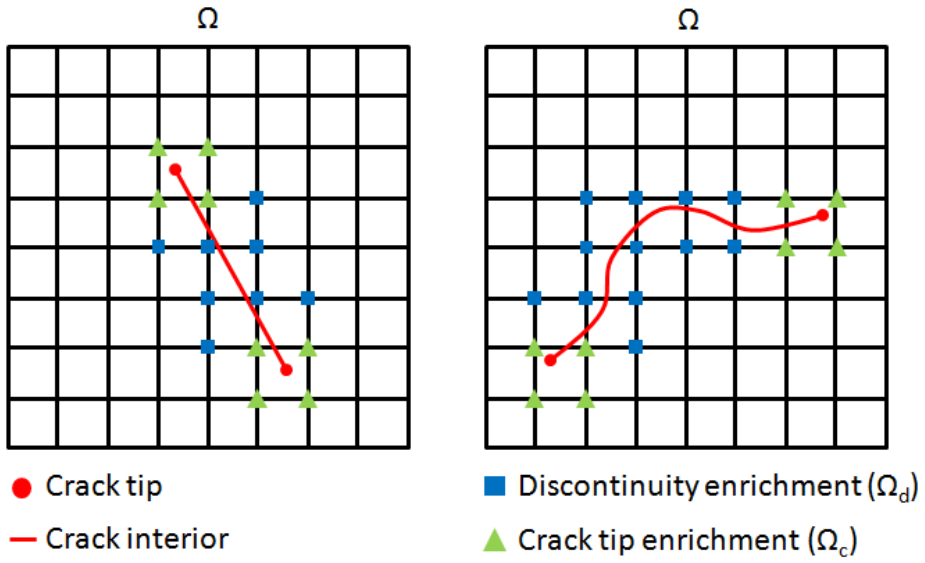

Figure 5 Nodal enrichment around crack tip and crack interiors

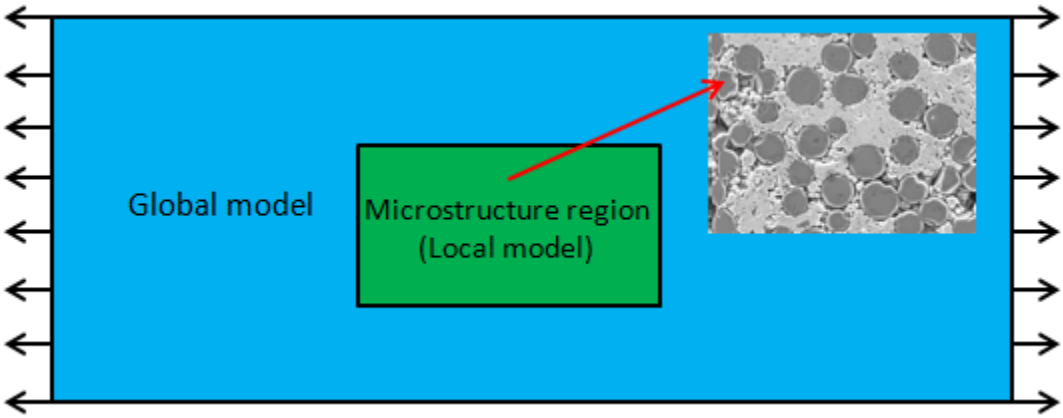

Figure 6 Multi-scale framework used in the analysis

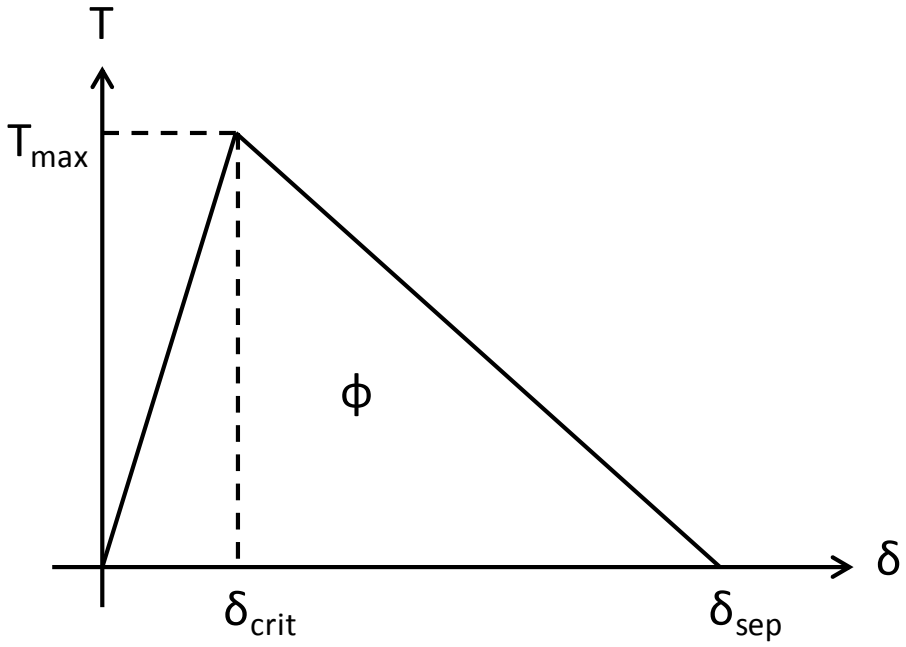

Figure 7 Traction-separation law for modeling damage evolution

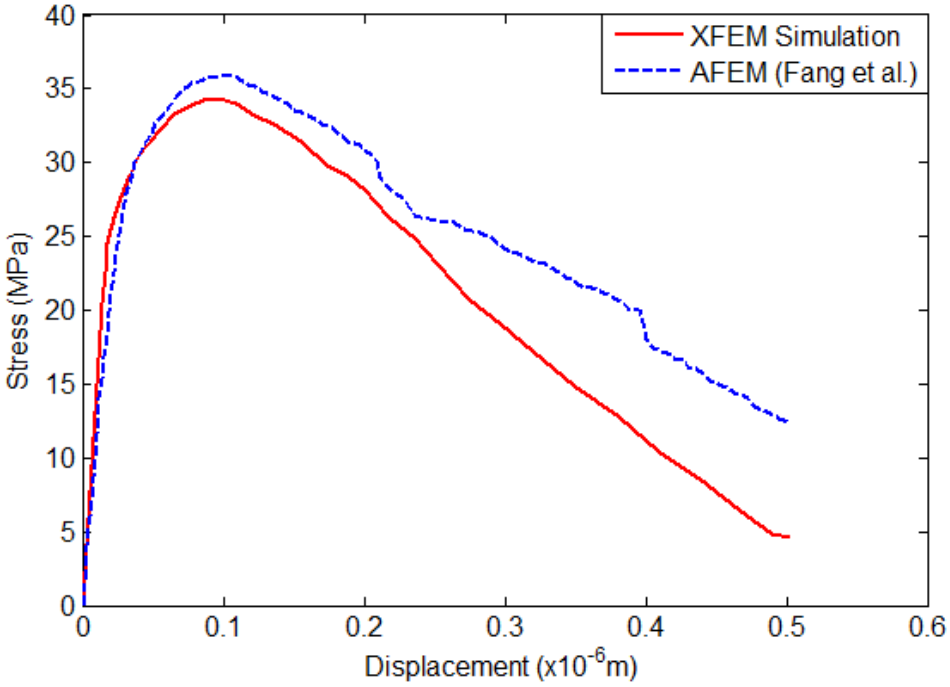

Figure 8 Comparison of predicted stress vs. displacement behavior with baseline results

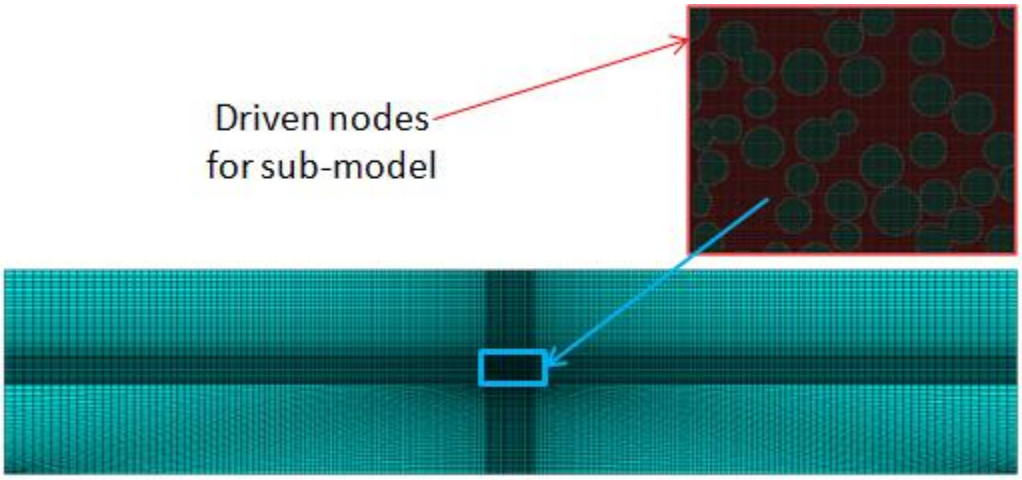

Figure 9 Multi-scale model for failure study in a CFCC

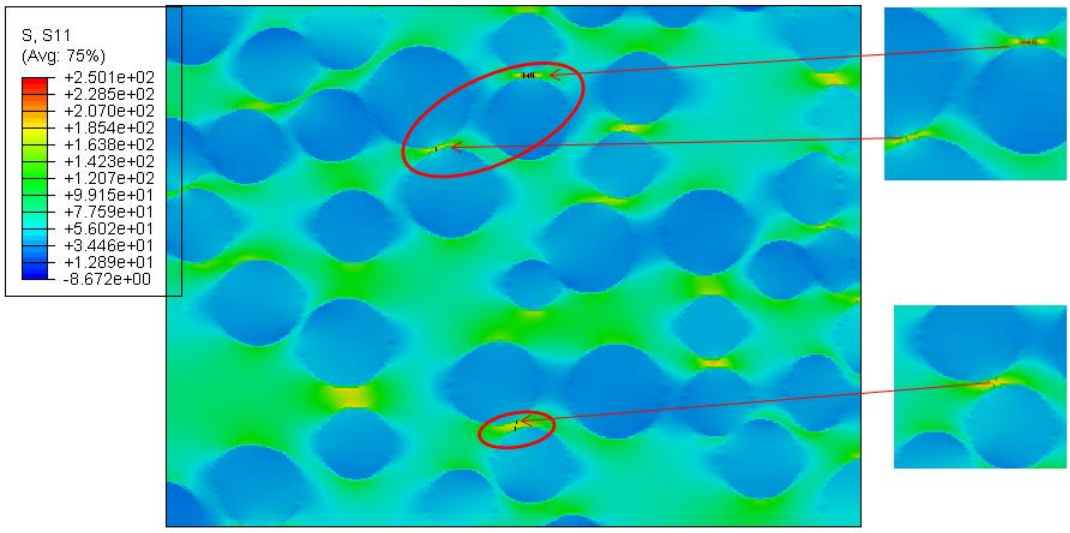

Figure 10 Matrix crack initiation

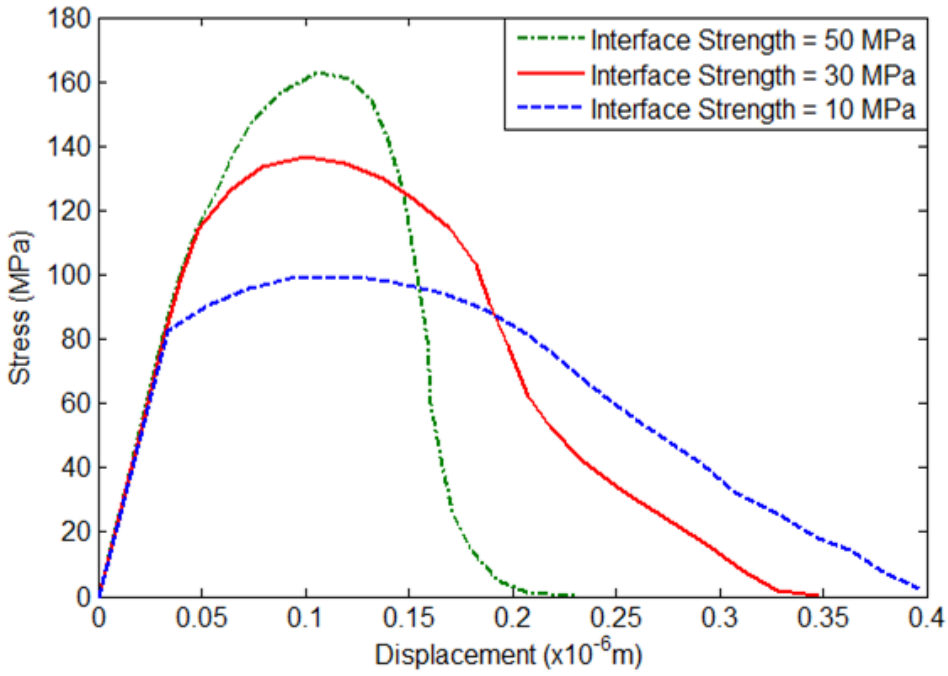

Figure 11 Effect of interface strength on traction-separation behavior in a RVE

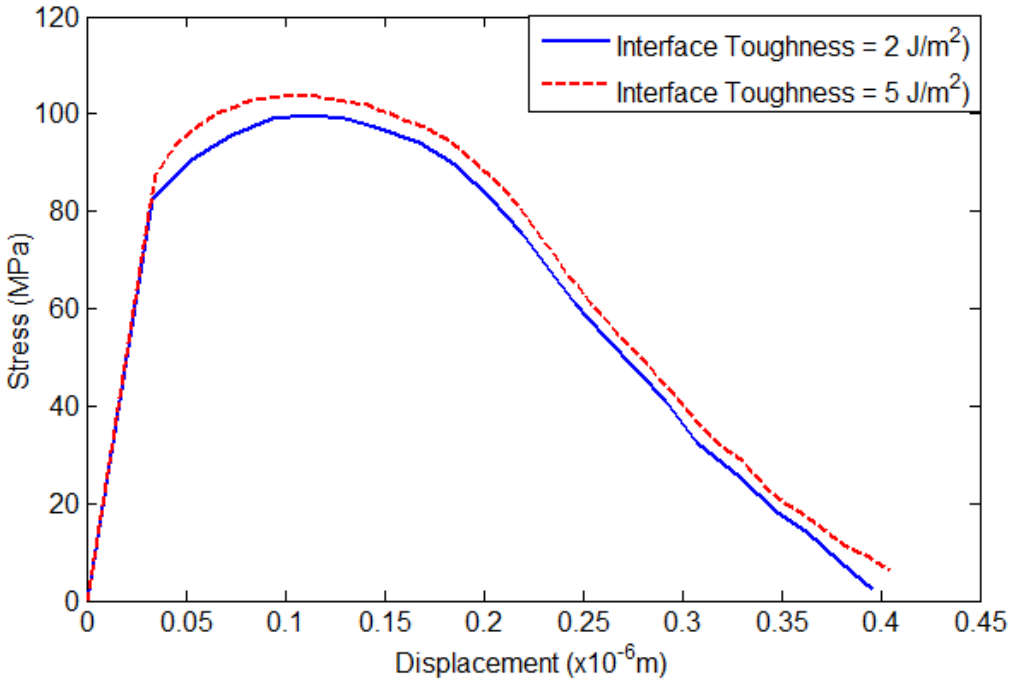

Figure 12 Effect of interface toughness on traction-separation behavior in a RVE

SECTION

4. CONCLUSIONS

The work performed in this dissertation provides a valuable procedure for developing a multi-scale framework for comprehensive damage study of CFCCs.

The first paper provides numerical models to study the load-displacement behavior during fiber pull-out in continuous fiber reinforced ceramic composites. Two numerical models are developed – an axi-symmetric finite element model based on a cohesive damage modeling approach integrated with frictional contact, and an artificial neural networks (ANN) model. Both the models were validated using an analytical model. The ANN model was trained and tested using the analytical model and finite element model. The ANN model has shown good potential in near-accurately predicting the load-displacement behavior. With the availability of a larger data set of experimental results, the ANN model can be trained rigorously to capture the intricate details from experimental observations which otherwise are difficult to analyze using analytical models. For the material system considered in this study, the debond initiation load was observed to be high enough to completely debond the interface without an increase in load.

The second paper provides a detailed study of mechanical behavior in a CFCC using the representative volume element (RVE) approach and damage models. In this study, a new algorithm was developed to generate the statistically equivalent RVE models. Fiber/matrix interface was explicitly defined in these models. Elastic properties of the unidirectional composite were estimated using the developed RVE models and validated using an analytical model. A damage model was developed and integrated with the RVE model using a user-material subroutine. Weibull probability of failure was used to account for scattered strength distribution in brittle fiber and matrix materials. The stress vs. strain behavior of composite under a uniaxial tensile load was predicted using the damage model. The finite element results were validated using the stress vs. strain experimental data from literature. The brittle (low failure strain) to tough (high failure strain) transition of the composite was studied. The models developed in this study can be

extended to generate multiscale damage models which can integrate geometries and loading at macro level to failure analysis at microstructural level.

In the third paper, a multi-scale modeling framework was developed for studying the failure behavior of a CFCC. Finite element mesh was generated for an actual microstructure image of a CFCC. XFEM method was integrated in to the multi-scale framework to simulate crack propagation in the microstructure. The effect of cohesive damage modeling parameters of matrix and interface on the predicted stress-displacement behavior of the RVE was evaluated. The multi-scale framework developed in this study can be extended to a ply-level damage model.

BIBLIOGRAPHY

1) V. Birman and L. Byrd, "Review of Fracture and Fatigue in Ceramic Matrix Composites," Applied Mechanical Reviews, Vol. 53, pp. 147-174, 2000.

2) N. Lissart and J. Lamon, "Damage and Failure in Ceramic Matrix Minicomposites: Experimental Study and Model," Acta Materialia, Vol. 45, pp. 1025-1044, 1997.

3) W. Curtin, B. Ahn, and N. Takeda, "Modeling Brittle and Tough Stress-Strain Behavior in Unidirectional Ceramic Matrix Composites," Acta Materialia, Vol. 46, pp. 3409-3420, 1998.

4) W. Curtin, "Multiple Matrix Cracking in Brittle Matrix Composites," Acta Metallurgica et Materialia, Vol. 41, pp. 1369-1377, 1993.

5) C. Sun, and R. Vaidya, "Prediction of Composite Properties from a Representative Volume Element," Composites Science and Technology, Vol. 56, pp. 171-179, 1996.

6) Z. Xia, C. Zhou, Q. Yong, and X. Wang, "On Selection of Repeated Unit Cell Model and Application of Unified Periodic Boundary Conditions in Micro-mechanical Analysis of Composites," International Journal of Solids and Structures, Vol. 43, pp. 266-278, 2006.

7) S. Li, "General Unit Cells for Micromechanical Analysis of Unidirectional Composites," Composites, Part A: Applied Science and Manufacturing, Vol. 32, pp. 815-826, 2000.

8) Z. Xia, Y. Chen, and F. Ellyin, "A Meso/Micro-Mechanical Model for Damage Progression in Glass-Fiber/Epoxy Cross-Ply Laminates by Finite Element Analysis," Composites Science and Technology, Vol. 60, pp. 1171-1179, 2000.

9) L. Mishnaevsky and P. Brondsted, "Micromechanisms of Damage in Unidirectional Fiber Reinforced Composites: 3D Computational Analysis," Composites Science and Technology, Vol. 69, pp. 1036-1044, 2009.

10) C. -H. Hsueh, "Interfacial Debonding and Fiber Pull-Out Stresses of Fiber-Reinforced Composites," Materials Science and Engineering, Vol. A123, pp. 1-11, 1990.

11) S. Zhandarov and E. Mader, "Characterization of Fiber/Matrix Interface Strength: Applicability of Different Tests, Approaches and Parameters," Composites Science and Technology, Vol. 65, pp. 149-160, 2005.

12) C. DiFrancia, T.C. Ward, and R. O. Claus, "The Single-Fibre Pull-Out Test. 1: Review and Interpretation," Composites Part A: Applied Science and Manufacturing, Vol. 27, pp. 597-612, 1996.

13) V. M. C. F. Cunha, J. A. O. Barros, and J. M. Sena-Cruz, "Pullout Behavior of Steel Fibers in Self-Compacting Concrete," Journal of Materials in Civil Engineering, Vol. 22, pp. 1-9, 2010.

14) A. J. G. Jurewicz, R. J. Kerans, and J. Wright, "The Interfacial Strengths of Coated and Uncoated SiC Monofilaments Embedded in Borosilicate Glass," Ceramic Engineering and Science Proceedings, Vol. 10, pp. 925-937, 1989.

15) E. P. Butler, E. R. Fuller, and H. M. Chan, "Interface Properties for Ceramic Composites from a Single Fiber Pull-Out Test," Materials Research Society Symposium Proceedings, Vol. 170, pp. 17-24, 1990.

16) H. Stang and S. P. Shah, "Failure of Fiber-Reinforced Composites by Pull-Out Fracture," Journal of Material Science, Vol. 21, pp. 953-957, 1986.

17) Y. C. Gao, Y. -W. Mai, and B. Cotterell, "Fracture of Fiber Reinforced Materials," Journal of Applied Mathematics and Physics, Vol. 39, pp. 550-572, 1988.

18) J. W. Hutchinson and H. M. Jensen, "Models of Fiber Debonding and Pullout in Brittle Composites with Friction," Mechanics of Materials, Vol. 9, pp. 139-163, 1990.

19) R. J. Kerans and T. A. Parthasarathy, "Theoretical Analysis of the Fiber Pullout and Pushout Tests," Journal of American Ceramic Society, Vol. 74, pp. 1585-1596, 1991.

20) W. Beckert and B. Lauke, "Critical Discussion of the Single-Fibre Pull-Out Test: Does it Measure Adhesion?" Composites Science and Technology, Vol. 57, pp. 1689-1706, 1997.

21) H. -Y. Liu, X. Zhang, Y. -W. Mai, and X. -X. Diao, "On Steady-state Fiber Pull-Out Computer Simulation," Composites Science and Technology, Vol. 59, pp. 2191-2199, 1999.

22) W. Sun and F. Lin, "Computer Modeling and FEA Simulation for Single Fiber Pull-Out," Journal of Thermoplastic Composite Materials, Vol. 14, pp. 327-343, 2001.

23) G. Wei, G. Liu, C. Xu, and X. Sun, "Finite Element Simulation of Perfect Bonding for Single Fiber Pull-Out Test," Advanced Materials Research, Vol. 418-420, pp. 509-512, 2012.

24) X. Fang, Q. Yang, B. Cox, and Z. zhou, "An Augmented Cohesive Zone Element for Arbitrary Crack Coalescence and Bifurcation in Heterogeneous Materials," International Journal of Numerical Methods in Engineering, Vol. 88, pp. 841-861, 2011.

25) T. Hettich, A. Hund, and E. Ramm, "Modeling of Failure in Composites by X-FEM and Level Sets within a Multiscale Framework," Computer Methods in Applied Mechanics and Engineering, Vol. 197, pp. 414-424, 2008.

26) B. Cox and Q. Yang, “In Quest of Virtual Tests for Structural Composites,” Science, Vol. 314, pp. 1102-1107, 2006.

27) Y. Li and M. Zhou, “Prediction of Fracture Toughness of Ceramic Composites as Function of Microstructure: I. Numerical Simulations,” Journal of the Mechanics and Physics of Solids, Vol. 61, pp. 472-488, 2013.

28) C. Gonzalez and J. Llorca, “Multiscale Modeling of Fracture in Fiber-reinforced Composites,” Acta Materialia, Vol. 54, pp. 4171-4181, 2006.

29) D. Huynh and T. Belytschko, “The Extended Finite Element Method for Fracture in Composite Materials,” International Journal for Numerical Methods in Engineering, Vol. 77, pp. 214-239, 2009.

30) R. de Borst, “Numerical Aspects of Cohesive Zone Models,” Engineering Fracture Mechanics, Vol. 70, pp. 1743-1757, 2003.

31) J. Melenk and I. Bubaska, “The Partition of Unity Finite Element Method: Basic Theory and Applications,” Computational methods in Applied Mechanics and Engineering, Vol. 139, pp. 289-314, 1996.

32) N. Moës, J. Dolbow, and T. Belytschko, “A Finite Element Method for Crack Growth Without Remeshing,” International Journal for Numerical Methods in Engineering, Vol. 46, pp. 132-150, 1999.

33) S. Loehnert and T. Belytschko, “A Multiscale Projection Method for Macro/Microcrack Simulations,” International Journal for Numerical Methods in Engineering, Vol. 71, pp. 1466-1482.

34) T. Belytschko and T. Black, “Elastic Crack Growth in Finite Elements with Minimal Remeshing,” International Journal for Numerical Methods in Engineering, Vol. 45, pp. 601-620, 1999.

VITA

Mr. Venkata Bheemreddy was born in Warangal, Andhra Pradesh, India. He was admitted to Kakatiya University of Science and Technology, India in 2003 and received his Bachelors degree in Mechanical Engineering in 2007. He worked at Infotech Enterprises Limited, India, as a Design Engineer from June 2007 to July 2008. He continued his graduate study at Missouri University of Science and Technology (formerly University of Missouri-Rolla), Rolla, Missouri, USA, and received his M.S. degree in Mechanical Engineering in 2010.

Since August 2010, Mr. Venkata Bheemreddy has been enrolled in the Ph.D. Program in Mechanical Engineering at Missouri University of Science and Technology. He has served both as Graduate Research Assistant and Graduate Teaching Assistant between August 2010 and August 2014 in the Department of Mechanical and Aerospace Engineering. In December 2014, he received his Ph.D. degree in Mechanical Engineering from Missouri University of Science and Technology, Rolla, Missouri.